Design and Control of Virtual Synchronous Machine Based Energy Systems

by

Baruwa Muftau Olatunji

A thesis submitted to

SWANSEA UNIVERSITY

in fulfilment of the requirements for the Degree of

DOCTOR OF PHILOSOPHY

College of Engineering

SWANSEA UNIVERSITY 2021

Prifysgol Abertawe
Swansea University

DECLARATION

Declaration

This work has not previously been accepted in substance for any degree and is not being concurrently submitted in candidature for any degree.

Signed . . . . [redacted] . . . . . .

Date . . . . . 17/05/2021. . . . . .

Statement 1

This thesis is the result of my own investigations, except where otherwise stated. Other sources are acknowledged by footnotes giving explicit references. A bibliography is appended.

Signed . . . . [redacted]. . . . . .

Date . . . . . 17/05/2021. . . . . .

Statement 2

I hereby give consent for my thesis, if accepted, to be available for photocopying and for inter-library loan, and for the title and summary to be made available to outside organisations.

Signed . . . . [redacted] . . . . . .

Date . . . . . 17/05/2021. . . . . .

ABSTRACT

Conventionally, the operation and stability of power systems have been governed by the dynamics of large synchronous generators (SGs) which provide the inertial support required to maintain the resilience and stability of the power system. However, the commitment of the UK to drive a zero-carbon economy is accelerating the integration of renewable energy sources (RESs) into the power system. Since the dynamics and operation of RESs differs from SGs, the large-scale integration of RESs will significantly impact the control and stability of the power system.

This thesis focuses on the design of grid-friendly control algorithms termed virtual synchronous machines (VSMs), which mimic the desirable characteristics of SGs. Although several VSM topologies have been proposed in literature, most of them require further modifications before they can be integrated into the grid. Hence, a novel VSM algorithm for permanent magnet synchronous generator based wind turbines has been proposed in this thesis.

The proposed VSM performs seamlessly in all operating modes and enables maximum power point tracking in grid-connected operation (assuming strong grid), load following power generation in islanded mode and fault ride-through during faults. To ensure optimal performance of the VSM in all operating modes, a comprehensive stability analysis of the VSM was performed in the event of small and large perturbations. The result of the analysis was used to establish design guidelines and operational limits of the VSM.

This thesis further evaluates the impact of VSMs on the power systems low-frequency oscillations (LFOs). A detailed two-machine test-bed was developed to analyze the

LFOs which exists when VSMs replace SGs. The characteristics of the LFO modes and the dominant states was comprehensively analyzed. The LFO modes which exists in an all-VSM grid was also analyzed. Further, the role of the power system stabilizers in an all-VSM grid was comprehensively evaluated. An IEEE benchmark two-area four-machine system was employed to validate the results of the small-signal analysis.

The analysis and time-domain simulations in this thesis were performed in the MATLAB/SIMULINK environment.

DEDICATION

In the name of Allah, the most beneficent the most merciful. All praise and adoration is due to Almighty God alone, who has made this journey possible, we glorify Him and beseech His help in all our affairs.

First and foremost, my sincere appreciation goes to my lovely parents and siblings, thanks for the du'as, unparalleled care, admonitions and motivation; my appreciation goes beyond words can express, may Allah reward you all abundantly.

My sincere and profound appreciation goes to my wife's parents, Alhaji & Alhaja Amoo, for their tremendous support, love, words of motivation and encouragement.

I express my profound appreciation to my supervisor, Dr. M. Fazeli for his immense support, motivation, constructive criticism, honest feedback and guidance from the commencement, development, through to the completion of my Ph.D thesis. My deep appreciation also goes to Dr. Augustine Egwebe, thanks for the momentous impetus and immense support.

My sincere appreciation goes to Dr. Mahboob, Dr. John Macaulay, Dr. Steve Orimoloye, Dr. Eric Wen, Engr. Blessing (PhD in view) for their immense and unflinching support.

My heartfelt appreciation goes to the love of my life, my sweet heart and my wife, Sakeenah Amoo, thanks for your care, understanding, patience and sincerity; thanks for everything, thanks for being there for me, I hope to be with you forever.

Big thanks to my lovely kids, Sumayyah, Maryam and Ibraheem for their love and cheerful disturbances (smiles).

LIST OF PUBLICATIONS

List of Publications

1. M. O. Baruwa, M. Fazeli, and A. M. Egwebe, "New control paradigm for both islanded and grid-connected operation of PMSG-based wind turbine," The Journal of Engineering, IET, vol. 2019, no. 18, pp. 5142-5146, July 2019.

2. B. Muftau, M. Fazeli, and A. Egwebe, "Stability analysis of a PMSG based Virtual Synchronous Machine," Electric Power Systems Research, vol. 180, p. 106 170, Mar. 2020.

3. M. O. Baruwa and M. Fazeli, "Impact of Virtual Synchronous Machines on Low-Frequency Oscillations in Power Systems," in IEEE Transactions on Power Systems, doi: 10.1109/TPWRS.2020.3029111.

4. M. Fazeli, P. M. Holland and M. Baruwa, ""Grid"-Less Power Systems: A Vision for Future Structure of Power Networks," in IEEE Access, vol. 8, pp. 159120-159131, 2020, doi: 10.1109/ACCESS.2020.3020455.

List of Potential Publication

1. M. O. Baruwa and M. Fazeli, "The Role of Virtual Synchronous Machines in Future Power Systems: A Review and Future Trends," (Submitted to the International Journal of Electrical Power and Energy Systems)

CONTENTS

LIST OF FIGURES

LIST OF TABLES

ACRONYMS

AVR	Automatic Voltage Regulator
DERs	Distributed Energy Resources
EMF	Electromotive Force
ESO	Electricity System Operator
ESSs	Energy Storage Systems
FACTS	Flexible alternating current transmission systems
FRT	Fault Ride Through
LFO	Low Frequency Oscillation
LFPG	Load Following Power Generation
MPPT	Maximum Power Point Tracking
NETS SQSS	The National Electricity Transmission System Security and Quality of Supply Standard
PCC	Point of Common Coupling
PEC	Power Electronic Converter
PI	Proportional Integral
PLL	Phase-Locked Loop
PMSG	Permanent Magnet Synchronous Generator
POD	Power Oscillation Damper
PV	Photovoltaic

PWM	Pulse Width Modulation
RESs	Renewable Energy Sources
SG	Synchronous Generator
SSSC	Static Synchronous Series compensator
STATCOM	Static Synchronous compensator
UPFC	Unified Power Flow Controller

1. INTRODUCTION

1.1 Background

Energy is the key driver for the socio-economic growth and development of any nation [1], [2]. Since the industrial revolution in the 19^{th} century, the world energy demand has increased exponentially [2], [3]. This has led to the tremendous expansion in the electrical power system, which is now one of the largest industries, ubiquitous in most regions of the world [3]–[5]. Currently, the power system is dominated by large fossil-fueled synchronous generators (SGs), which provide power to load centres via interconnected transmission lines [3], [6]. The SGs operate in synchronism and inherently provide damping and inertial response to mitigate the impact of disturbances on the network; thus, maintaining the stability and reliability of the power system [7], [8]. However, the adverse enviro-economical impact of the conventional fossil-fueled SGs, is driving the revolution for an alternative energy source which is clean and sustainable [9]–[11].

The power system is transitioning from the centralized fossil-fuel based system to a decarbonized and decentralized smart system with energy prosumers (producers + consumers) [12]–[15]. It is estimated that the decarbonisation of the energy sector by 2050 will add $52 trillion to the global GDP, and a 62% reduction in air pollution related ailments [16], [17]. The British National Grid is committed to decarbonize the energy sector by replacing the conventional fossil-fueled SGs with renewable energy sources (RESs) [17], [18]. Fig. 1.1 illustrates the projected power generation trend for the Great Britain (GB) [18].

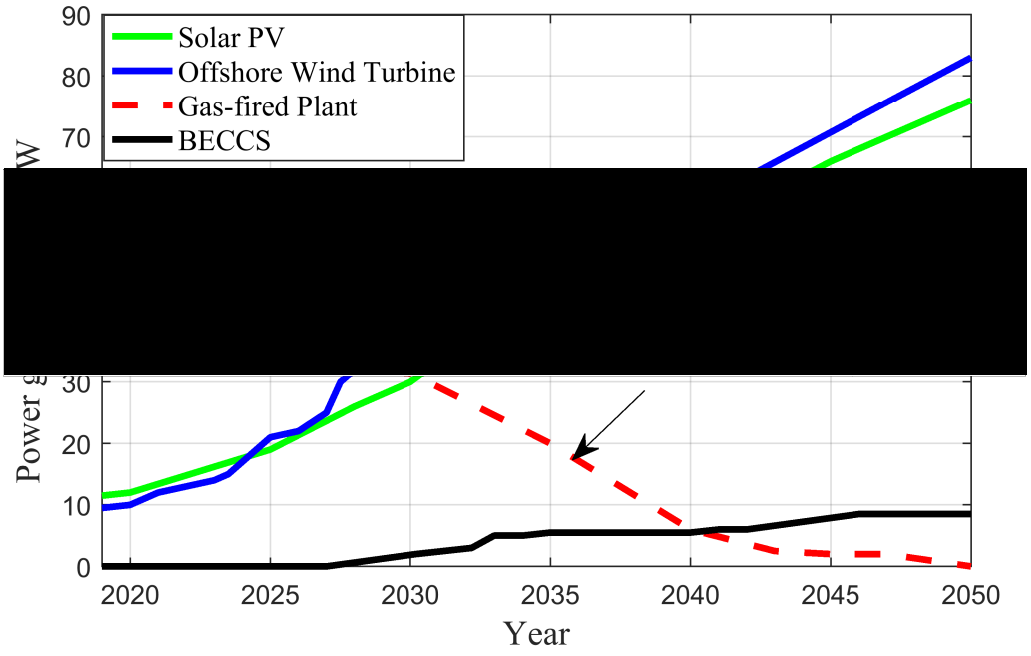

Fig. 1.1. Trend of GB power generation "Customer Transformation Scenario" [18].

In Fig. 1.1, the combination of bio-energy with carbon capture and storage is termed as BECCS [18]. From Fig. 1.1, it is evident that the proportion of RESs in the generation mix will increase exponentially, while fossil-fueled SGs will be completely retired by 2050.

RESs are often clustered with local loads, energy storage systems (ESSs) and other distributed energy resources (DERs) to form a microgrid [19], [20]. The microgrid functions as a single controllable entity, which can be grid-connected via a point of common coupling (PCC), and can operate in isolation from the grid (islanded mode) [21], [22]. Currently, most RESs operate in grid-following mode, where the grid imposes the voltage and frequency, and the RESs injects a pre-defined amount of power into the network [23], [24]. In islanded mode of operation, the microgrid must regulate the voltage and frequency within stipulated limits by maintaining power balance [25], [26]. A plethora of droop topologies have been proposed in literature to enable reliable operation of microgrids in islanded mode [27]. However, the conventional droop topologies are unable to provide support for the grid during

contingencies (e.g. blackout, fault), and are prone to transient instability [28], [29]. Moreover, reports from various electricity system operators (ESOs) have demonstrated that the increasing penetration of RESs poses significant operational and control challenges, and impacts the power system stability [8], [30], [31].

.

1.2 Power system stability

Power system stability deals with the ability of the power system to regain a state of operating equilibrium after being subjected to disturbances from its initial operating condition [3], [32]. Regulatory and financial constraints have forced ESOs to operate power systems close to their stability limits [3]. Also, the increasing penetration of RESs adds more strain on the power system network, and significantly impacts the power system dynamics and stability [33], [34]. Holistically, power system instability is a single problem; however, instabilities in the power system are impacted by diverse and wide-ranging factors [32]. Hence, the power system stability has been systematically categorized to facilitate the analysis, operation and control of the power system. The power system stability can be classified into (a) rotor angle stability (b) frequency stability (c) voltage stability, and this is illustrated in Fig. 1.2 [35].

1.2.1 Rotor angle stability

The rotor angle (or angular) stability deals with the ability of interconnected SGs to generate adequate restoring forces after being subjected to disturbances, in order to maintain synchronism [3], [32]. It involves the study of the low-frequency oscillations (LFOs) inherent in power systems. The rotor angle stability is subdivided into small-disturbance angle stability and transient stability [35].

Small-disturbance (or small-signal) angle stability deals with the ability of SGs in a system to remain in synchronism after being subjected to small disturbances (e.g.

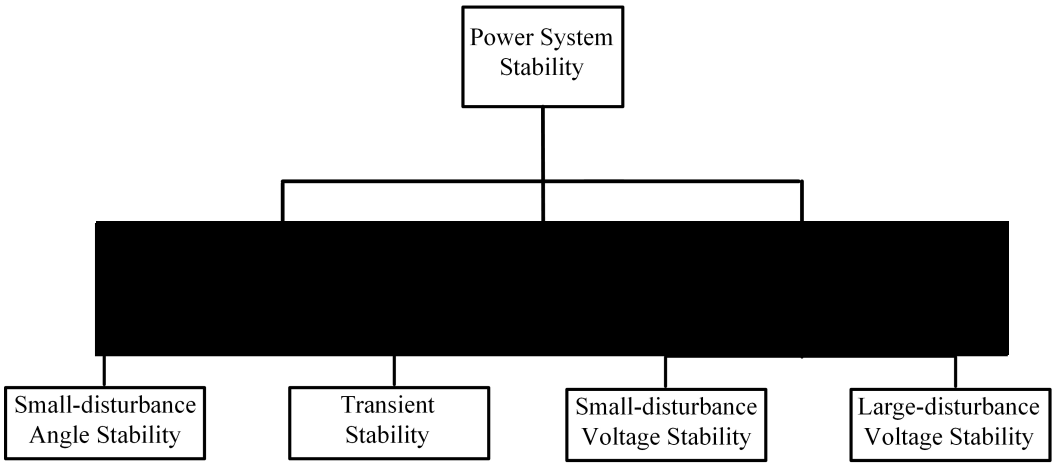

Fig. 1.2. Classification of power system stability [35].

small variations in the system loading) [32]. This disturbance is usually considered small enough, such that the resulting system response can be linearized for the purpose of analysis [3], [35]. The small-signal angle stability will be discussed further in chapter 2.

Transient stability (or large-disturbance angle stability) deals with the ability of the power system to maintain synchronism when subjected to large disturbances (e.g. 3-phase faults, loss of large SGs) [32], [35]. Time domain simulations are commonly employed to observe and analyze the non-linear response resulting from transient disturbances [3]. Loss of synchronism due to transient disturbances are usually evident from 2–3 seconds after the initial disturbance [3]. Although the angular stability of power systems dominated by SGs has been well studied, the impact of RESs on the power system angular stability has not been well established in literature [36]. Hence, an accurate and comprehensive study on the impact of RESs on the power system angular stability will be discussed in chapter 4.

1.2.2 Frequency stability

Frequency stability deals with the ability of the power system to maintain an acceptable frequency profile following a severe imbalance in the generation and load demand (e.g. loss of power infeed) [32]. The British National Grid stipulates that

the frequency f is maintained within 1% of its nominal value (i.e. $f = 1 \pm 0.01$ pu) [37]. Frequency is a global variable (i.e. the measured frequency at steady state has virtually same value throughout the system), which reflects the active power balance in the system [7], [11]. At the instant of a power imbalance in the system, SGs provide inertial response using the kinetic energy (K.E) stored in their rotor. This is followed by the governors action to drive the frequency to its nominal value by either increasing or decreasing the power output of the SG [3], [38]. For large disturbances, coordinated control of generation reserves and protection devices are required to ensure a desirable frequency response [32], [38]. Frequency instability often arises in the form of sustained frequency swings which may lead to tripping of loads [3]. The increasing penetration of intermittent RESs, will pose significant challenges on the frequency stability of the power system [7], [38]. Hence, appropriate control topologies must be employed by RESs to maintain the frequency stability of the power system.

1.2.3 Voltage stability

Voltage stability deals with the ability of the power system to maintain acceptable voltage levels at all buses after being subjected to disturbances [5], [32]. Voltage is a local variable, and it reflects the reactive power balance at a bus. Unlike frequency, different operating requirements are stipulated at different voltage levels [37]. The British National Grid stipulates the most stringent voltage V regulation at 400 kV (where $V = 1 \pm 0.05$ pu), while the least stringent voltage regulation is stipulated at 275 kV & 132 kV (where $V = 1 \pm 0.10$ pu). Voltage instability is common in heavily stressed systems, and often arises in the form of a progressive and uncontrollable increase or decrease of voltage at some buses [3], [5]. Voltage stability can be further subdivided into two categories (a) small-disturbance (b) large disturbance voltage stability.

Small-disturbance voltage stability refers to the ability of the power system to main-

tain steady voltages when subjected to minor disturbances (e.g. load perturbation) [5]. Large-disturbance voltage stability is concerned with the ability of the power system to maintain stability when subjected to large disturbances (e.g. 3-phase fault) [32]. Large disturbances can be accompanied by cascaded events which leads to voltage collapse [5]. It is noted that majority of the stability challenges arising from increasing RESs are associated with voltage instability [39]. Further, voltage and frequency disturbances will become more intertwined with increasing RESs, such that voltage disturbances will impact the frequency stability and vice-versa [40]. Hence, this research work focuses on the design of control paradigms for RESs which are resilient to power system disturbances (both small and large), thus ensuring the stability and reliability of the power system.

1.3 Original Contribution

Conventionally, large SGs inherently provide and maintain the power system inertia and short-circuit level at acceptable levels, to ensure stable, robust and reliable operation of the power system [7]. However, with the commitment of the UK to reduce 80% of its greenhouse emission by 2050, the power system must be decarbonized, with RESs replacing fossil-fueled SGs [18].

Recent reports from the British National Grid have shown that the increasing penetration of RESs has led to undesirable trends including increasing frequency and voltage oscillations, declining frequency response, reduction in short-circuit levels, system inertia and reactive power support [40]–[42]. Similar studies have also shown that the stable operating limit (or tipping point) for the instantaneous penetration of RESs in the Irish Grid is approximately 65% [43]. For the UK to meet the 2050 target [44], without jeopardizing the grid stability and reliability, RESs must employ control paradigms which offer similar robustness as the conventional SGs [15], [45]. Hence, the concept of virtual synchronous machines (VSMs), which mimic the desirable characteristics of the SG, has been proposed as a grid-friendly approach to

integrate RESs into the grid [34], [46]. Although various topologies have been proposed in literature for VSM implementation, most of the VSM models do not guarantee seamless transition between grid-connected and islanded mode of operation. Moreover, most of the detailed VSM models are very complex and computationally intensive, while some of the simpler models are not well adapted for operation in islanded mode. This thesis proffers a novel VSM strategy for the control of RESs, which enables:

(1) Seamless transition from grid-connected to islanded operation and vice-versa.

(2) Maximum power point tracking (MPPT) and load following power generation (LFPG) in grid-connected and islanded modes, respectively.

(3) Fault ride-through (FRT) capability during faults.

(4) Easy application to industrial standard *dq* current control approach, thus minimizing the required system changes.

To ensure optimal operation, a comprehensive analysis of the proposed VSM was performed in the event of small and large perturbations. A detailed mathematical model of the VSM was developed to enable accurate small-signal stability analysis. Also, the transient analysis was performed using a detailed non-linear model. From the resulting analysis, design guidelines were established to ensure optimal performance of the VSM in all operating modes.

Further, this thesis comprehensively analyzes the impact of VSMs on the power systems LFOs. This was achieved by:

(1) Developing a detailed two-machine test-bed which enables accurate evaluation of the LFO modes from the participating generators.

(2) Comprehensive analysis on the impact of replacing SGs with VSMs

(3) Comprehensive analysis of the LFO modes which exists in an all-VSM power system.

(4) Evaluation of the role of power system stabilizers (PSSs) in an all-VSM power system.

1.4 Thesis Outline

This thesis is structured as follows:

Chapter 2 provides a comprehensive review of the state-of-the art VSM topologies proposed in literature. A detailed explanation of the operation and control of each VSM topology is presented. The advantages and drawbacks of each VSM approach are comprehensively detailed. Also, the techniques for analyzing and damping the LFOs inherent in power systems are comprehensively reviewed. Further, the impact of VSMs on LFOs, including the solutions discussed in literature are comprehensively detailed. Finally, the research gaps and drawbacks of the previous studies are detailed.

Chapter 3 presents a VSM strategy for permanent magnet synchronous generator (PMSG) based wind turbines which enables seamless operation in all operating modes. It guarantees MPPT in grid-connected operation (assuming strong grid), LFPG in islanded operation, provides weak grid support, and FRT capability during faults. A small-signal stability analysis was performed to provide design guidelines for the VSM, while transient analysis were performed to confirm optimum operations in all scenarios.

Chapter 4 presents a detailed analysis on the impact of VSMs on the LFOs inherent in the power system. A detailed two-machine test-bed was developed to analyze the LFOs which exists when VSMs replace SGs. The role of PSSs in an all-VSM grid was comprehensively evaluated. The IEEE benchmark two-area four-machine system was employed to evaluate the system performance in the event of transient

disturbances.

Chapter 5 presents a general conclusion of the overall work and provides some recommendations for future works.

2. LITERATURE REVIEW

2.1 Introduction

The concept of grid-friendly converters with plug and play capabilities are envisaged as the solution to overcome the challenges associated with the increasing integration of RESs into the power system [34]. SGs inherently provide the necessary grid support, which ensures a reliable, robust and stable operation of the power system [11], [34], [39]. However, with the increasing replacement of SGs with RESs, operational difficulties and change in desirable system dynamics have been reported by grid operators [39], [47]. Hence, the concept of VSMs which mimic the dynamics of the SG have been proposed in literature [34], [46]. Further, owing to the similarities of the dynamics of the VSM with the SG, it is envisaged that the LFOs inherent in the conventional power system may also be present in a VSM dominated grid. Hence, this chapter provides a comprehensive review of the state-of-the art VSM concepts proposed in literature. Also, the impact of VSMs on LFOs, including the solutions discussed in literature are comprehensively detailed. Finally, the research gaps and drawbacks of the previous studies are discussed in the conclusion.

2.2 Review of VSM topologies

This section provides a comprehensive review of the state-of the art VSM topologies in literature, including the merits and drawbacks of each approach.

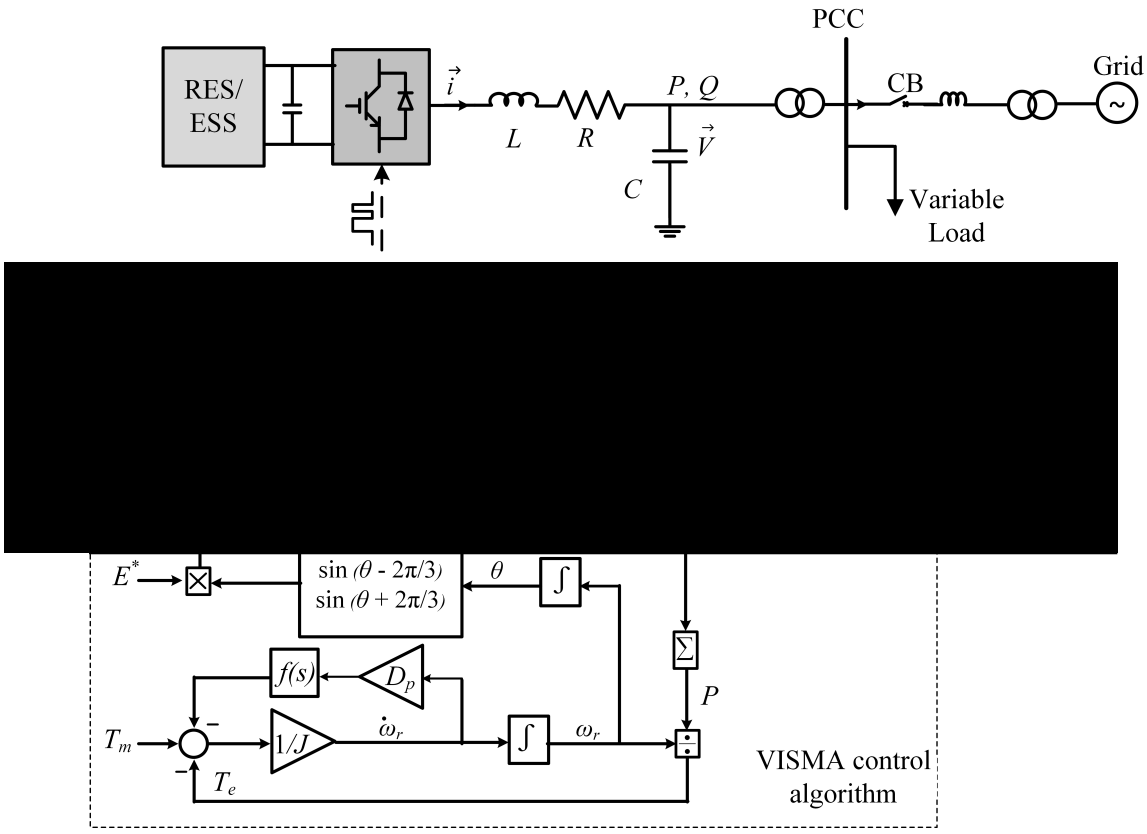

Fig. 2.1. Topology of VISMA and the grid interface [46].

2.2.1 VISMA

The pioneer VSM algorithm was presented in [46], [48] and termed VISMA. It employs the 5^{th} order model of the SG to fully capture the static and dynamic characteristics of the SG. The input and output of the VISMA algorithm, are the 3-phase measured voltage $\vec{V}$ and 3-phase reference current respectively $\vec{i}^*$. A fast hysteresis controller processes $\vec{i}^*$, to derive the desired VSM operation. Unlike the conventional SG, VISMA allows bi-directional flow of active and reactive power, which caters for energy storage applications. The topology of the VISMA is illustrated in Fig. 2.1, and is described by (2.1)–(2.3) [46]:

$$\vec{e} = \vec{V} + \vec{i}^* R_s + L_s \frac{d\vec{i}^*}{dt} \tag{2.1}$$

$$\omega_r = \int \frac{T_m - T_e}{J - D_p f(s)} \tag{2.2}$$

$$\theta = \int \omega_r dt \tag{2.3}$$

Where $\vec{e} = [e_a\ e_b\ e_c]^T$ is the induced electromotive force (EMF) in the stator winding (in *abc* frame), R_s is the stator resistance and L_s is the stator inductance. The measured current $\vec{i} = [i_a\ i_b\ i_c]^T$ is compared with $\vec{i}^* = [i_a^*\ i_b^*\ i_c^*]^T$ in the hysteresis controller. The notations J, ω_r, P, T_m, T_e, D_p, $f(s)$ and θ respectively represent the moment of inertia, virtual angular frequency, active power, mechanical torque, electromagnetic torque, damping coefficient, phase compensation term and phase angle. The induced EMF reference E^* determines the magnitude of $\vec{e}$. Although the VISMA offers considerable support for the grid-connected operation, the voltage in islanded mode is highly distorted for no-load (and presumably low-load) conditions. From Fig. 2.1, it is also observed that the VISMA does not employ any control for the reactive power Q injected to the grid. Furthermore, when the current tracking error from the hysteresis controller is large, the VISMA does not satisfactorily replicate the desired SG dynamics [34]. Ref. [49] proposed enhancing the islanded operation of the VISMA by implementing a PWM based control. To achieve this, the input and output parameters of the VISMA were swapped such that; the measured grid current and grid voltage are the input and output parameter respectively. Although this alteration improved performance in the islanded mode, the model employs a differentiator to obtain the output voltage from the current, which may lead to instability (since differentiators have a tendency to amplify noises and harmonics). Ref. [50] proposed mitigating grid harmonics by synthesizing the difference between $\vec{e}$ and V by a distortion compensation factor, prior to processing by the hysteresis controller. Ref. [51] observed that neglecting the transient and sub-transient dynamics of the stator in the VISMA design resulted in undesirable transient performance. Hence, the authors [51] proposed employing an auxiliary controller in parallel with the VISMA. The auxiliary controller employs an exact replica of the VISMA but with easily adjustable parameters based on the change in operating conditions. Although this approach improves the transient performance, it increases the system complexity and significantly increases the computational burden on the digital signal processor.

2.2.2 Synchronverter

Ref. [34], [52] proposed a VSM strategy, which offers the same dynamics as the SG from the grid point of view. Similar to the VISMA, this VSM also employs a detailed mathematical model of the SG and is termed a synchronverter. It embodies a round rotor machine (i.e. the direct and quadrature axis have the same synchronous reactance), but neglects the dampers, eddy current and iron core losses. The synchronverter is equipped with frequency and voltage droop control loops which enable parallel operation of multiple units. The frequency droop mechanism is achieved by comparing ω_r with the angular frequency reference ω^* as shown in Fig. 2.2. Here, D_p provides both damping and $P-\omega$ droop. Unlike the VISMA, the synchronverter has a dedicated control loop for Q. The systems voltage is regulated by comparing the measured voltage V with the reference voltage V^*. The error in the measured voltage is added to the reactive power control loop as shown in Fig. 2.2. The voltage drooping coefficient D_q determines the $V-Q$ droop. The notation $\langle\cdot,\cdot\rangle$ denotes the inner product in $\mathbb{R}^3$, and the overall dynamics of the synchronverter can be represented by (2.4)–(2.9) [34]:

$$\frac{d\omega_r}{dt} = \frac{1}{J}(T_m - T_e - D_p(\omega^* - \omega_r)) \tag{2.4}$$

$$T_e = -M_f i_f \langle \vec{i}, \widetilde{\sin}\theta \rangle \tag{2.5}$$

$$E = \omega_r M_f i_f \tag{2.6}$$

$$e = E\widetilde{\sin}\theta \tag{2.7}$$

$$P = E\langle \vec{i}, \widetilde{\sin}\theta \rangle \tag{2.8}$$

$$Q = -E\langle \vec{i}, \widetilde{\cos}\theta \rangle \tag{2.9}$$

Where P^*, Q^*, E, i_f, and M_f represents the reference active power, reference reactive power, amplitude of the induced EMF, field excitation current, and maximum mutual inductance between the stator windings and the field winding.

The notations $\widetilde{\sin}$ and $\widetilde{\cos}$ represent:

$$\widetilde{\sin}\theta = \begin{bmatrix} sin\theta \\ sin(\theta - \frac{2\pi}{3}) \\ sin(\theta - \frac{4\pi}{3}) \end{bmatrix}, \ \widetilde{\cos}\theta = \begin{bmatrix} cos\theta \\ cos(\theta - \frac{2\pi}{3}) \\ cos(\theta - \frac{4\pi}{3}) \end{bmatrix} \tag{2.10}$$

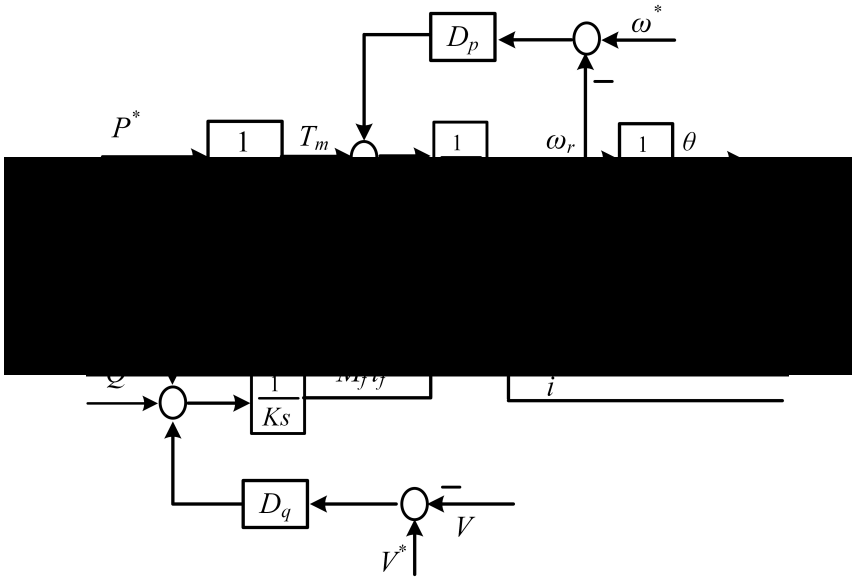

Fig. 2.2. Control topology of the synchronverter [34].

An advantage of the synchronverter over the SG, is the freedom of tuning system parameters as required (i.e. parameters such as inertia and mutual inductances are not physical) to obtain the desired performance. However, the synchronverter also exhibits all the undesirable phenomena present in the SG including: loss of stability due to under-excitation, and hunting phenomena. It is also observed that the synchronverter (see Fig. 2.2) employs a pure integrator to generate θ. However, since the integrator accumulates the previous input states over time, this will cause a challenge in reconnection to the grid from islanding, when the integrator must be reset to achieve synchronization. This necessitates a communication from the PCC to the VSM to reset the integrator when re-connecting to the grid. Otherwise, there might be a phase shift between the VSM unit and the grid, which can even trip their operation. Several improvements on the synchronverter have been proposed in literature [52]–[59].

Ref. [52] augmented the structure of the synchronverter to achieve self-synchronizing capability, without the need of a phase-locked loop (PLL). The main principle of this concept is to drive the phase difference $\Delta\theta$ between e from the synchronverter, and the grid voltage V_{PCC} to zero, while simultaneously ensuring equal voltage magnitude (i.e. $|E| = |V_{PCC}|$). To achieve this, a synchronization mode is defined; P and Q are set to zero, and proportional integral (PI) controllers are used to drive $\Delta\theta$ to zero. Doing so solves the need to

reset the integrator at the time of grid reconnection, at the price of creating an intermediate mode that interrupts the operation of the VSM ($P = Q = 0$). In addition, a virtual impedance is employed to drive the difference between $|V_{PCC}|$ and $|E|$ to zero. Ref. [53] performed a stability analysis of the self-synchronizing synchronverter to facilitate optimal parameter tuning. Although, this topology [52], [53] enables self-synchronization with the grid, it adds complexity to the the control paradigm. Furthermore, it does not allow seamless operation, as it necessitates a change in normal operating condition (i.e. P and Q must be set to zero before re-synchronization). Ref. [54] observed that, the synchronverter [34] lacks some degree of control freedom, as it is impossible to vary the response speed of the active power loop without altering the $P - \omega$ droop (which is normally fixed by the grid requirements). Hence, an additional damping correction loop was employed which enables the adjustment of the active power loop (APL) response without impacting the frequency droop. The authors also suggested that this technique can improve the stability of the synchronverter by reducing the active and reactive power coupling, when a fast APL response is employed.

Ref. [55] proposed a technique to limit the inrush current in the synchronverter during short-circuit fault. An inrush current detection circuit was employed to detect large inrush current during fault, thereafter the synchronverter control is switched to enable the operation of a fast hysteresis controller to limit the inrush current. Although this technique is suitable for symmetrical fault, its applicability to asymmetric fault was not discussed. Moreover, the fault detection circuit increases the system complexity. The stable operating boundary of the synchronverter was analyzed in [56], [57]. Ref. [58]–[60] proposed employing virtual impedance to improve the synchronverter stability, while Ref. [61] adapted the synchronverter for high voltage direct current systems. It is noted that most of the improvements for the synchronverter cannot be implemented simultaneously (e.g. the self-synchronizing control [52] cannot be simultaneously employed with the inrush current protection scheme [55]); hence, they do not provide a comprehensive solution. In addition, the complex mathematical computations required for the implementation of the control algorithm may lead to numerical instability [62].

2.2.3 ISE Lab VSM

Ref. [63] proposed a simplified model of the SG for VSM implementation. This VSM has also been termed the "ISE lab" VSM in literature [62]–[65]. In contrast to the VISMA and synchronverter which employ the detailed dynamics of the SG, the ISE lab VSM only considers the swing equation of the SG. It employs a voltage-mode control [66], where θ and E are modulated to regulate P and Q respectively. The dynamics of the ISE lab VSM is represented by (2.11) – (2.13), and is illustrated in Fig. 2.3 [67].

$$P^* - P = J\omega_r \frac{d\omega_r}{dt} - D\Delta\omega \tag{2.11}$$

$$P^* = P_0 + K_p\Delta\omega\left(\frac{1}{1+T_d s}\right) \tag{2.12}$$

$$Q^* = Q_0 + K_q\Delta V \tag{2.13}$$

In Fig. 2.3, ω_r is solved from the swing equation (2.11) by iteration [67], while ω is the measured angular frequency obtained from a PLL. The swing equation is calculated at every control cycle to emulate the SG's inertia [62]. The governor block is a $\omega - P$ droop which regulates the reference power P^* based on the angular frequency deviation $\Delta\omega$ (i.e. $\Delta\omega = \omega - \omega_r$). The governor employs a low-pass filter (LPF) with a time constant T_d, which emulates the mechanical delay in the governor of the SG. The ISE lab VSM was augmented with a reactive power loop in [68]. The Q-droop block (see Fig. 2.3) regulates the reactive power flow in response to voltage deviation (i.e. $\Delta V = V^* - V$). The droop gains of the active and reactive power loop are represented by K_p and K_q respectively. The preset active power P_0 and reactive power Q_0 are determined by the VSM rating and the ESOs requirements. Although this VSM is relatively simpler than the VISMA and synchronverter [34], [46], it suffers from reactive power sharing error and transient active power sharing error. Also, since the ISE lab VSM (see Fig. 2.3) employs a voltage-mode control, it has no inherent over-current protection. This can lead to undesirable and unpredictable current transients, which can damage the power electronic converter (PEC) [66]. Improvements on the ISE lab VSM were proposed in [67], [69]–[71].

Ref. [67] employed a virtual inductance to enhance the transient active power sharing error. Further, an inverse voltage droop (V–Q droop) control with a common ac-bus volt-

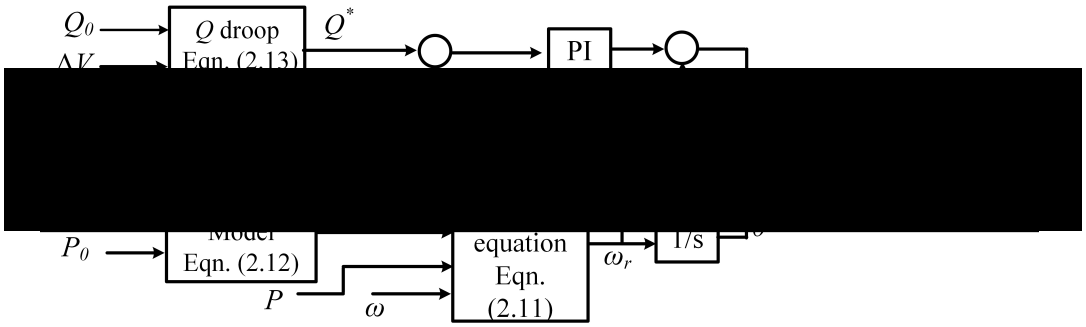

Fig. 2.3. Topology of the ISE Lab VSM [67].

age estimation was employed to achieve accurate reactive power sharing. However, if the estimated ac-bus voltage is inaccurate, the reactive power sharing will worsen. In [69], a particle swarm optimization algorithm was developed to optimally tune the system parameters to minimize phase angle deviation and achieve smooth transitions after disturbances for parallel operation of the VSM. Ref. [70], employed an alternating inertia on the VSM to damp LFOs. Ref. [71] proposed a FRT strategy for the ISE lab VSM. This was achieved by replacing the reactive power loop with a direct measurement of V, such that a voltage sag at PCC is directly reflected at E. Further, P is controlled inversely proportional to V, while J is varied in response to changes in ω, to achieve satisfactory performance. However, this topology increases the VSM complexity. Further, the proposed topology is unable to inject fast-fault current as stipulated in [37].

2.2.4 VSM0H

Ref. [72] proposed a zero inertia VSM control termed VSM0H. The topology adopted for the VSM0H is similar to the conventional droop control. However, it does not have an inner current control loop and PI controllers. The frequency and voltage are droop regulated in proportion to the active and reactive power demand respectively. Fig. 2.4 illustrates the topology of the VSM0H and the dynamics of the droop block is represented by (2.14) and (2.15) below [72]:

$$\omega_r = \omega^* + K_p(P^* - P)\left(\frac{1}{1+T_d s}\right) \tag{2.14}$$

$$E = E^* + K_q(Q^* - Q) \tag{2.15}$$

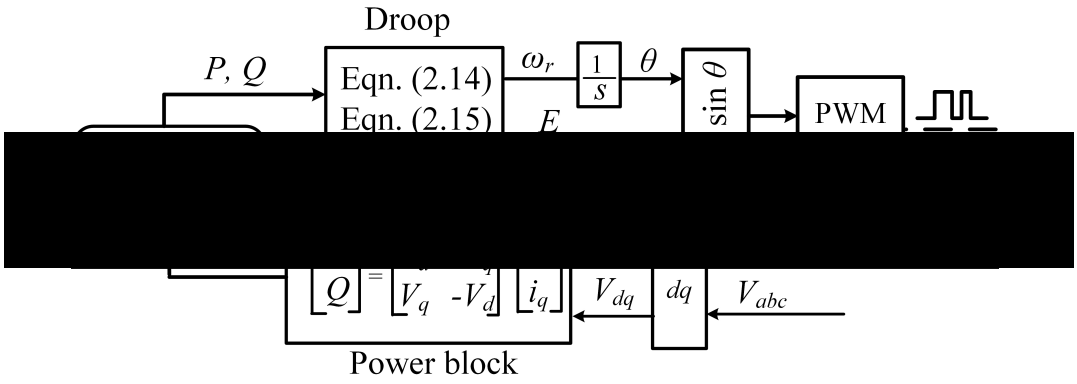

Fig. 2.4. Control topology of the VSM0H [72].

The VSM0H is designed with a low control bandwidth (less than 50 Hz) to minimize voltage harmonics. Although the VSM0H is not equipped with synthetic inertia, it has a fast acting frequency droop slope. The capability of the VSM0H to operate in a scenario of 100% RESs penetration was demonstrated using a simplified power system model. However, an infinite bus is required to initialize the system. Similar to the synchronverter, the pure integrator on the VSM0H needs to be reset at the time of reconnecting the grid from islanding. Ref. [73] augmented the VSM0H with a phase angle correction block to enable soft-start. This was followed up by an experimental validation; however, the FRT capability was not investigated. An improvement on the VSM0H was proposed in [74] to add synthetic inertia into the VSM0H; however, this causes the system to resonate around certain frequencies (2–5 Hz). Further, since the VSM0H employs a voltage-mode control, it has no inherent over-current protection.

2.2.5 Algebraic Model of VSM

Ref. [75] proposed an algebraic model of the VSM, which employs the phasor representation of the SG (in steady state), while the dynamic equations of the SG are neglected. Similar to the synchronverter, the algebraic VSM also embodies a round rotor machine. It is assumed that the VSM impedance is low for a wide range of frequencies to enable smooth operation in grid and islanded mode. A major advantage of this VSM model over the previous models (e.g. synchronverter, VSM0H) is the inherent over-current protection provided by the current loop.

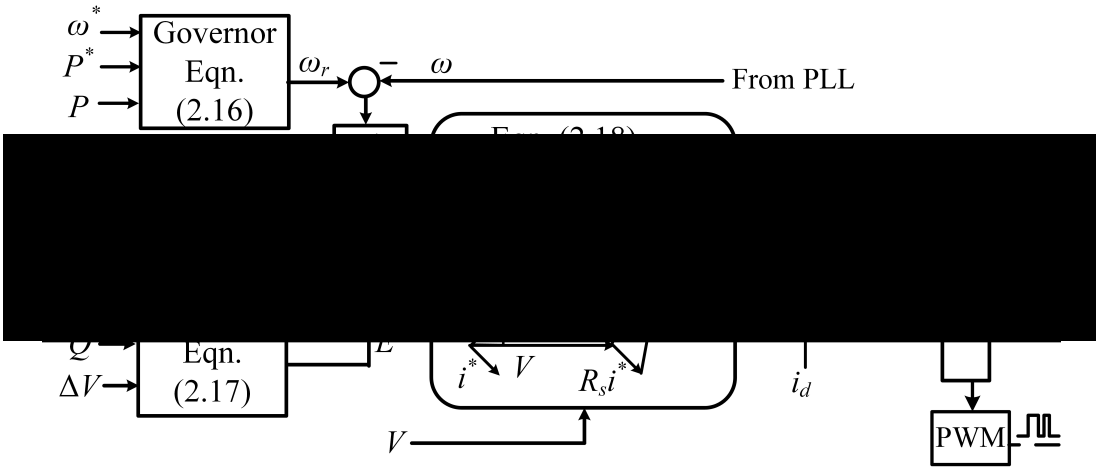

Fig. 2.5. Control topology of the Algebraic VSM model [75].

The structure of the algebraic VSM is illustrated in Fig. 2.5. The dynamics of the governor (2.16) and AVR (2.17) can be represented by [75]:

$$\omega_r = \omega^* + K_p(P^* - P)\left(\frac{1}{1+T_d s}\right) \tag{2.16}$$

$$E = \left[\Delta V + K_q(Q^* - Q)\left(\frac{1}{1+T_d s}\right)\right]\left(K_p + \frac{K_I}{s}\right) \tag{2.17}$$

The notations E_{dq}, V^*_{dq}, V_{dq}, i^*_{dq} and i_{dq} are the dq-axis representation of the VSM's induced EMF, reference voltage, measured voltage, reference current and measured current respectively. The relationship between E_{dq}, V_{dq} and i^*_{dq} are described in (2.18). The equations for the abc/dq transformations are illustrated in (A.1) and (A.2). The admittance Y is a function of the generator's synchronous reactance X_s and R_s. Here, X_s is a constant, whose magnitude is independent of variations in ω. The magnitude of E is a function of V^* and Q^* from the AVR (see Fig. 2.5). Similarly, ω_r is a function of P^* and ω^*. The magnitude of P and Q can be obtained as described in (A.3) and (A.4) respectively. Also, θ is obtained from the integral of the difference between the virtual angular frequency provided by the governor ω_r and ω from the PLL. The main drawback of this scheme is the need to switch the control topology during transition from grid to islanded mode of operation which undermines seamless operation of the system especially in cases of fault.

$$\begin{bmatrix} i_d^* \\ i_q^* \end{bmatrix} = Y \left\{ \begin{bmatrix} E_d \\ E_q \end{bmatrix} - \begin{bmatrix} V_d \\ V_q \end{bmatrix} \right\}$$

$$\begin{bmatrix} E_d \\ E_q \end{bmatrix} = E \begin{bmatrix} cos\theta \\ sin\theta \end{bmatrix}, \; Y = \frac{1}{{R_s}^2 + {X_s}^2} \begin{bmatrix} R_s & X \\ -X_s & R_s \end{bmatrix} \tag{2.18}$$

2.2.6 Power synchronization controller

Ref. [76] proposed a VSM which is capable of emulating the self-synchronizing capability of the SG and is termed a power synchronization controller (PSC). The active power loop (also termed as the power synchronization loop in this topology) directly controls the phase angle deviation $\Delta\theta$. The summation of the reference phase angle θ^* and $\Delta\theta$ generates θ (i.e. $\theta = \theta^* + \Delta\theta$). The dynamics of the PSC can be represented by (2.19) [76]:

$$\begin{aligned} \frac{d\Delta\theta}{dt} &= K_p(P^* - P) \\ \Delta E &= K_v(V^* - V)\left(\frac{1}{1 + T_d s}\right) \end{aligned} \tag{2.19}$$

The voltage control is similar to the conventional droop [27], and the voltage droop gain is represented by K_v. The LPF block has a time constant T_d. A fundamental drawback of the PSC is the absence of a current control loop, which makes the PEC vulnerable to over-current events [66]. It also suffers from large steady state error [77]. The PSC was augmented with a current controller in [78], [79] and the weak grid operation and FRT capability were demonstrated. In [80], the power loop was modified to enable independent tuning of the $P - \omega$ droop, damping and inertia of the power loop; this was achieved by employing a lead-lag compensator to emulate the swing equation of the SG. Ref. [81] proposed emulating the impedance of the SG, by augmenting the PSC with a virtual admittance. The virtual admittance improves the dynamic performance of the PSC and enables smooth transition from grid connected mode to islanded mode. However, the grid re-synchronization was not evaluated. In the aforementioned PSC topologies, grid re-synchronization will be very challenging, due to the absence of a frequency detection

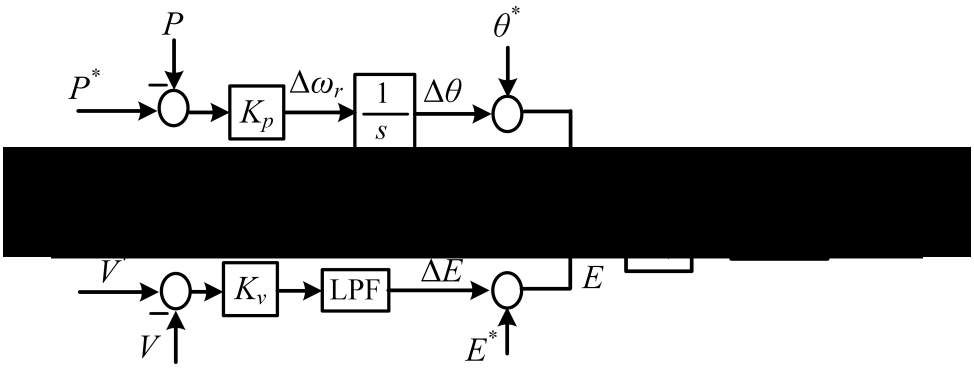

Fig. 2.6. Power Synchronization controller [76].

circuit (e.g. PLL). A presumable justification for the elimination of the frequency detection circuit will be that $f \approx 1$pu. However, in practice f can vary within the nominal value stipulated in the grid code (e.g. British National Grid stipulates $\Delta f \leq \pm$ 0.01 pu) [37]. Therefore, if the grid frequency is, for example, 49.5 Hz, while the VSM reference uses the nominal 50 Hz (as there is no frequency detector), there will be a phase difference (hence a circulating current) that can interrupt the operation. Further, in islanded operation, technical and economical constraints can compel system operators to employ less stringent regulation of V and f [20]. Hence, an attempt to re-synchronize the PEC when V, f and θ are not within the stipulated standards will lead to large transients which can damage the PEC [82], [83]. Ref. [84] proposed a technique to enable smooth re-synchronization of the PSC to the grid. It employs a PLL at PCC to obtain the phase angle, angular frequency ω and voltage V_{PCC} of the grid, while the PSC is in islanded operation. Thereafter, PI controllers are employed on the active power and voltage loop to ensure $\omega = \omega_r$ and $|E| = |V_{PCC}|$, before reconnection to the grid. A major drawback of this approach is that it also requires switch of controllers from islanded to grid-connected operation. Also, the topologies in [80], [81] employ open loop voltage control, which will impact the reactive power sharing amongst multiple systems.

2.2.7 Synchronous Voltage controller

Ref. [85] proposed a voltage based approach for SG emulation termed SynVC. Distinct from the preceeding VSM models (e.g. PSC, ISE lab VSM), where the SG emulation was

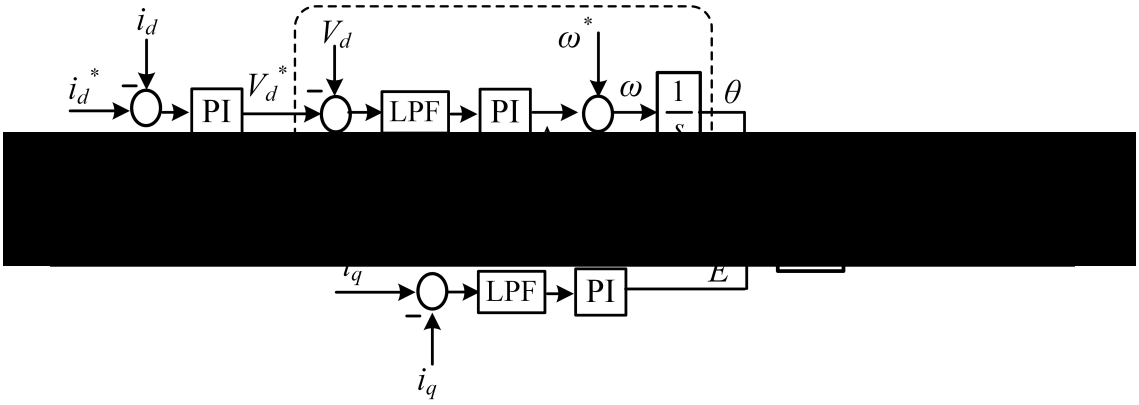

Fig. 2.7. Topology of the synchronous voltage controller [85].

realized on the power loop, the SynVC actualizes the SG emulation on the voltage loop. The overall control of the SynVC is achieved using a joint d-axis and joint q-axis control loop. The joint d-axis control loop regulates i_d, V_d, and provides a virtual inertia and virtual PLL. Unlike the conventional droop control [27], this topology employs an outer current loop, while the voltage loop is the inner loop. The outer current loop indirectly regulates the active power flow in the SynVC. As illustrated in Fig. 2.7, the error of i_d is processed by the PI controller to generate V_d^*. Further, the deviation of V_d (i.e. $\Delta V_d = V_d^* - V_d$) is processed by the virtual PLL to generate the phase angle. The LPF in the virtual PLL adds a virtual inertia and damping effect, and also attenuates PWM switching effect. The dynamics of the virtual PLL and joint q-axis is given by (2.20)–(2.22) [85]:

$$\theta = \int \left(\omega^* + \Delta\omega\right) \tag{2.20}$$

$$\Delta\omega = \left(K_p + \frac{K_I}{s}\right)\left(\frac{\Delta V_d}{1 + T_d s}\right) \tag{2.21}$$

$$E = (i_q^* - i_q)\left(K_p + \frac{K_I}{s}\right)\left(\frac{1}{1 + T_d s}\right) \tag{2.22}$$

The joint q-axis control loop, regulates the voltage magnitude via i_q. The LPF on this control loop mimics the dynamics of the RL excitation circuit of the rotor in the SG. The joint d-axis and q-axis respectively perform the role of a virtual governor and virtual AVR. A major stability concern for the SynVC, is the deployment of V_d instead of V_q for frequency estimation. Since V_d undergoes much larger excursions than V_q during faults, the SynVC may be susceptible to instability or loss of synchronization post-fault. Also, although it was demonstrated that the SynVC is able to track changes in the grid variables

(i.e. V and f) in grid-connected mode, the re-synchronization capability from an islanded mode was not investigated. An alternative to the SynVC was proposed in [77], where the SG emulation was realized on the current loop. The frequency loop directly controls the phase angle, and the reference current is synthesized from the phase angle. Although this topology has high degree of control freedom, the direct alteration of the phase angle may cause re-synchronization and stability problems [86].

2.2.8 Inducverter

The inducverter is designed to mimic the dynamics of the induction generator [87]. Although the inducverter is not *synchronous* in operation, it aims to achieve the core objective of the VSM i.e. mimic the desired characteristics of conventional generators to improve robustness of the grid [87]. The salient feature of the inducverter is its soft- and auto-synchronizing capability. The inducverter consists of two principal units: the current damping/synchronization unit and the core controller unit. The principal function of the current damping/synchronization unit is to accurately estimate the grid frequency and phase angle using local information, thus enabling soft- and auto-synchronization without the need of a dedicated synchronizing unit or PLL. Figure 2.8 illustrates the topology of the inducverter, where the angular frequency deviation ω_{slip} is estimated as a function of i_d and i_q. Hence, ω_{slip} varies in response to variations in the output power and grid frequency to enable auto-synchronization. The dynamics of the inducverter can be expressed by (2.23)–(2.26) [87]:

$$i_d^* = (P^* - P)\left(K_p + \frac{K_I}{s}\right) \tag{2.23}$$

$$i_q^* = (Q^* - Q)\left(K_p + \frac{K_I}{s}\right) \tag{2.24}$$

$$J\frac{d\omega_r}{dt} = T_m - T_e + D_{\omega_r} \tag{2.25}$$

$$\theta = \int (\omega_r + \omega_{slip} + \omega^*) \tag{2.26}$$

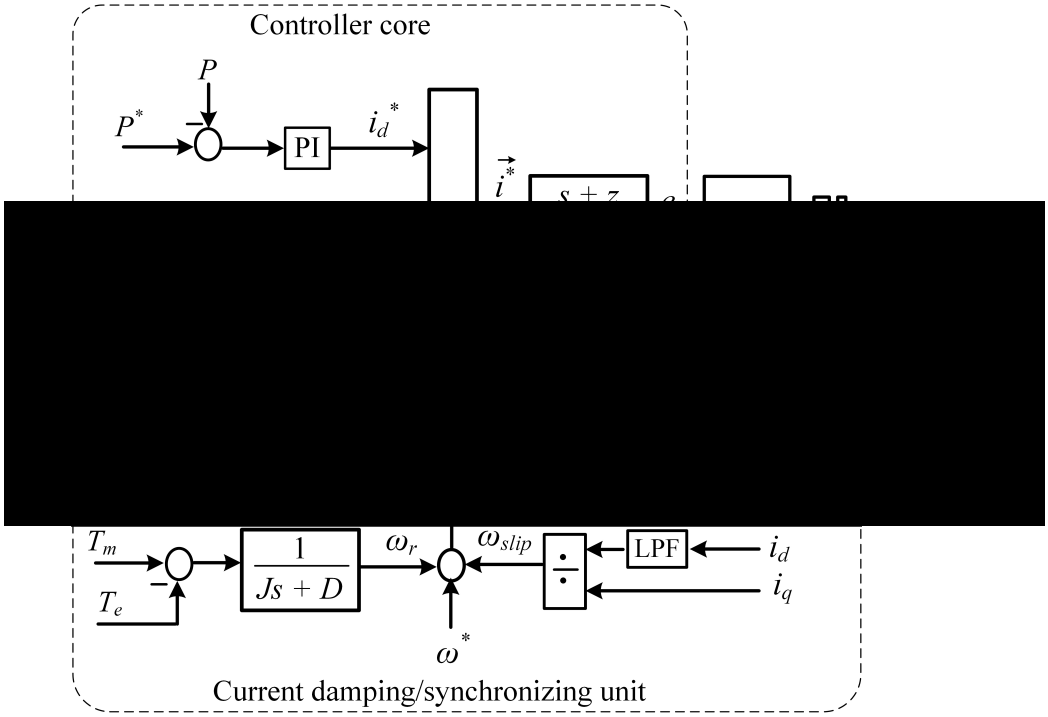

Fig. 2.8. Topology of the Inducverter [87].

The core controller is realized using a hybrid dq/abc controller as illustrated in Fig. 2.8. The errors of the active and reactive powers are processed via PI controllers to generate the reference current in dq-frame. The reference current is transformed to the equivalent abc frame using the angle generated from the current damping/synchronization controller. The voltage input to the PWM is obtained from $\vec{i^*}$ using the virtual impedance. The virtual impedance is realized using an adaptive lead or lag compensator, to enhance either the transient response or steady state error respectively. In the proposed inducverter, the core controller, feeds constant amount of real and reactive powers to the grid regardless of variations in grid parameters. Although this may be advantageous for some applications, exporting constant power irrespective of voltage deviation can cause negative resistance on the grid, hence leading to instability [88]. Moreover, since the power output is kept constant regardless of grid variation, the inducverter is unable to provide fast-fault current as stipulated in [37]. From Fig. 2.8, it is observed that the voltage and current control are both open loop; hence, the voltage and current may exhibit undesirable transients during large disturbance [66]. Further, although the inducverter enables soft connection to the grid, its islanded operation was not investigated.

2.2.9 VSYNC

Ref. [89]–[91] proposed a VSM topology termed VSYNC, which employs a PLL-based emulation of the SG. As illustrated in Fig. 2.9, VSYNC employs a simple topology, which is not computationally intensive. The PLL generates P^* from ω as shown in Fig. 2.9. This VSM topology does not implement any reactive power control and the system dynamics is described by (2.27)–(2.29) [89]:

$$P^* = P_0 + K_i \frac{d\Delta\omega}{dt} + K_p \Delta\omega \tag{2.27}$$

$$i_d^* = P^* \left(\frac{2V_d}{3(V_d^2 + V_q^2)} \right) \tag{2.28}$$

$$i_q^* = P^* \left(\frac{2V_q}{3(V_d^2 + V_q^2)} \right) \tag{2.29}$$

The operability of VSYNC was demonstrated via real time simulations and field tests in [92] and [93] respectively. An improvement on this topology was presented in [94], where an energy management system was implemented to enable multiple VSMs support the grid proportionally without communication. This algorithm ensures sufficient leverage for energy absorption and injection during disturbance, while preventing deep discharge or overcharge of the local ESSs. A major drawback of VSYNC is the absence of a voltage control loop. Hence, it is not applicable for islanded operations, and cannot provide dynamic voltage support to the grid.

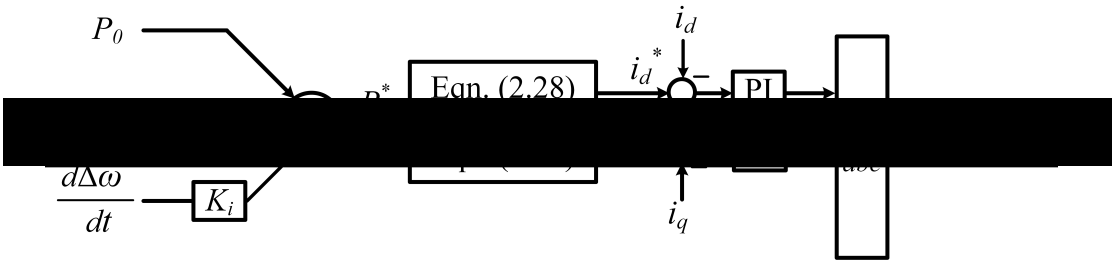

Fig. 2.9. Control topology of VSYNC [89].

2.2.10 Summary of VSM topologies

It is envisaged that an ideal VSM will exhibit specific characteristics which guarantee the global stability of the power system. At the moment, no specific VSM topology has been

Tab. 2.1. Summary of VSM topologies

Topology	Key features					
	Seamless transition between grid and islanded mode	Frequency detector (e.g. PLL)	Voltage control /AVR	Inherent over-current protection	Fault Ride-Through	Black-start capability
VISMA	Not investigated	Required	Closed loop	Present	Not investigated	Yes
Synchronverter	Not realizable	Not required in [52], [53]	Closed loop	Achievable in [55]	Achievable in [55]	Yes
ISE Lab VSM	Not investigated	Required	Closed loop	None	Achievable in [71]	Yes
VSM0H	Not investigated	Required	Closed loop	None	Not investigated	Yes
Algebraic VSM	Not realizable	Required	Closed loop	Present	Not investigated	Yes
Power Synchronization Controller	Not investigated	Not required in [78],[79], [80],[81]	Closed loop except [80],[81]	Present except [76]	Yes	Yes
Synchronous voltage	Not investigated	Not required	Closed loop	Present	Not investigated	Yes
Inducverter	Not investigated	Not required	Open loop	Present	Yes	Yes
VSYNC VSM	Not realizable	Required	None	Present	Not investigated	Not realizable

stipulated as a recommended standard; however, some ESOs [47], [95], [96] have drafted some desirable technical requirements for VSMs, which include: (i) seamless operation in grid-connected and islanded mode (ii) inherent over-current protection (iii) dynamic voltage and frequency support (iv) FRT (v) black-start capability. Based on this criteria, Table 3.1 provides a birds-eye view of the key features and drawback of the VSM topologies discussed in literature. Since all the VSM topologies provide frequency support, this is not highlighted in Table 3.1, and not discussed further.

From Table 3.1, it is observed that most of the topologies proposed in literature may not guarantee seamless transition from grid-connected to islanded operation and (vice-versa). For most of the VSM topologies (e.g. VISMA, VSM0H), the grid re-synchronization (i.e. from islanding) was not investigated, while some VSM topologies cannot achieve seamless transition. For the modified PSC model [84] which employs a PLL for soft-synchronization, a switch of control paradigm is required before re-synchronization. Similarly, the self-synchronizing synchronverter requires a change in operating point (P and $Q = 0$) prior to reconnection with the grid [52]. Hence, although the self-synchronizing synchronverter guarantees soft-synchronization without a frequency detector, the transition process is not seamless. The inducverter also guarantees soft-synchronization; however, the transition to islanded operation was not investigated.

It is also observed that some VSM topologies (e.g. PSC, inducverter) do not employ any frequency detector (e.g. PLL) for synchronization. This is due to the notion that PLLs can be difficult to tune, and can negatively impact the VSM stability in weak grid conditions [52], [76]. The self-synchronizing synchronverter aligns the voltage and phase angle of the PEC with the grid using auxiliary control loops, while the inducverter estimates the grid frequency to ensure soft-synchronization. However, for the modified PSC models [78], [79], where no frequency estimation is employed, there is a potential risk of out-of-phase synchronization, which can damage the PECs [82]. In practice, synchronism devices (e.g. phase measurement units, synchro-check relays) are often employed to match the parameters of SGs (i.e. V, f, θ) prior to synchronization or parallel operation [97], [98]. Automated synchronism devices are capable of facilitating precise closure of the mains switch (i.e. at $\Delta\theta = 0°$), thus achieving soft-synchronization [98]. Similarly, it is

essential for VSMs to employ a form of frequency detection/estimation scheme to ensure soft-synchronization with the grid or adjacent microgrids. PLLs have been the standard device for synchronizing PECs to the grid [86], [87]. Although, it is often argued that PLLs can negatively impact the VSM stability, recent reports have demonstrated that optimally tuned PLLs can improve system stability in weak grids [99]. Also, for VSM schemes employing in-built frequency estimation schemes (e.g. synchronous voltage controller), it is essential to validate the soft-synchronization capability.

It is also observed (see Table 3.1) that in view of mimicking the SGs, some VSM topologies (e.g. synchronverter, VSM0H) employ voltage-mode control. Hence, these topologies have no inherent over-current protection, due to the absence of a current control loop. It is noted that SGs have high over-current tolerance and are capable of injecting fast-fault currents beyond the SGs rating (e.g. $5-7$ pu) [100]. However, for VSMs with limited over-current capability, it essential to employ appropriate control loops to provide over-current protection, which is difficult (if not impossible) without a current loop.

According to the revised grid codes, RESs are mandated to remain connected during faults, and inject a certain amount of reactive power into the grid [37], [101]. The FRT capability of some VSMs (e.g. PSC, inducverter) were demonstrated, while others were not investigated. The FRT capability of the modified ISE lab VSM was demonstrated in [71]. However, this was achieved by eliminating the voltage control loop; hence, it does not inject reactive power as stipulated by the grid code [37]. It is noted that dynamic voltage support from VSMs is essential to contribute to the power systems SCL, and to facilitate the post-disturbance recovery of the power system [39], [47]. Most VSM topologies employ closed loop voltage control, except the modified PSC [80], [81], inducverter and VSYNC. The PSC and inducverter which employ open loop voltage control will be prone to circulating currents, which results from poor reactive power sharing between multiple PECs [27]. Similarly, the VSYNC will not be capable of meeting the stipulated FRT requirement, due to the absence of a voltage/AVR loop. Hence, the VSYNC, inducverter and PSC must be augmented with closed loop voltage controllers to facilitate the integration to the grid.

Black-start capability is also a crucial feature for VSMs, to facilitate smooth transition to

a net-zero grid [102]. It is assumed that VSMs capable of establishing independent regulation of V and f (grid-forming) can perform black-start operation [103]. From Table 3.1, it is observed that all the VSM topologies are capable of black-start except the VSYNC, which does not employ a voltage control loop. Hence, the VSYNC needs to be augmented with voltage control loop to enable black-start capability. Further, although it is expected that VSMs with grid-forming capability can perform black-start, it is essential for this capability to be verified via simulations in islanded operating mode [104].

Although several VSM topologies have been proposed in literature, some VSM topologies require further modifications to meet the grid requirement [37]. Also, the capabilities of some VSMs have not been validated for contingencies (e.g. fault, blackout). It is also noted that VSMs employing complex algorithms (e.g. VISMA, synchronverter and inducverter) are computationally intensive, difficult to implement in real time and susceptible to numerical instability [62]. On the other hand, some of the VSMs employing simpler models (e.g. VSYNC) are not well adapted for islanded operation. Further, in most of the previous works, the required guidelines for designing and tuning the VSMs have not been discussed. From a stability point of view, this information is very crucial, as improper tuning of VSM controllers can lead to oscillatory response and undermine the overall grid stability. In addition, details of the energy source (e.g. wind/solar PV) were omitted; hence, energy management issues such as MPPT in grid-connected mode and LFPG in islanded mode cannot be investigated.

In light of the gaps in the previous topologies, a novel VSM topology which performs seamlessly in all operating modes while achieving the desirable operational characteristics highlighted in Table 3.1 is proposed in this thesis, and will be comprehensively discussed and analyzed in chapter 3.

2.3 Low-Frequency Oscillations in Power Systems

The increasing penetration of RESs has a significant impact on the power system dynamics [33]. A crucial phenomena inherent in power systems is the LFOs [3], [6]. LFOs mainly impact the power-angular relationship between interconnected SGs, and are usually in

the range of 0.1–2 Hz; where the inter-area and local modes oscillate within the range of 0.1–0.7 Hz and 0.7–2.0 Hz respectively [33], [3]. The inter-area modes are due to SGs in one generating station swinging against SGs in another region of the network [3], while the local modes are due to SGs in one generating station swinging against the rest of the power system [3]. LFOs were first observed in the Northern American power network in 1964 during a trial interconnection of the Northwest Power Pool and the Southwest Power Pool [105]. Since then, several incidents resulting from LFOs have been reported in power transmission networks around the world [106]. In severe cases, large disturbances (e.g. 3-phase fault) exacerbate poorly damped LFOs, leading to loss of synchronism and subsequent collapse of the power system [3]. Hence, to maintain the stability and reliability of the grid, it is pertinent to perform analysis which elucidate the LFO modes in the network, and the mechanism to effectively suppress them.

2.3.1 Small-signal analysis of Low-Frequency Oscillations

LFOs can be studied via small-signal analysis and large-signal analysis [3], [32]. Large signal analysis of LFOs are generally achieved by time-domain simulation of the test power system in the event of large disturbance (e.g. 3-phase fault, loss of power in-feed) [3]. For the small-signal analysis, two techniques have been adopted in literature [106], [107] :(a) Damping torque analysis (b) Modal analysis.

The damping torque analysis (DTA) is commonly employed to examine the torque contribution of the control loops in the SG, to the damping of LFOs in the power system. As discussed in chapter 1, the electrical torque is composed of the synchronizing torque and the damping torque. The synchronizing torque T_s is in phase with the rotor angle deviation $\Delta\delta$ and is responsible for keeping the SG in synchronism with the rest of the power system. Instability due to lack of synchronizing torque emanates in the form of an aperiodic increase in the rotor angle [3]. The employment of fast-acting and high gain AVRs have virtually eliminated the problems associated with insufficient synchronizing torque; however, these AVRs detrimentally impact the damping torque of the SG [108]. The damping torque T_D is in phase with the rotor speed deviation and is responsible for damping oscillations in the power system. Fig. 2.10 illustrates the torque composition of

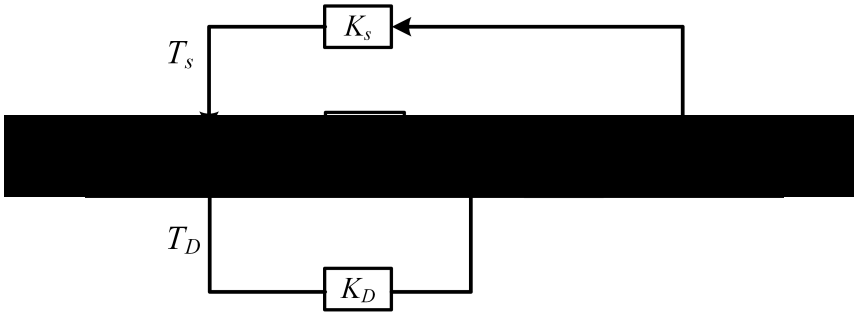

Fig. 2.10. Block representation of a classical generator model connected to an infinite bus [3].

a classical generator connected to an infinite bus. The notations K_s and K_D represent the synchronizing torque coefficient and damping torque coefficient respectively [3]. Stability metrics such as damping torque coefficient index, simple index, damping index, and induced damping and synchronizing torque coefficients can be obtained from the damping torque analysis [106], [109], [110]. Although several works have employed the DTA technique, it is not well-suited for multi-machine analysis [111], [112]. Further, the DTA relies on transfer functions; hence, evaluation based on an arbitrary selection of input and output variables may provide a false conclusion on the system stability [3].

Modal analysis employs state space models to completely describe the dynamics of the power system. The system equations are expressed as a set of first-order, non-linear differential equations, which are then perturbed at a specified operating point to generate the linearized system, which can be represented as (2.30) [106], [107]:

$$\begin{aligned} \boldsymbol{\Delta \dot{x}} &= \boldsymbol{A\Delta x} + \boldsymbol{B\Delta u} \\ \boldsymbol{\Delta y} &= \boldsymbol{C\Delta x} + \boldsymbol{D\Delta u} \end{aligned} \tag{2.30}$$

The notations $\boldsymbol{\Delta} x$, $\boldsymbol{\Delta} y$, $\boldsymbol{\Delta} u$ represent the state, input and output vector respectively, and $\boldsymbol{A}$, $\boldsymbol{B}$, $\boldsymbol{C}$, $\boldsymbol{D}$ represent the state, input, output and feedforward matrix respectively. The stability of the system is described by the eigenvalues of the $\boldsymbol{A}$ matrix [113]. A complex eigenvalue λ can be expressed as $\lambda = \sigma \pm j\omega$; where the imaginary part of the eigenvalue (ω) indicates the oscillation frequency of λ, while the real part of the eigenvalue (σ) is related to the damping of the oscillation. The value of σ determines the system operating

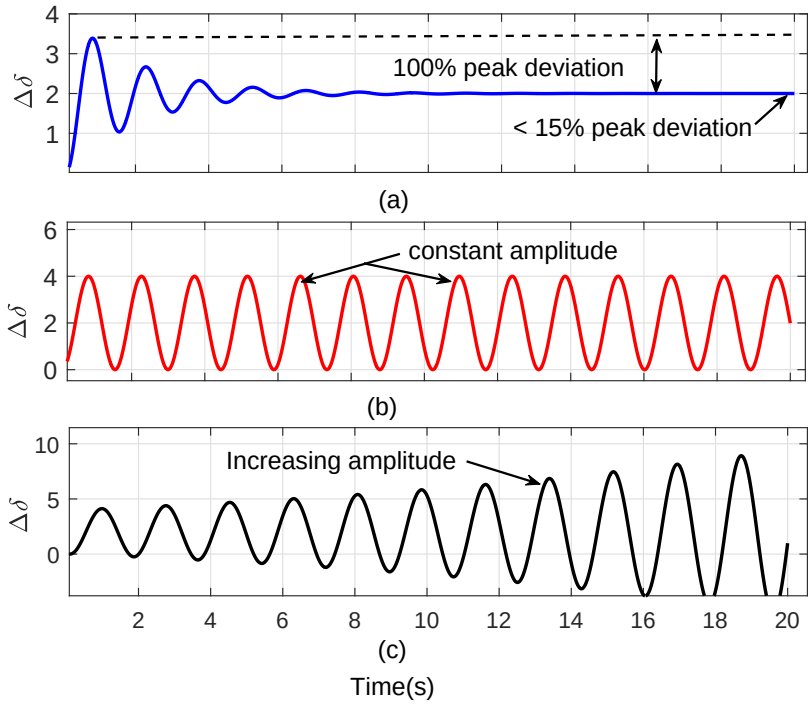

Fig. 2.11. Low-frequency oscillation: (a) stable (b) marginally stable (c) unstable operation.

condition, which can be classified as (a) stable, (b) marginally stable or (c) unstable as illustrated in Fig. 2.11. It is noted that the simulations in Fig. 2.11 were obtained using a state space model of a single machine infinite bus [3]. If all the real parts of the complex eigenvalues in a system are negative, it indicates a system with decaying oscillations and stable operation (see Fig. 2.11(a)). A system which has a complex eigenvalue whose real parts are zero, indicates a marginally stable system whose oscillations do not diminish (see Fig. 2.11(b)). If any real part of the complex eigenvalue is positive, this indicates an unstable system, with increasing oscillations (see Fig. 2.11(c)) [3], [113]. To guarantee system stability in the event of large disturbances, the oscillatory modes must be well-damped. The National Electricity Transmission System Security and Quality of Supply Standard (NETS SQSS) defines poorly damped LFOs as oscillations with resultant peak deviations in excess of 15% of initial amplitude after a 20 second period [114]. Fig. 2.11(a) illustrates the NETS SQSS damping requirement.

By employing control metrics such as participation factor, eigenvalue sensitivity, observability and controllability, control variables causing unstable and poorly damped modes

can be identified and modified to ensure system stability and reliability. A major advantage of the modal analysis over the DTA, is that the state-space representation captures the entire dynamics of the system, and not just the relationship of the input and output variables [3]. Hence, the modal analysis gives a more comprehensive description of the system, and it is ideally suited for the analysis of large power systems [3], [6].

2.4 Techniques for damping Low-Frequency Oscillations

One solution to mitigate the impact of LFOs, is to limit the magnitude of power transfer in critical tie-lines in order to reduce the stress in the system; however, this results in the under-utilization of transmission line infrastructure [115], [116]. The three main techniques proposed in literature for LFO damping are: (1) Load modulation (2) Flexible alternating current transmission systems (FACTS) (3) Power system stabilizers (PSSs). The operating principle of each of the techniques are detailed below.

2.4.1 Load Modulation

The control of large-scale industrial loads and demand-side loads have been widely employed for maintaining the reliability and stability of the power system [117]. Most commonly, peak shaving and load shedding have been employed to ensure cost-effective power system operations, and to prevent cascaded outages or total blackout in the event of severe disturbances [118], [119]. The advent of smart grids, which enables 2-way customer-utility communication, is paving way for selective control of consumer loads without impacting critical loads during contingencies.

The modulation of demand-side load has been proposed in literature as a viable technique for damping LFOs [116], [120]–[122]. The main idea is to remotely control end-user loads in response to LFOs. The loads are grouped into clusters, and wide-area signals are utilized to control each cluster to achieve adequate damping of the LFOs. A typical *modus operandi* is described in [122], where two layers of control termed device layer and supervisory layer are employed. At the device layer, individual loads are equipped with remotely controlled actuators which turn OFF or ON the local loads in response to

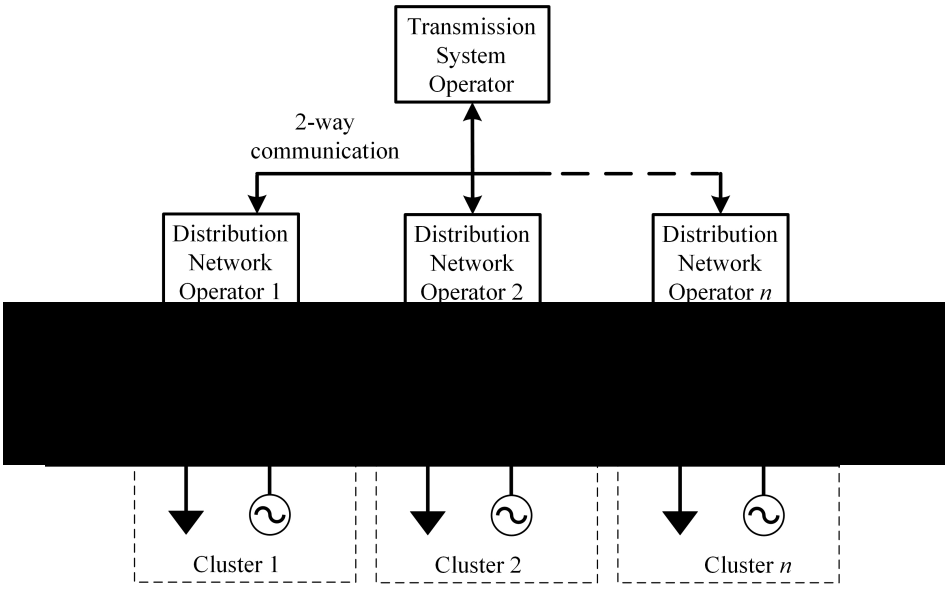

Fig. 2.12. Demand-side load modulation [122].

wide-area signals from a distribution network operator (DNO). At the supervisory layer, loads are segregated into clusters, with each DNO assigned to a cluster by a transmission system operator (TSO). Various system identification techniques can be employed in the assignment of load clusters. In [116], the eigenvalue realization algorithm was employed in the load cluster assignment to achieve effective damping contribution from the end-user loads. The DNO monitors wide-area measurement systems and determines the appropriate wide-area signal to be transmitted to the actuators of the remote load. To ensure that the aggregated load can follow the desired real power modulation, the DNO and TSO periodically reassess the end-user loads available for modulation. Ref [116] suggested modulating the power input to the load by varying the measured voltage (e.g. $\Delta V = \pm 10$ %), rather than switching the load ON/OFF. Damping torque analysis was employed to demonstrate the damping capabilities of variable loads, and a multi-stage mixed H_2/H_∞ approach was employed to design the load damping controllers.

A major drawback of employing load modulation for damping LFOs is the need for significant end-user loads to achieve satisfactory performance, which may not be readily available at the instant of need. Further some loads are very sensitive to voltage and frequency variations and cannot participate in this damping scheme.

2.4.2 FACTS

FACTS refers to a combination of power electronics devices employed to control one or more parameters (e.g. reactive power, voltage) of the power system [106], [113], [123]–[125]. FACTS are commonly employed to facilitate: increased power transmission capacity, improvement of power system transient stability limit, enhanced voltage stability, limiting short circuit currents and smoothen integration of RESs [124], [125]. The studies and implementation of FACTS to improve the stability and reliability of the power system has gained wide attention and application in the both academic and industrial spheres [106], [126]. FACTS can be connected in series with the power transmission line (i.e. series compensation), or in shunt with the power transmission line (i.e. shunt compensation) or a combination of both series and shunt compensation [113], [123], [127]. Fig. 2.13 illustrates the topology of voltage source converter (VSC) based series and shunt connected FACTS. Shunt connected FACTS (see Fig. 2.13(a)) function as controllable current source, and are commonly employed to regulate the reactive power exchange with the grid to maintain the bus voltage within the specified thresholds. Static synchronous compensator (STATCOM) and static var compensator (SVC) are commonly employed FACTS for shunt compensation of the power system. Series connected FACTS (see Fig. 2.13(b)) function as controllable voltage source, which are capable of modulating the reactance of the transmission line or varying the bus voltage [113], [127]. Thyristor controlled series compensator (TCSC) and static synchronous series compensator (SSSC) are commonly employed for series compensation of the power system. The unified power flow controller (UPFC) offers a combination of series and shunt compensation. It is the most versatile FACTS device, and offers more flexibility and control of the power system parameters [106], [126], [128].

In order to improve the damping of LFOs using FACTS, auxiliary stabilizing devices known as power oscillation dampers (PODs) are commonly integrated with FACTs [107], [127], [129]. The PODs damp LFOs by modulating the output variables of the FACTS device. Although several reports have demonstrated that FACTS can be an effective solution for damping LFOs, it may not be economically viable for future energy scenarios with high

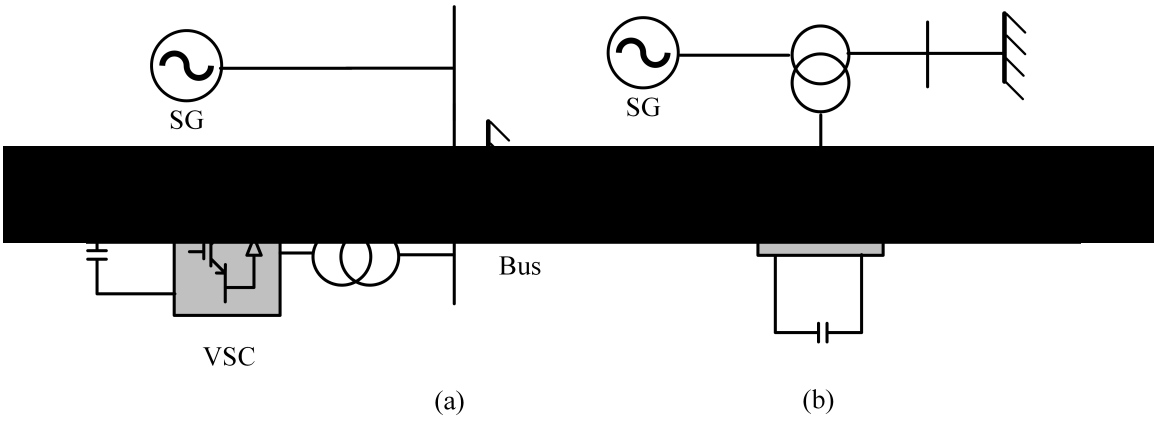

Fig. 2.13. Topology of VSC based FACTS: (a) shunt (b) series connected.

penetration of RESs [106], [122].

2.4.3 Power system stabilizers

Power system stabilizers are the most commonly employed and cost effective solution for damping LFOs [33], [130]. The PSS is commonly employed on the AVR, to inject stabilizing signals which modulates the SGs excitation [3], [125], [131]. The rotor speed, frequency and power are commonly employed as input signals to the PSS [132]–[134]. Fig. 2.14 illustrates the structure of an excitation system with AVR and PSS [3]. The stabilizer gain K_{STAB} determines the amount of damping introduced by the PSS [6]. The phase compensation block, with time constants T_1 and T_2, compensates for the phase lag between the exciter and the SG's electromagnetic torque. The notation n represents the number of cascaded lead-lag filters [107]. The signal washout block serves as a high-pass filter, which eliminates steady state signals from V_{pss}. The time constant of the high-pass filter T_w is selected such that signals in the LFO range pass through the PSS without attenuation. For most applications, T_w is normally chosen in the range of 1–20 s [3]. The terminal voltage E_t is transformed to V via the voltage transducer, with time constant T_R. The error of the voltage summation is amplified by the exciter gain K_A to modulate the exciter's field voltage E_{fd}. It is noted that the configuration of the PSS is same as the POD employed for FACTS devices [130], [134]. With the increasing replacement of SGs with RESs, there are new concerns on the role of PSS on the future grid network and the impact of RES technologies on the LFOs [36], [135], [136].

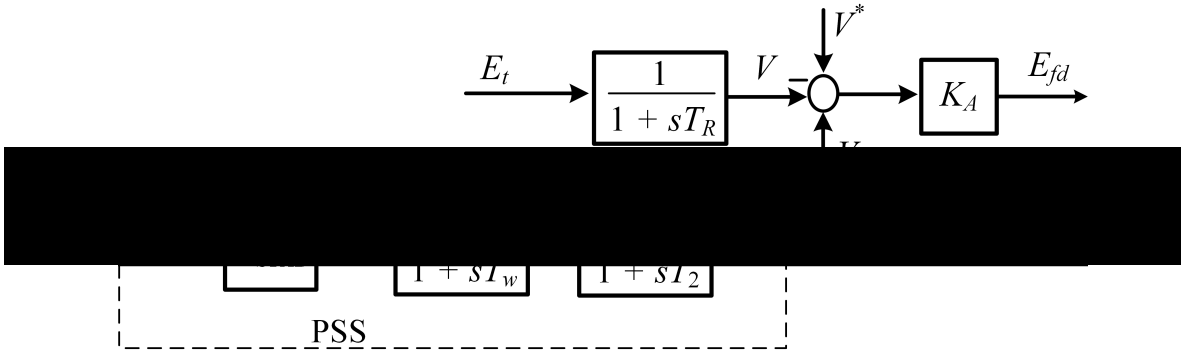

Fig. 2.14. Excitation system with AVR and PSS [3].

2.5 Impact of Renewable Energy Systems on LFOs

The increasing penetration of RESs into the grid significantly impacts the dynamics of the power system [33], [130], [134]. The integration of RESs into the grid have generally been accomplished by two main approaches [36] as illustrated in Fig. 2.15: (1) Addition of RESs into the power system (2) Replacement of SGs with RESs. Considering the two approaches, the replacement of SGs with RESs will have more impact on the power system dynamics. Further, the replacement of SGs with RESs seems more practical in light of the envisioned future energy scenarios [18]. The replacement of SGs with RESs mainly impacts the LFOs in four ways [11], [36], [137]:

1) Replacing the SGs dynamics with the RESs dynamics, thereby affecting the modes (oscillatory and non-oscillatory).

2) Impacting the resultant synchronizing torque in the power system.

3) Displacing SGs integrated with PSS.

4) Large scale RESs impacting damping torque of SGs.

With respect to the synchronizing torques from SGs, fast-acting AVRs have been employed to eliminate problems associated with insufficient synchronizing torques [3], [108]. It is also known that the dynamic response of RESs are much faster than the SGs, hence a well designed RES with voltage/reactive power control is expected to provide adequate synchronizing torque. The remaining three concerns are all related to the damping of the

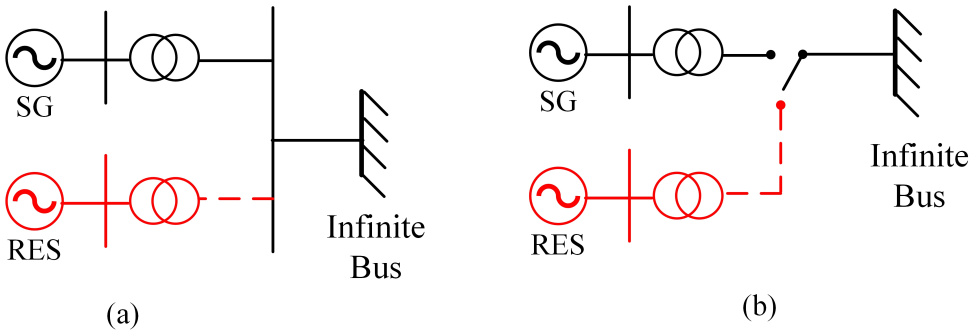

Fig. 2.15. Integration of RES: (a) Addition of RESs (b) Replacement of RESs.

LFOs, which is the focus of the succeeding discussion.

Although, LFOs generally refer to the electromechanical oscillations emanating from SGs, recent literature [99], [138]–[141], have discussed the possibility of new modes in the LFO range due to the interaction between SGs and RESs. Considering the critical nature of LFOs in impacting the power system stability and the gradual replacement of SGs by RESs, the threat of LFO instability will still exist. It is also noted that a "zero carbon power system" does not necessarily mean that there will not be any SGs. For examples, nuclear/hydro power plants, which are considered clean energy, utilize SGs. Hence in this thesis, the oscillations in the LFO range emanating from both the RESs and SGs are termed as LFOs. Generally, two approaches have been employed in improving LFOs with RES: (1) mitigating the impact of RESs on power system LFOs e.g. [142]–[145] (2) employing stabilizing signals on RESs to damp LFOs e.g. [132], [134], [146], [147].

To mitigate the impact of RESs on LFOs, Ref. [142], proposed a retrofit controller for wind farms using a linear quadratic regulator that depends on partial feedback of states solely from the wind farm. This design ensures that newly added RESs do not destabilize a hitherto stable system. It was also observed in [99], [138], [143], [144], that optimizing the parameters of the phase-locked loop (PLL) reduced the impact of RESs on the damping of LFOs. Studies in [33], [145], [148] demonstrate that implementing voltage or reactive power control on RESs (as opposed to unity power factor control) relieves the reactive power strain on SGs and thus improves LFO damping. However, [140] claims that the interaction between reactive power control of RESs with the SGs can create new LFO modes. Also, changing the PLL's parameters as suggested in [99], [138], [143], [144]

may impact the synchronization and the FRT performance. Moreover, since [142]–[145] emphasis on the mitigation of the detrimental impact of RESs on the power system, their employed parameter optimization, may not adequately damp external disturbances emanating from the SGs. Hence, the bulk of studies on RESs focus on the deployment of PSS and PODs using both local and wide-area signals to effectively damp LFOs [130], [132], [134], [146], [147]. However, the potential frequency instability and inertia reduction associated with the traditional RESs is shifting the focus of new studies to the robust and grid-friendly VSMs [149]. Hence, this thesis investigates the LFO modes which exists when VSMs replace SGs, and the role of PSS in such systems.

Recent studies [136], [150] have shown that LFOs, similar to the conventional SGs, exists for multi-VSM power systems. Ref. [136] observed that when the LFOs from the VSM and the SGs are in close proximity, the power system's angular stability deteriorates. Hence, the authors suggested designing the VSM parameters such that the LFOs from the VSM are not within close proximity of the LFOs from the SGs. Although this approach mitigates the detrimental impact of the VSM on the power system angular stability, it may lead to sub-optimal design and performance of the VSM. Ref. [70] proposed a variable inertia scheme for damping LFOs. The rationale of this scheme was elucidated via the energy function analysis and validated via simulation. It was also reported that VSMs employing this scheme can be deployed as a buffer between the SG and the grid to enhance the system stability. However, the authors did not detail the stable boundaries for the inertia variation. Ref. [151] proposed augmenting the adaptive inertia with an inertia matching scheme. The change of frequency and the time derivative of the frequency change were utilized in deriving a stable threshold for the virtual inertia variation. However, the effectiveness of this scheme was not validated for large disturbances. In [152], the VSM swing equation was linearized and expressed as a second-order control system. Hence, the system parameters relating to the damping ratio can be optimized to improve the system stability. Results from the simulated scenarios prove that the proposed scheme is viable for damping LFOs. However, the design requires some trial and error procedures followed by complex and time consuming mathematical derivation. Although the above schemes for VSM do not employ an additional stabilizing signal, the damping provided by [70],

[136], [151] are not as efficient as the conventional PSS.

Ref. [150] proposed a lead-lag compensator employed on the frequency control loop, which provides both inertial and damping effect on the LFOs. Although the proposed control seems effective, the impact of the VSM replacing SG was not investigated. Ref. [149] employed the DTA to evaluate the controllers which impact the LFO damping when VSMs replace SGs. The resulting analysis, illustrated that the PLL significantly impacts the LFO damping of the VSM. Hence, the authors proposed employing a lead-lag compensator which is cascaded with the PLL to improve the LFO damping of the VSM. However, the design of the proposed controller necessitates a trade-off between the tracking speed of the PLL and the damping capability of the VSM, thus hindering the optimal damping of LFOs.

Ref. [153] investigated two LFO damping topologies namely: the grid-damping and self-damping, which employed the measured grid frequency and the virtual rotor speed of the VSM respectively. It was observed that the grid-damping is a more effective solution. Furthermore, the combination of both damping topologies provided satisfactory performance. Similarly, in [154], the difference between the measured grid frequency and the virtual rotor speed was synthesized to achieve a virtual inertial power to damp LFOs. However, the stabilizing signals for these topologies [153], [154] were injected on the active power loop, which may lead to torsional oscillations when the prime mover of the VSM is a wind turbine [133]. In [155], a virtual frictional component was proposed to damp LFOs. The input signal to the virtual frictional component is the difference in rotor speeds of the participating machines. Despite the efficacy of the proposed technique, it is highly reliant on the communication of remote signals (rotor speeds of remote machines), which institutes a technical and economical barrier for application in large systems [156].

In most of the previous arts (including [130], [140], [150]), the grid network is assumed to be quasi-static, which is often considered adequate for stability analysis involving only SGs with slow dynamics [3], [6]. However, for RESs with fast response, evaluating the dynamic interaction of the RESs with the network is crucial in validating the system stability [157], [158]. Also, in [70], [150], [152], [153] the analytical derivations do not provide a holistic insight of the system stability as it neglects some controller dynamics (e.g.

reactive power, voltage and current control). Also, although the generic models employed in [140], [148] are considered adequate for regional planning studies; RES topologies are continually evolving, hence, it is generally agreed that manufacturer-specific models are most appropriate for RESs integration studies [159]. It is also noted, that despite the vast works on RESs, there are still conflicting conclusions on its net impact on the LFO damping [36]. Furthermore, none of the previous arts (to the best of the authors knowledge) have evaluated the role of PSS in an all VSM system.

Hence, in this thesis, the impact of VSMs on LFOs will be extensively investigated. Instead of the generic RESs models and quasi-static network models employed in [140], [148]; a detailed state space model of the SG, VSM and network dynamics was developed in MATLAB/SIMULINK. The systematic design procedure and resulting analysis will be comprehensively discussed in chapter 4. The role of the PSS in an all-VSM grid will also be comprehensively studied. Furthermore, the accuracy of the small-signal analysis will be validated by transient analysis (time-domain simulation).

2.6 Conclusion of Chapter 2

This chapter reviews and discusses the following points:

- The integration of RESs into the grid can significantly impact the grid stability; hence, VSMs have been proposed as a grid-friendly approach for maintaining the grid stability with increasing penetration of RESs.
- Although several VSM topologies have been proposed in literature; the VSMs employing detailed model of SGs are prone to numerical instability and difficult to implement, while some of the simpler models are not well suited for islanded operation. Moreover, most of the topologies proposed in literature will require further modifications before integration with the grid.
- A new VSM paradigm which is capable of operating seamlessly in islanded and grid-connected modes is thus required. The VSM should have inherent over-current protection and must be systematically designed to ensure stable operation. Hence, a

novel VSM algorithm which bridges the gaps highlighted in the previous topologies has been proposed in this thesis, and will be comprehensively discussed and analyzed in chapter 3.

- LFOs inherent in power systems will be impacted by the increasing RESs penetration. VSMs have been deployed to surpress LFOs by modifying the VSM parameters or injecting stabilizing signals using a compensator. The VSMs employing stabilizing signals offer superior damping performance.

- Most of the previous analysis on the impact of RESs on LFOs neglect some control dynamics and network dynamics, thus leading to conflicting conclusions from various researchers. Hence, a fully dynamic and accurate model of the VSM, SG and network parameters will be developed and extensively analyzed in chapter 4.

3. STABILITY ANALYSIS OF A PMSG BASED VIRTUAL SYNCHRONOUS MACHINE

3.1 Introduction

This chapter presents a novel VSM strategy for PMSG based wind turbines which enables seamless operation in all operating modes. This VSM has inherent over-current capability, and can provide black-start service. It guarantees MPPT in grid-connected operation (assuming strong grid), LFPG in islanded operation and FRT capability during faults. To achieve optimal performance in all operating modes, the stability of the VSM will be investigated in the event of small and large perturbations. The small-signal stability analysis of the VSM will be conducted using a linearized state space model, and the impact of the controllers on the dominant modes will be evaluated using participation factor analysis. The transient stability and dynamic performance of the VSM will be analyzed using a non-linear model. Based on this analysis, design guidelines and operational limits of the VSM will be established. The results of this analysis will be validated using time-domain simulations in MATLAB/SIMULINK.

It should be noted that the results presented in this chapter have been published in the Electric Power Systems Research Journal [160].

3.2 Problem Definition

As discussed in chapter 2, most of the VSM topologies proposed in literature do not guarantee seamless transition between grid and islanded modes, thus they require further modifications, to facilitate the smooth integration of RESs into the grid. Some VSM topologies (e.g. VSM0H) employ voltage mode control; hence, they have no inherent over-current protection. Also, some VSM topologies employ complex algorithms (e.g. VISMA,

synchronverter), which are computationally intensive, difficult to implement in real-time, and susceptible to numerical instability. Although the simpler models are likely to provide better stability, some of the simpler models (e.g. VSYNC) are not well adapted for islanded operation.

Further, in some of the previous works (e.g. Algebraic VSM, VSM0H), the stability analysis and required guidelines for designing and tuning the controllers have not been discussed. From an ESOs point of view, this information is crucial, as improper tuning of controllers can lead to oscillatory response and undermine the overall grid stability [21], [157]. Also, some previous arts (e.g. [72] and [75]) omitted the details of the energy source (e.g. wind turbine or solar PV). Therefore, energy management issues such as MPPT in grid-connected mode, and LFPG in islanded mode cannot be investigated.

Hence, in this chapter a novel VSM algorithm, which enables seamless operation in all operating modes has been proposed. The salient features of the VSM strategy proposed in this thesis are:

(1) Seamless transition between grid-connected and islanded mode of operation.

(2) Dynamic voltage and frequency support.

(3) MPPT and LFPG in grid-connected and islanded modes, respectively.

(4) Black-start and FRT capability.

(5) Inherent over-current capability.

(6) Easy application to industrial standard *dq* current control approach.

The base concept of the VSM employed in this thesis was initially developed in [86] (for a PV system), where it was demonstrated that a virtual governor and a virtual AVR can be emulated by a first-order LPF. This chapter proposes a method to adopt the VSM for PMSG based wind systems.

This work is mainly concentrated on the stability analysis of the proposed VSM, although it is noted that ESSs are essential to support the operation of RESs, in order to

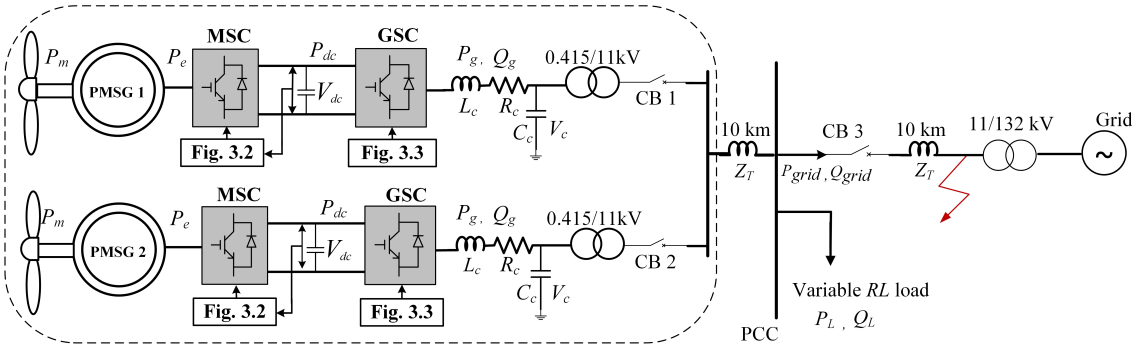

Fig. 3.1. Topology of the understudy system

avoid mixing this work with an EMS, the following assumptions are made:

(1) The combined turbine and generator inertia is sufficient to damp network disturbances. However, the system can be augmented with an external energy storage (to provide extra support), which is not considered in this chapter (for the above reason).

(2) During islanding, load power $P_L \leq$ total available wind power, and load reactive power $Q_L \leq$ available capacity.

(3) The power factor (PF) of the load is maintained at 0.9 lagging PF all through this chapter. The succeeding sections in this chapter are organized as follows: A comprehensive description of the proposed control structure and small-signal model is presented in Section 3.3. The eigenvalue analysis and transient performance are discussed in section 3.4. Section 3.5 presents the simulation results which corroborate the analysis in section 3.4. Section 3.6 concludes the findings of this chapter.

3.3 Modelling of PMSG

The proposed VSM will be explained for PMSG based wind turbines, however, it is applicable to other RESs. The modelling of the wind turbine is described in (A.5)-(A.7). The topology of the understudy system is illustrated in Fig. 3.1.

3.3.1 Machine Side Converter

The machine side converter (MSC) regulates the electrical power P_e that the PMSG extracts from the wind turbine. The PMSG is controlled in the dq frame with the $d-$axis

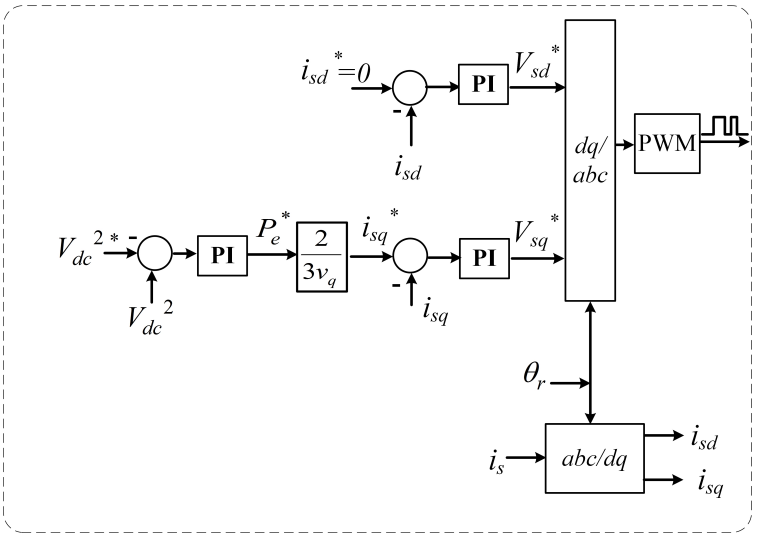

Fig. 3.2. Control structure of the Machine Side Converter

aligned with the rotor magnetic flux λ_m [66], [161]. The control structure of the MSC is illustrated in Fig. 3.2. The dynamics of the PMSG in the rotor field coordinates is given below (3.1−3.4):

$$V_{sd} = L_d \frac{di_{sd}}{dt} + R_s i_{sd} - L_q \omega_r i_{sq} \tag{3.1}$$

$$V_{sq} = L_q \frac{di_{sq}}{dt} + R_s i_{sq} + L_d \omega_r i_{sd} + \lambda_m \omega_r \tag{3.2}$$

$$J \frac{d\omega_r}{dt} = T_m - T_e - B\omega_r \tag{3.3}$$

$$\frac{d\theta_r}{dt} = \omega_r \tag{3.4}$$

Where V_{sd}, V_{sq}, i_{sd}, i_{sq}, L_d, L_q represents the dq component of the stator terminal voltages, current, and self-inductances respectively. R_s, T_m, T_e, J, B, ω_r and θ_r represents the stator resistance, mechanical torque, electromagnetic torque, machine inertia, friction coefficient, rotor speed and rotor angle respectively. For non-salient surface mounted PMSG ($L_q = L_d$), the components of T_e are represented by (3.5), while P_e is given by (3.6) [66], [161]:

$$T_e = \frac{3}{2} \lambda_m i_{sq} \tag{3.5}$$

$$P_e = \frac{3}{2} V_{sq} i_{sq} \tag{3.6}$$

Conventionally, the MSC is employed to extract the maximum power from the wind, and the grid side converter (GSC) transfers the energy to the grid by keeping the DC-link voltage V_{dc} constant. However, it is well-known that extracting the maximum power from

the wind, irrespective of the grid condition, can lead to instability [162], [163]. For example, during faults, where the power output of the GSC is attenuated, the excess P_e leads to rapid rise in V_{dc} and eventual loss of stability [162]. In order to take the grid condition into account, the proposed VSM algorithm in (Fig. 3.3) is employed. Applying the VSM algorithm using the conventional structure (i.e. GSC controls V_{dc}) necessitates separating the virtual AVR (on the GSC) and the virtual governor (on the MSC). Therefore, to keep the virtual AVR and governor on one converter, this thesis proposes to control V_{dc} by the MSC, while the GSC determines the power imposed on the wind turbine P_g. Using the proposed structure (Fig. 3.3), under normal/strong grid condition, since $i_{d-f} \cong 0$, the maximum power will be extracted through the MPPT component i_{d-MPPT}. In the event of abnormal conditions (e.g. a fault on the grid), the virtual governor will regulate the imposed power on the wind turbine (by adding i_{d-f} to i_{d-MPPT}). Since MSC makes $P_e \cong P_g$ (by keeping V_{dc} constant), no supplementary devices will be required to dump the extra energy [163]. The surplus energy from the wind during abnormal conditions will be stored as K.E in the rotor of the wind turbine [162], [163]. Hence, the combination of the wind turbine and associated controls on the MSC, mimics the prime mover of a conventional SG, allowing the contribution of its inertial energy to mitigate system disturbances and suppress oscillations. The relationship between P_e and P_g is governed by the power balance principle (3.7), neglecting losses [66]:

$$P_e - P_g = CV_{dc}\frac{dV_{dc}}{dt} \tag{3.7}$$

Where C represents the DC-link capacitor, V_{dc} is regulated by comparing the reference DC-link voltage ${V_{dc}}^{2*}$ with ${V_{dc}}^2$ (see Fig. 3.2). The error signal is processed by the PI controller to generate Pe^* (where $P_e^* \cong P_e$), which is then transformed to the equivalent current magnitude i_{sq}. The d-component of the current is regulated to zero to maximize available power and minimize ohmic losses [66], [164].

3.3.2 Grid Side Converter

The proposed scheme for the VSM (see Fig. 3.3) is implemented on the GSC, which interfaces with the grid network. It regulates power exchange and ensures stable operation

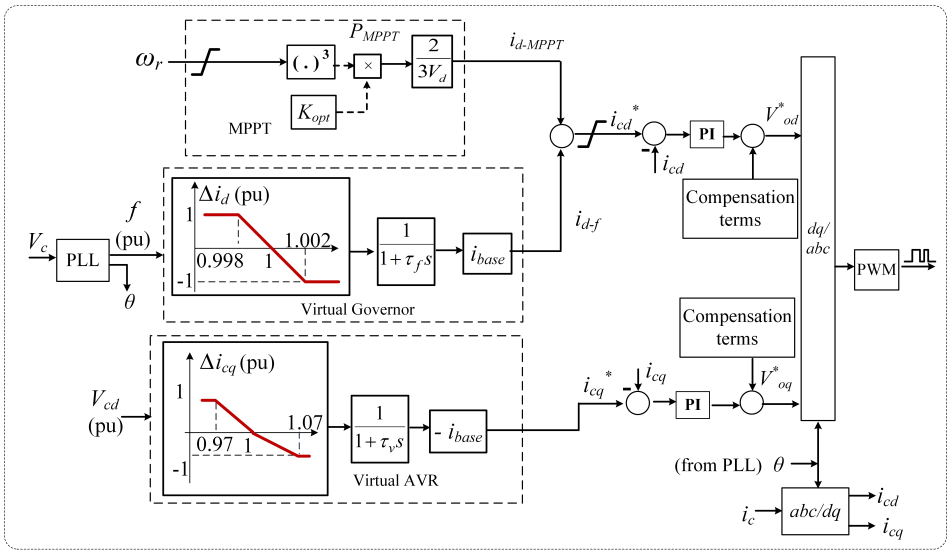

Fig. 3.3. Proposed Control paradigm of the Virtual Synchronous Machine for the Grid Side Converter

of the PMSG and connected loads in all operating modes. The salient feature of this VSM paradigm is that no switching operation is required in all modes of operation. It employs a single control paradigm, which enables MPPT in grid-connected operation (assuming a strong grid), LFPG in islanded mode and FRT during faults. In order to perform the stability analysis, the system can be divided into four sub-systems: power synchronization, power management system (PMS), current controller, the output filter and load. The operation and small-signal model of each sub-systems are detailed below:

3.3.3 Power synchronization

The PLL tracks the phase angle of the filter capacitor voltage V_c (Fig. 3.1) to achieve synchronization with the grid [165], [166]. This ensures the voltage magnitude V is locked with the d - axis, $V_{cd} \approx 1$ pu and $V_{cq} \approx 0$ [167]. In this scheme, the PLL is used in both grid-connected and islanded modes [86]. The PLL dynamics may be neglected for stiff grids, however, it plays a crucial role on the system stability for weak grids and in islanded operation [165], [168]. The synchronously-rotating-frame (SRF) PLL is implemented in this study [86]. The equations representing the PLL dynamics are given by (3.8):

$$\omega = \omega_0 + K_i\, \omega_{PLL} + K_p V_{cq}$$
$$\omega_{PLL} = \int V_{cq}\, dt \;\;, \quad \theta = \int \omega\, dt \tag{3.8}$$

Where ω_{PLL} is the state variable representing $\int V_{cq}\, dt$. The proportional and integral gains are represented by K_p and K_i respectively. The phase angle of the inverter is represented by θ, while ω and ω_0 represent the measured and reference angular frequency respectively. The measured frequency is represented by f. By linearizing, the small-signal model can be written in state space as below:

$$\begin{bmatrix} \Delta\dot{\theta} \\ \Delta\dot{\omega}_{PLL} \end{bmatrix} = A_{PLL} \begin{bmatrix} \Delta\theta \\ \Delta\omega_{PLL} \end{bmatrix} + B_{PLL} \begin{bmatrix} \Delta V_{cq} \end{bmatrix}$$
$$\begin{bmatrix} \Delta\theta \\ \Delta f \end{bmatrix} = C_{PLL} \begin{bmatrix} \Delta\theta \\ \Delta\omega_{PLL} \end{bmatrix} + D_{PLL} \begin{bmatrix} \Delta V_{cq} \end{bmatrix} \tag{3.9}$$

$$A_{PLL} = \begin{bmatrix} 0 & K_i \\ 0 & 0 \end{bmatrix} \;\;, \;\; B_{PLL} = \begin{bmatrix} K_p \\ 1 \end{bmatrix}$$
$$C_{PLL} = \begin{bmatrix} 1 & 0 \\ 0 & \dfrac{K_i}{2\pi} \end{bmatrix} \;\;, \;\; D_{PLL} = \begin{bmatrix} 0 \\ \dfrac{K_p}{2\pi} \end{bmatrix} \tag{3.10}$$

3.3.4 Power Management System

The PMS, regulates the frequency f and voltage V of the system within nominal value. Since large wind farms are normally connected at transmission level, where the network is mainly inductive, the conventional droop control (i.e. $i_d - f$, $i_q - V$) is employed in this thesis. The main components of the PMS include: virtual AVR, virtual governor and the MPPT. The control structure of the PMS is illustrated in Fig. 3.3.

i) Virtual AVR: The primary function of the virtual AVR is to regulate V. In grid-connected operation V is maintained by the grid ($V_{cd} \approx 1$pu). However, in islanded mode of operation, V_{cd} is regulated in proportion to the current demand i_{cq} (which is associated to reactive load Q_L) as illustrated in Fig. 3.3 and described in 4.1, where V_{cd}^* is the reference voltage, i_{cq}^* is the reference reactive current, while K_v and τ_v are the droop gains and damping filter time constant respectively.

$$i_{cq}^* = -K_v(V_{cd}^* - V_{cd})(\frac{1}{1+\tau_v s}) \tag{3.11}$$

ii) Virtual Governor and MPPT: The role of the virtual governor in this scheme, is to regulate f within the nominal value. In grid-connected mode, f is dictated by the grid network. In islanded operation, f is regulated in proportion to the current demand i_d (which is associated to active load P_L). Fig. 3.3 illustrates the i_d – f droop, explained in (3.12) [86]. It is known that $P_{MPPT} = K_{opt}\omega_r^3$, where K_{opt} is a constant denoting the optimal ratio required between ω_r and P_e to achieve MPPT. The integration of the virtual governor and the MPPT loops ensures that maximum power is extracted when connected to a stiff grid, and in islanding it follows the load demand without the immediate need of pitch control. Obviously, if P_L is very small and wind speed is very high, ω_r may exceed the rated speed (normally 1.2 pu), which necessitates using the pitch angle. The equation representing the dynamics of the virtual governor and MPPT is given by (3.12):

$$i_{cd}^* = K_f(f^* - f)(\frac{1}{1+\tau_f s}) + i_{d-MPPT} \tag{3.12}$$

Where f^*, i_{cd}^* and i_{d-MPPT} are the reference frequency, reference active current and output current of the MPPT respectively. K_f and τ_f are the droop gains and the damping filter time constant of the virtual governor respectively. Assuming i_{d-MPPT} is constant ($di_{d-MPPT}/dt = 0$), the small-signal linearized model of the PMS is given

by (3.13) and (3.14):

$$\begin{bmatrix} \Delta\dot{i}^*_{cq} \\ \Delta\dot{i}^*_{cd} \end{bmatrix} = A_{PMS} \begin{bmatrix} \Delta i^*_{cq} \\ \Delta i^*_{cd} \end{bmatrix} + \begin{bmatrix} B_{PMS_v} \\ B_{PMS_f} \end{bmatrix} \begin{bmatrix} \Delta V^*_{cd} \\ \Delta f^* \end{bmatrix} + \begin{bmatrix} B_{PMS_v} \\ B_{PMS_f} \end{bmatrix} \begin{bmatrix} -\Delta V_{cd} \\ -\Delta f \end{bmatrix} \tag{3.13}$$

$$\begin{bmatrix} \Delta i^*_{cq} \\ \Delta i^*_{cd} \end{bmatrix} = C_{PMS} \begin{bmatrix} \Delta i^*_{cq} \\ \Delta i^*_{cd} \end{bmatrix} \tag{3.14}$$

$$A_{PMS} = \begin{bmatrix} \frac{-1}{\tau_v} & 0 \\ 0 & \frac{-1}{\tau_f} \end{bmatrix}, \quad B_{PMS_v} = \begin{bmatrix} \frac{-K_v}{\tau_v} & 0 \end{bmatrix}$$
$$B_{PMS_f} = \begin{bmatrix} 0 & \frac{K_f}{\tau_f} \end{bmatrix}, \quad C_{PMS} = \begin{bmatrix} 1 & 0 \\ 0 & 1 \end{bmatrix} \tag{3.15}$$

3.3.5 Current Controller

The output of the PMS is fed directly to the current controllers as shown in Fig. 3.3. The current controller shapes the voltage across the filter inductor and dampens oscillations at the output of the LC filters [169], [170]. The equations representing the current controller are given below:

$$\text{Let } \gamma_d = \int i^*_{cd} - i_{cd}, \quad \gamma_q = \int i^*_{cq} - i_{cq} \tag{3.16}$$

$$V^*_{od} = -\omega_0 L_c i_{cq} + K_{pc}(i^*_{cd} - i_{cd}) + K_{ic}\gamma_d \tag{3.17}$$

$$V^*_{oq} = \omega_0 L_c i_{cd} + K_{pc}(i^*_{cq} - i_{cq}) + K_{ic}\gamma_d \tag{3.18}$$

Where γ_d and γ_q are the state variables in the current controller. The proportional and integral gains are represented by K_{pc} and K_{ic} respectively. L_c is the filter

inductance, while V_{od}^* and V_{oq}^* represents the output voltage of the inverter. The linearized small-signal state space form of the current controller are given below:

$$\begin{bmatrix} \Delta\dot{\gamma}_{dq} \end{bmatrix} = \begin{bmatrix} 0 \end{bmatrix} \begin{bmatrix} \Delta\gamma_{dq} \end{bmatrix} + B_{C1} \begin{bmatrix} \Delta i_{cdq}^* \end{bmatrix} + B_{C2} \begin{bmatrix} \Delta i_{cdq} \\ \Delta V_{cdq} \\ \Delta i_{ldq} \end{bmatrix} \tag{3.19}$$

where $\Delta\gamma_{dq} = [\Delta\gamma_d \;\; \Delta\gamma_q]^T$

$$B_{C1} = \begin{bmatrix} 1 & 0 \\ 0 & 1 \end{bmatrix} \;, \;\; B_{C2} = \begin{bmatrix} -1 & 0 & 0 & 0 & 0 & 0 \\ 0 & -1 & 0 & 0 & 0 & 0 \end{bmatrix} \tag{3.20}$$

$$\begin{bmatrix} V_{odq}^* \end{bmatrix} = C_c \begin{bmatrix} \Delta\gamma_{dq} \end{bmatrix} + D_{c1} \begin{bmatrix} \Delta i_{cdq}^* \end{bmatrix} + D_{c2} \begin{bmatrix} \Delta i_{cdq} \\ \Delta V_{cdq} \\ \Delta i_{ldq} \end{bmatrix} \tag{3.21}$$

$$C_c \begin{bmatrix} K_{ic} & 0 \\ 0 & K_{ic} \end{bmatrix} \;, \; D_{c1} = \begin{bmatrix} K_{pc} & 0 \\ 0 & K_{pc} \end{bmatrix} \tag{3.22}$$

$$D_{c2} = \begin{bmatrix} -K_{pc} & -\omega_0 L_f & 0 & 0 & 0 & 0 \\ \omega_0 L_f & -K_{pc} & 0 & 0 & 0 & 0 \end{bmatrix} \tag{3.23}$$

3.3.6 Output LC filter and load

The output current i_{cd} and i_{cq} from the inverter is fed to the load and grid through the output filters R_c, L_c and C_c of the inverter and coupling inductance. In the small-signal model, the coupling inductance are superimposed with the variable load (R_l and L_l in Fig. 3.1). It is also assumed that the inverter delivers the required output voltage, i.e., $V_{odq}^* = V_{odq}$. The state equation of the output LC filter and the load

are represented below:

$$\frac{di_{cd}}{dt} = \frac{-R_c}{L_c} i_{cd} + \omega i_{cq} + \frac{1}{L_c} V_{od} - \frac{1}{L_c} V_{cd} \tag{3.24}$$

$$\frac{di_{cq}}{dt} = \frac{-R_c}{L_c} i_{cq} - \omega i_{cd} + \frac{1}{L_c} V_{oq} - \frac{1}{L_c} V_{cq} \tag{3.25}$$

$$\frac{dv_{cd}}{dt} = \omega V_{cq} + \frac{1}{C_c} i_{cd} - \frac{1}{C_c} i_{ld} \tag{3.26}$$

$$\frac{dv_{cq}}{dt} = -\omega V_{cd} + \frac{1}{C_c} i_{cq} - \frac{1}{C_c} i_{lq} \tag{3.27}$$

$$\frac{di_{ld}}{dt} = \frac{-R_l}{L_l} i_{ld} + \omega i_{lq} + \frac{1}{L_l} V_{cd} \tag{3.28}$$

$$\frac{di_{lq}}{dt} = \frac{-R_l}{L_l} i_{lq} - \omega i_{ld} + \frac{1}{L_l} V_{cq} \tag{3.29}$$

The linearized small-signal state space form of the LC filter and load is given by:

$$A_{LCL} = \begin{bmatrix} \frac{-R_c}{L_c} & \omega_0 & \frac{-1}{L_c} & 0 & 0 & 0 \\ -\omega_0 & \frac{-R_c}{L_c} & 0 & \frac{-1}{L_c} & 0 & 0 \\ \frac{1}{C_c} & 0 & 0 & \omega_0 & \frac{-1}{C_c} & 0 \\ 0 & \frac{1}{C_c} & -\omega_0 & 0 & 0 & \frac{-1}{C_c} \\ 0 & 0 & \frac{1}{L_l} & 0 & \frac{-R_l}{L_l} & \omega_0 \\ 0 & 0 & 0 & \frac{1}{L_l} & -\omega_0 & \frac{-R_l}{L_l} \end{bmatrix} \tag{3.30}$$

$$B_{LCL1} = \begin{bmatrix} \frac{1}{L_l} & 0 & 0 & 0 & 0 & 0 \\ 0 & \frac{1}{L_l} & 0 & 0 & 0 & 0 \end{bmatrix}^T \tag{3.31}$$

$$B_{LCL2} = \begin{bmatrix} i_{cq} & -i_{cd} & V_{cq} & -V_{cd} & i_{lq} & -i_{ld} \end{bmatrix}^T \tag{3.32}$$

$$\begin{bmatrix} \Delta\dot{i}_{cdq} \\ \Delta\dot{V}_{cdq} \\ \Delta\dot{i}_{ldq} \end{bmatrix} = A_{LCL} \begin{bmatrix} \Delta i_{cdq} \\ \Delta V_{cdq} \\ \Delta i_{ldq} \end{bmatrix} + B_{LCL1} \begin{bmatrix} \Delta V_{odq} \end{bmatrix} + B_{LCL2} \begin{bmatrix} \Delta\omega \end{bmatrix} \tag{3.33}$$

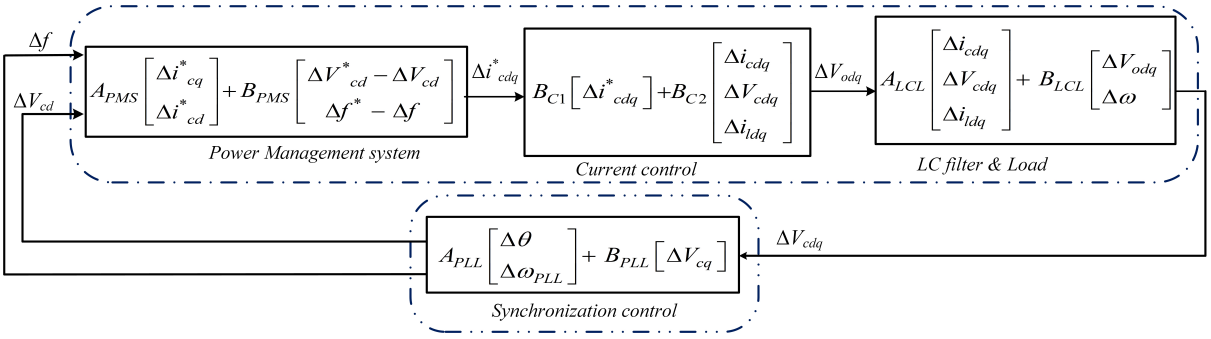

Fig. 3.4. Linearized model of the proposed VSM

The overall linearized model of the system is illustrated in Fig. 3.4. The aggregated matrix (3.34), is derived by combining the state space models of the power synchronization sub-system (3.9), PMS (3.13), (3.14), current controller (3.19), (3.21), the output filter and load (3.33).

$$\Delta\dot{x} = \mathbf{A}[\Delta x] + \mathbf{B}[\Delta u]$$

$$\Delta x = \begin{bmatrix} \Delta\theta & \Delta\omega_{PLL} & \Delta i^*_{cdq} & \Delta\gamma_{odq} & \Delta i_{cdq} & \Delta V_{cdq} & \Delta i_{ldq} \end{bmatrix}^T$$

$$\mathbf{A} = \begin{bmatrix} A_{PLL} & 0 & 0 & B_{PLL} \\ B_{PMS_f} C_{PLL} & A_{PMS} & 0 & \begin{bmatrix} B_{PMS_v} \\ B_{PMS_f} D_{PLL} \end{bmatrix} \\ 0 & B_{c1} & 0 & B_{c2} \\ B_{LCL2}(k_i) & B_{LCL1} D_{c1} & B_{LCL1} C_c & A_{LCL} + B_{LCL1} D_{c2} \\ & & & +B_{LCL2}(k_p) \end{bmatrix}_{12\times 12}$$

$$\mathbf{B} = \begin{bmatrix} 0 & B_{PMS_v} & 0 & 0 \\ 0 & B_{PMS_f} & 0 & 0 \end{bmatrix}_{2\times 12}, \quad \Delta u = \begin{bmatrix} \Delta V^*_{cd} & \Delta f^* \end{bmatrix} \tag{3.34}$$

Tab. 3.1. System's Parameters

MSC		
Variable	PMSG 1	PMSG 2
Rated Power	2 MW	1 MW
Rated Voltage	0.7 kV	0.7 kV
Rated Rotor speed	3.1 rad/s	4.4 rad/s
Inertia Time constant	3 s	2 s
DC link Voltage	2 kV	2 kV
DC link Capacitance	6 mF	4.5 mF
VSM (GSC)		
Transmission line impedance Z_T	$R = 0.16$ mΩ/km	$L = 0.1$ mH/km
Current loop PI controllers	$K_{pc} = 0.15$	$K_{ic} = 1.5$
PMS damping	$\tau_f = 1.3$ s	$\tau_v = 0.005$ s
PLL (PMSG 1/ PMSG 2)	$K_p = 0.05/\ 0.03$	$K_i = 0.5/\ 0.03$
Filter impedance	$R_c = 1.5$ mΩ	$L_c = 0.15$ mH $\quad C_c = 160\ \mu$F

3.4 Stability Analysis and Dynamic Peformance of the Proposed VSM

The stability of the proposed VSM, will be analyzed for both small and large perturbations. In this section, the MSC is replaced by a constant DC source in order to focus on the VSM dynamics.

3.4.1 Validation of small-signal model

For the purpose of validating the developed small-signal (mathematical) model (Fig. 3.4), the response of the model is compared with the SIMULINK model (i.e. developed using components from the MATLAB specialized power systems toolbox). The system parameters, detailed in Table 3.1 for PMSG 1, are used for both SIMULINK and small-signal models.

Fig. 3.5 shows the system response of both models for a step change in load. The variables P, Q, V and f respectively represent the active power, reactive power,

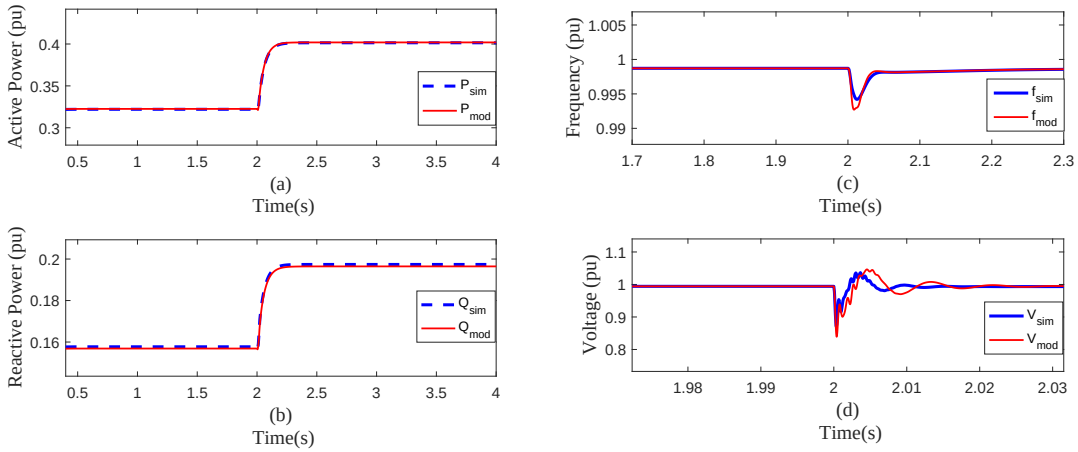

Fig. 3.5. Simulation results comparing the response of the SIMULINK model with the small-signal model:(a) Active Power (b) Reactive Power (c) Frequency (d) Voltage

voltage and frequency. The signals from the SIMULINK and small-signal model are identified by the suffix "sim" and "mod" respectively. From Fig. 3.5(a) and Fig. 3.5(c), it is observed that for an increase in active power demand from 0.32 pu to 0.4 pu, P_{mod} closely matches P_{sim}, while f_{mod} also matches f_{sim} but with a slightly larger undershoot than f_{sim}. Similarly, for an increase in reactive power demand from 0.16 pu to 0.2 pu, Fig. 3.5(b) and Fig. 3.5(d) show that, Q_{mod} closely matches Q_{sim}, while V_{mod} also matches V_{sim} but with slightly more oscillations. The results from Fig. 3.5 confirm that the developed model accurately represents the VSM. The increased oscillations observed on the small-signal model is due to the linearity of the system.

3.4.2 Eigenvalue analysis

The steady state initial condition for this analysis, is a single VSM (PMSG 1) feeding an RL load of 0.70 pu. The system parameters are given in Table 3.1. The complete state space matrix of the VSM has 12 states (3.34). As observed in Table 3.2, all eigenvalues have negative real parts, indicating stable operation.

Tab. 3.2. Complete System eigenvalues

Eigenvalues			Damping	f (Hz)	Dominant
λ	Real	Imaginary	ratio (ζ)		states
λ_1	0		1		$\Delta\theta$
$\lambda_{2,3}$	-407	± 9910i	0.04	1577	Δi_{cdq}, ΔV_{cdq}, Δi_{ldq}
λ_4	-948		1		Δi_{cd}, Δi_{ldq}
$\lambda_{5,6}$	-441	± 8120i	0.05	1292	Δi_{cdq}, ΔV_{cdq}, Δi_{ldq}
$\lambda_{7,8}$	-410	± 1010i	0.38	161	Δi^*_{cq}, Δi_{cq}, Δi_{lq}
λ_9	-40.1		1		Δi^*_{cd}
λ_{10}	-15.2		1		$\Delta\omega_{PLL}$, Δi^*_{cd} , $\Delta\gamma_{dq}$
$\lambda_{11,12}$	-9.39	± 1.01i	0.99	0.16	$\Delta\omega_{PLL}$, $\Delta\gamma_q$

The dominant states, which are shown in Table. 3.2, are derived using the participation factor matrix [3].

It can be inferred that there is a degree of coupling between the states relating to the active and reactive power control, this is because the system is not purely inductive [157]. The zero eigenvalue λ_1, is due to the PLL angle $\Delta\theta$, a similar occurrence is observed with the rotor angle when SGs are operated in islanded mode [3]. The super-synchronous oscillatory modes $\lambda_{2,3}$ and $\lambda_{5,6}$ are associated with the LC filter and load, and are damped instantaneously (0.003 s). The modes $\lambda_{7,8}$ are mainly influenced by the virtual AVR, which dictates the reactive power flow.

The sub-synchronous oscillatory modes $\lambda_{11,12}$ are associated with states from the PLL and the current controller. The result of the eigenvalue analysis confirms that the VSM is well-damped, as the dominant modes have a damping ratio, $\zeta \geq 5\%$ [171]. The dominant modes of the VSM, which are λ_{10} and $\lambda_{11,12}$, are mainly influenced by the reactive power flow and by states from the PLL and virtual governor. Hence, to maintain stability and achieve the desired dynamic performance of the VSM in all operating modes, the design parameters of the PLL, virtual AVR and virtual governor will be further investigated.

3.4.3 Impact of PLL on VSM stability

The PLL bandwidth has a dominant effect on the stability of the VSM. Although a fast PLL is desirable for grid synchronization, it can greatly reduce stability, increase phase tracking error and lead to poor harmonics filtering [165], [172]. Hence, a compromise is required between a fast synchronizing PLL and an optimal dynamic performance. Fig. 3.6 shows the transition of the open loop poles as the proportional gain K_p of the PLL is increased. As the poles move closer to the origin, the voltage waveforms becomes distorted. It can be observed that for $K_p \geq 3$, the VSM becomes unstable. This corroborates earlier works [165], [168] which stipulate that, for stable operation in islanded operation PLL bandwidth should be small. To ensure stability in the event of fault, where large swings are expected in V_{cq} this work proposes keeping K_p at $\leq 10\%$ of the critical K_p value ($K_p \approxeq 3$).

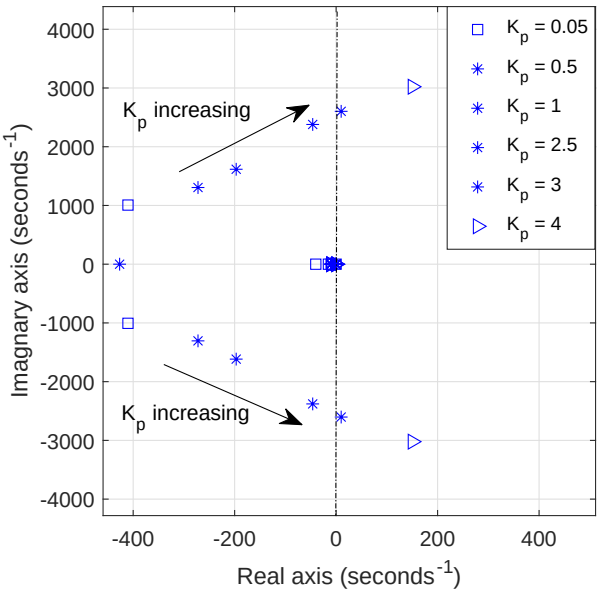

Fig. 3.6. Transition of open loop poles with varying K_p

3.4.4 Impact of Virtual AVR damping

Based on the VSM design Fig. 3.3, the voltage and frequency droop gains are constant (determined by the grid regulation in the region). However, the damping filter

time constants τ_f and τ_v of the virtual governor and virtual AVR can be varied to improve the stability and transient response. Hence, the impact of τ_f and τ_v on the dynamics and transient stability of the VSM will be investigated using eigenvalue analysis and time domain simulation respectively.

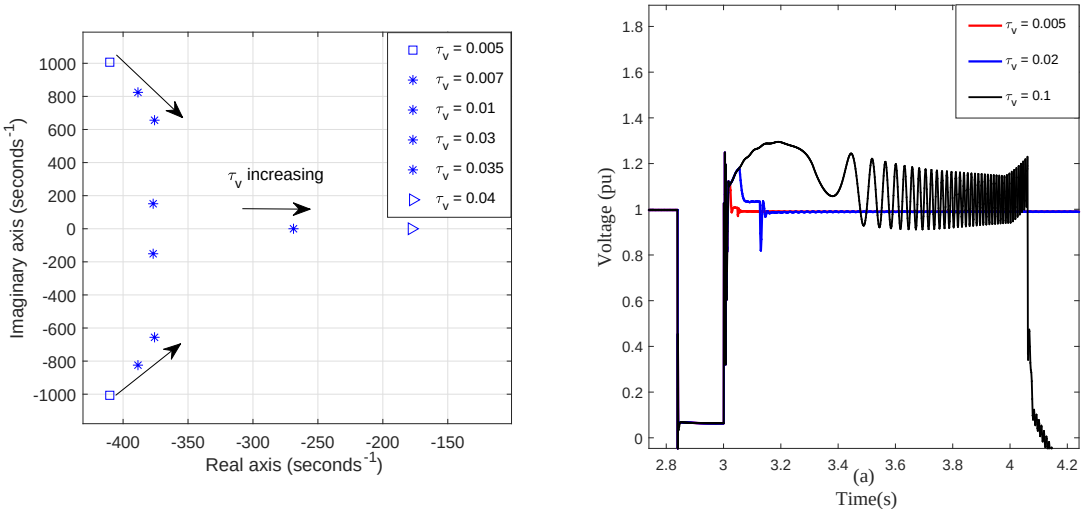

(a) Transition of open loop poles with varying τ_v

(b) Transient performance of VSM for varying values of τ_v

Fig. 3.7. Performance of VSM for different values of τ_v

Fig. 3.7(a) illustrates the transition of the poles as τ_v is varied. It is observed that as τ_v is increased, the open loop poles move towards the $j\omega$-axis indicating a less stable operating mode. For large values of τ_v ($\tau_v > 0.6$) the open loop poles cross over to the right hand plane (RHP) and the system becomes unstable.

Fig. 3.7(b) illustrates the transient performance of the proposed VSM for different values of τ_v (at the same operating point as the linearized model used for the eigenvalue analysis). The VSM is initially grid-connected, then a 3-phase fault is applied on the grid side at 2.86 s, thereafter the VSM is disconnected at 3 s and operates in islanded mode. It can be observed that as the damping on the virtual AVR is increased, which results in a slower response, the transient performance worsens and for $\tau_v = 0.1$ the VSM fails to recover post-fault. The result from the

transient analysis, corroborates the result from the small-signal analysis, which illustrated that increasing τ_v moves the VSM poles towards the unstable operating region (RHP). Hence, this work proposes keeping τ_v at ≤ 0.01. This findings also conforms with the operation of the SG, where high exciter response is required to increase synchronizing torque and improve transient stability [3].

3.4.5 Impact of Virtual Governor damping

The damping filter time constant τ_f of the virtual governor proffers inertial support for the VSM operation. Fig. 3.8 illustrates the transition of the open loop poles as τ_f is varied. It can be observed that the open loop poles drift away from the RHP as τ_f increases, indicating a more stable operation. Furthermore, an increase in τ_f results in damping of higher frequency oscillations in the system.

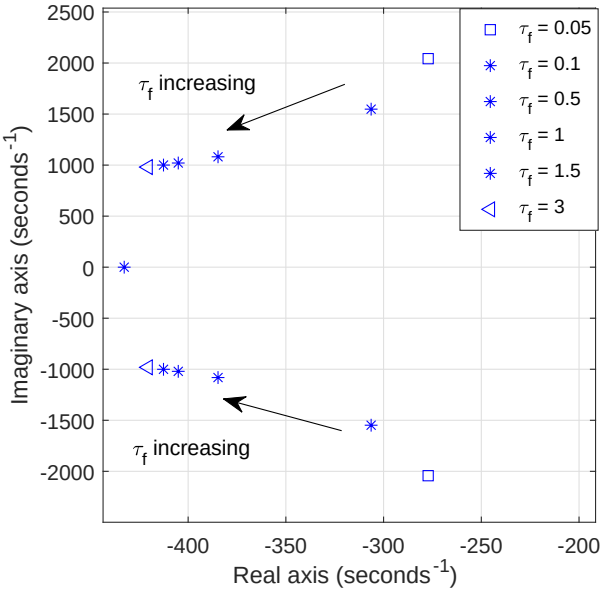

Fig. 3.8. Transition of open loop poles with varying τ_f

To observe the transient stability of the VSM due to τ_f, the same test procedure as for Fig. 3.7 is implemented. From Fig. 3.9, after the fault is cleared, we observe a relatively high frequency oscillation on the voltage signal for $\tau_f = 0.2$, indicating an under-damped system. However for $\tau_f \geq 0.4$, the VSM provides a better damped

response which suppresses the oscillation due to the disturbance and eliminates high frequency oscillation caused by the PLL interaction with the controllers. Despite the benefits of a large inertial support, a very slow system response is also undesirable. Hence, this work proposes keeping τ_f at, $0.4 \leq \tau_f \leq 1.5$. This phenomenon is also similar to the SG, where a large inertia is required to mitigate network disturbances, and sufficient damping of the rotor angle is required to maintain stability after a large disturbance [3].

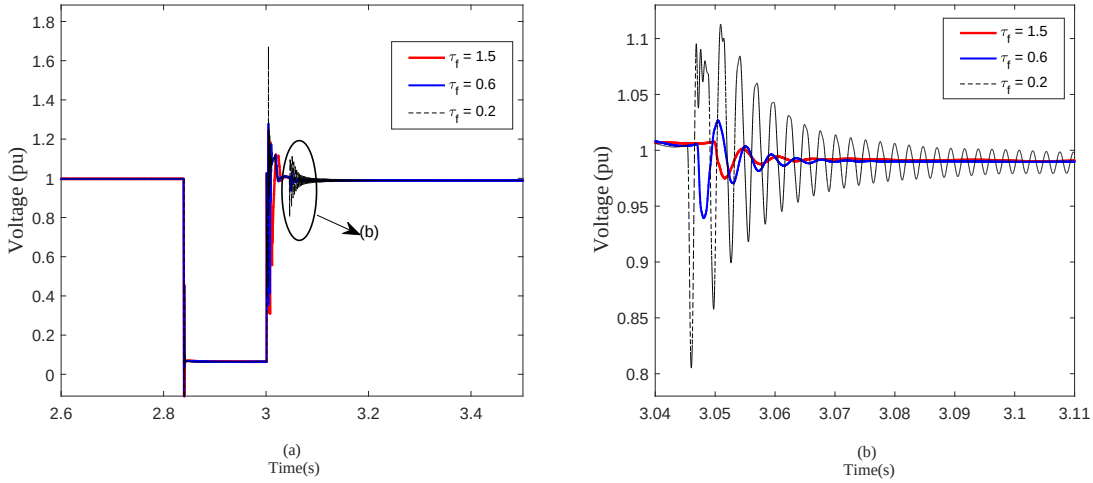

Fig. 3.9. Transient response of the VSM for different values of τ_f

3.5 Simulation and Discussion

The model shown in Fig. 3.1 is simulated using the MATLAB/SIMULINK software package. The system parameters for the PMSGs are given in Table 3.1. All results are presented in pu based on total system rating (not each PMSG). The output of the individual PMSGs are represented as $PMSG1$ and $PMSG2$. P_T, Q_T and P_{grid}, Q_{grid} represent the total active and reactive power from the PMSGs and the grid respectively. ω_{opt} represents the optimal rotor speed based on available wind power, while ω_{r1} and ω_{r2} represents the rotor speed of each PMSG. Figs. 3.10(g) and 3.10(h) illustrate the voltage and frequency at PCC (see Fig. 3.1). Fig. 3.10 illustrates the simulation results of the following scenarios:

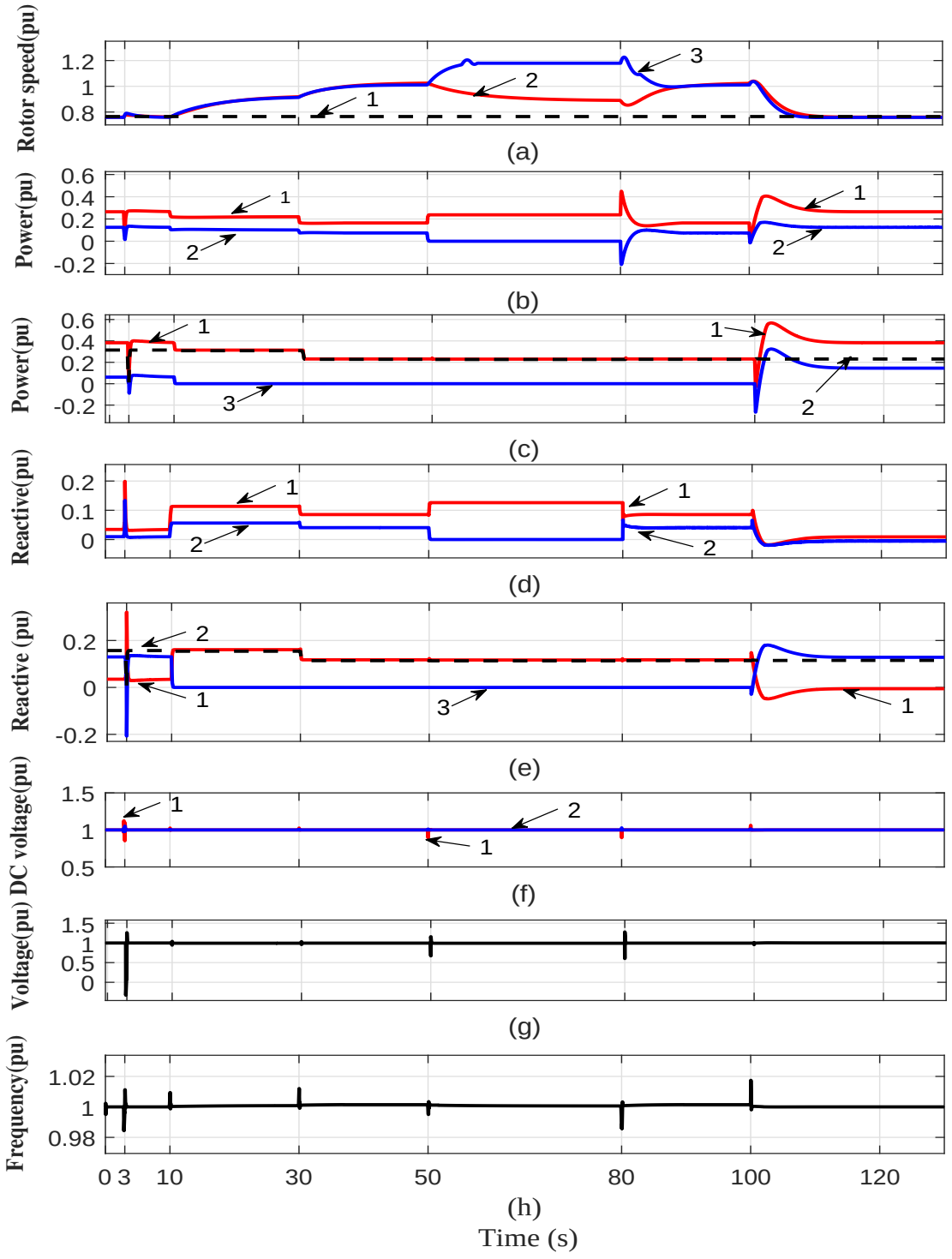

Fig. 3.10. Simulation results for PMSGs in grid-connected and islanded mode:(a) Rotor speed, pu 1- ω_{opt}, 2 - ω_{r1}, 3 - ω_{r2}. (b) Power, pu 1 - $PMSG1$, 2 - $PMSG2$. (c) Power, pu 1 - P_T, 2 - P_L, 3 - P_{grid} (d) Reactive power, 1 - $PMSG1$, 2 - $PMSG2$ (e) Reactive power, pu 1 - Q_T, 2 - Q_L, 3 - Q_{grid} (f) DC-Link voltage (V_{dc}), pu 1 - $PMSG1$, 2 - $PMSG2$ (g) Voltage at PCC, pu (h) Frequency at PCC, pu.

3.5.1 Grid-connected operation (0—10 s)

The simulation starts with the two PMSGs connected to the grid. It can be observed from Fig. 3.10(a) that the PMSGs are operating at MPPT as $\omega_{opt} = \omega_{r1} = \omega_{r2} =$ 0.78 pu. The surplus power (not consumed by P_L) is transferred to P_{grid} (Fig. 3.10(c)). It is also observed (see Figs. 3.10(d) and 3.10(e)) that Q_L is supplied by the grid, which is in compliance with the control paradigm. At t = 2.84 s, a 3-phase fault occurs at the grid side, (see Fig. 3.1). The PMSGs seamlessly ride through the fault, as the DC voltage V_{dc} (Fig. 3.10(f)) and f (Fig. 3.10(h)) are well regulated. It is worth noting that, unlike the conventional control strategies (where V_{dc} is controlled by GSC) [162], V_{dc} does not rise during fault, as the prime mover (MSC) only supplies the power demanded by the VSM. Hence $P_e \approxeq P_g$ during fault, and the surplus energy from the wind during fault is stored as K.E in the rotor (ω_{r1} and ω_{r2} increases). This eliminates the need for a crowbar on the DC-link to dissipate excess energy. As observed from Fig. 3.11, there is minimal distortion on the voltage waveform during fault. The fault is cleared at 3 s, and it is observed that the VSM maintains stable operation; as instability due to large disturbance is usually evident within 2–3 s after the disturbance [3]. At t = 10 s, the VSM is disconnected from the grid. Unlike [75], there is no need to switch controllers when disconnecting the VSM from the grid. As observed from Fig. 3.10, the transition to islanded operation is seamless.

3.5.2 Islanded operation (10–100 s)

In this operating mode, the PMS ensures V and f are regulated within nominal values. Hence, the PMSGs operate in the sub-optimal power region [173], this is reflected by an increase in the rotor speeds, and is determined by the load demand. The following test scenarios are applied in this mode:

(I) A step reduction in load demand occurs at t = 30 s. As illustrated in Figs.

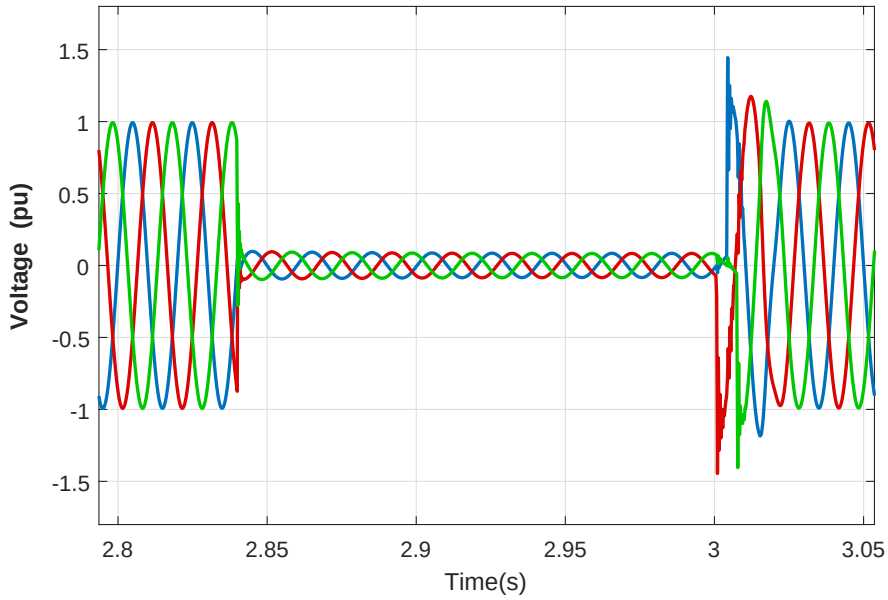

Fig. 3.11. The three-phase voltage waveform at PCC (pu) for the fault duration

3.10(c) and 3.10(e), P_T and Q_T precisely follow the change in load demand P_L and Q_L respectively. As shown in Figs. 3.10(b) and 3.10(d), the load is shared by the two PMSGs while the surplus electrical power in the PMSGs are stored as K.E in the rotor.

(II) The system runs smoothly until t = 50 s, when PMSG 2 is suddenly taken offline (CB 2 is open). This was done to observe the system response to large disturbance. Upon the sudden loss of PMSG 2, PMSG 1 supplies the total load. As observed from Fig. 3.10(a), PMSG 1 releases the stored K.E and operates close to the MPPT region. Since PMSG 2 is operating on no-load, the pitch control is automatically activated to limit ω_{r2} to 1.2 pu. The standard pitch control from MATLAB was implemented here. As observed from Fig. 3.10(g) and 3.10(h), V and f are well regulated and the system maintains stability despite the large disturbance. This shows that, for a system implementing the proposed VSM, if one or more converters develop a fault during operation, it can be easily taken offline with negligible impact on the operation of the remaining VSMs. At t = 80 s, PMSG 2 is reconnected and the load is shared between the two PMSGs.

Fig. 3.10 shows that V and f are maintained within nominal value.

3.5.3 Grid Reconnection (100–130 s)

At t = 100 s, the grid is restored and CB 3 is closed. The transition to the grid is relatively smooth, and V and f are well controlled. As observed from Fig. 3.10, there is negligible voltage oscillation during transition to grid, as the phase difference between the islanded zone and the grid at the time of closing CB 3 is very minute. As earlier discussed, a fast PLL (i.e. PLL with large bandwidth) will be detrimental to the system stability. However, since grid reconnection is always intentional, conventional synchro-check devices [97], [98] can be applied to ensure the VSM variables (V, f, θ) are within the stipulated boundaries [174], prior to closing the mains circuit breaker (which is CB 3 in this study) to ensure smooth transition to the grid-connected operation.

The key contributions of this chapter are:

I) Developed a detailed mathematical model of the proposed VSM.

II) Comprehensive analysis of the VSM in the event of small and large perturbations.

III) Establishing design guidelines using the developed small-signal model.

3.6 Conclusion of Chapter 3

This chapter proposed a VSM strategy for PMSG based wind turbines, which enables seamless operation in grid-connected and islanded operating modes. It achieves MPPT in grid-connected operation, LFPG in islanded operation and FRT during faults.

A detailed mathematical model of the VSM was derived and the dynamic response was validated with the SIMULINK model. The derived model was analyzed

in the event of small and large perturbations. It was observed from the analysis, that a low PLL bandwidth is required for a desirable performance and stable operation of the VSM. It was also observed that, a fast virtual AVR and a relatively slow and well-damped virtual governor are essential to maintain stability and optimal dynamic performance.

The results of this analysis, were used as a guide in the design of the VSM. To verify the performance of the VSM, a time domain simulation (MATLAB/SIMULINK) was performed for different test scenarios. The results confirmed that the VSM operates seamlessly in grid-connected and islanded modes, and rides through fault without switching controls in all modes.

The next chapter will evaluate parallel operation of the VSM with SGs, investigating LFOs and the network stability.

4. IMPACT OF VIRTUAL SYNCHRONOUS MACHINES ON LOW-FREQUENCY OSCILLATIONS IN POWER SYSTEMS

4.1 Introduction

The LFOs inherent in power systems will be impacted by the increasing penetration of RESs. This chapter investigates the impact of VSM based RESs on the LFOs in power systems. A detailed two-machine test-bed has been developed to analyze the LFOs which exists when VSMs replace SGs. The characteristics of the LFO modes and the dominant states have been comprehensively analyzed. Furthermore, this study analyzes the LFO modes which exists in an all-VSM grid. The role of PSSs in the all-VSM grid has been comprehensively evaluated. The IEEE benchmark two-area four-machine system has been employed to corroborate the results of the small-signal analysis and observe the transient performance. The analysis in this chapter have been performed in MATLAB/SIMULINK environment.

It should be noted that the results presented in this chapter have been published in the IEEE Transactions on Power Systems Journal [175].

4.2 Problem Definition

VSMs have been adopted as a grid-friendly approach to integrate large-scale RESs into the grid [34]. However, since VSMs emulate the dynamics of the SGs, they may also exhibit some of the undesirable characteristics of the SG [150]. This chapter analyses the impact of VSMs on the LFOs in power systems. Considering that fast-acting AVRs and voltage controllers (from the SGs and VSMs respectively)

adequately cater for the power systems synchronizing torque [3], [176], thus VSMs mainly impact the LFOs by [36]:

(1) Replacing the SGs dynamics with the VSMs dynamics, thereby impacting the modes (oscillatory and non-oscillatory).

(2) VSMs impacting damping torque of SGs.

(3) VSMs displacing SGs integrated with PSS.

As discussed in chapter 2, several techniques have been proposed to improve the power systems LFOs using VSMs. However, there are some research gaps as detailed below:

- Studies in [70], [136] attempt to minimize the impact of VSMs on the power systems LFOs by modifying the parameters of the VSMs; however, this approach leads to sub-optimal performance of the VSM. Also, it may not provide sufficient damping for LFOs emanating from SGs.
- The analytical studies in [70], [150], [152], [153] do not provide an holistic insight on the system stability as they neglect the dynamics of some controllers, e.g. reactive power control, voltage control and current control.
- Some of the past works (e.g. [150]) only consider LFOs in an all-VSM grid, and neglect the integration of VSMs with SG. Hence, the net impact (either positive/negative) of VSMs on the LFOs of power systems (with substantial amount of SGs in operation) cannot be evaluated.
- In some previous studies [130], [150] the network is assumed to be quasi-static. Although this approach is considered accurate for SGs with slow dynamics, since VSMs have much faster dynamics, neglecting the network dynamics can lead to false conclusion on the system stability [158], [177].

It is also noted that some of the schemes proposed in literature (e.g. [70], [136], [151]) are not as efficient as the PSS. Furthermore, none of the previous arts have evaluated the role of PSS in an all-VSM system. In light of the gaps in the previous works, the study in this chapter aims to provide an accurate and comprehensive analysis on the impact of VSMs on the power systems LFOs.

The succeeding sections in this chapter are organized as follows: The modelling of the VSM and the SG dynamics are presented in Section 4.3 and Section 4.4 respectively. The state space model of the network dynamics of a two-machine test-bed is developed in Section 4.5. Section 4.6 presents the comprehensive modal analysis of the two-machine test-bed. Section 4.7 presents the simulation results for the IEEE benchmark two-area four-machine system, which corroborates the analysis in Section 4.6. Section 4.8 concludes the chapter.

4.3 Modelling of the VSM

The VSM proposed in chapter 3 is employed in this chapter. The main addition here is the PSS for damping LFOs. In chapter 3, it has been demonstrated that the dynamics of the VSM dominates the power system response. In order to focus on the impact of the VSM on the LFOs, the details of the prime mover (e.g. wind turbine/solar PV) is not detailed. Also, since it has been demonstrated in chapter 3 that the proposed VSM regulates the DC-bus at a fairly constant value in all operating modes, a constant DC-bus can be employed without loss of accuracy in the system analysis.

4.3.1 Virtual governor and Virtual AVR

The virtual governor performs the same role of regulating the system frequency as described in chapter 3. However, since LFOs are mainly associated with weak systems [3], [116], MPPT is not employed here; rather, P_{set} is determined by the ESOs requirements.

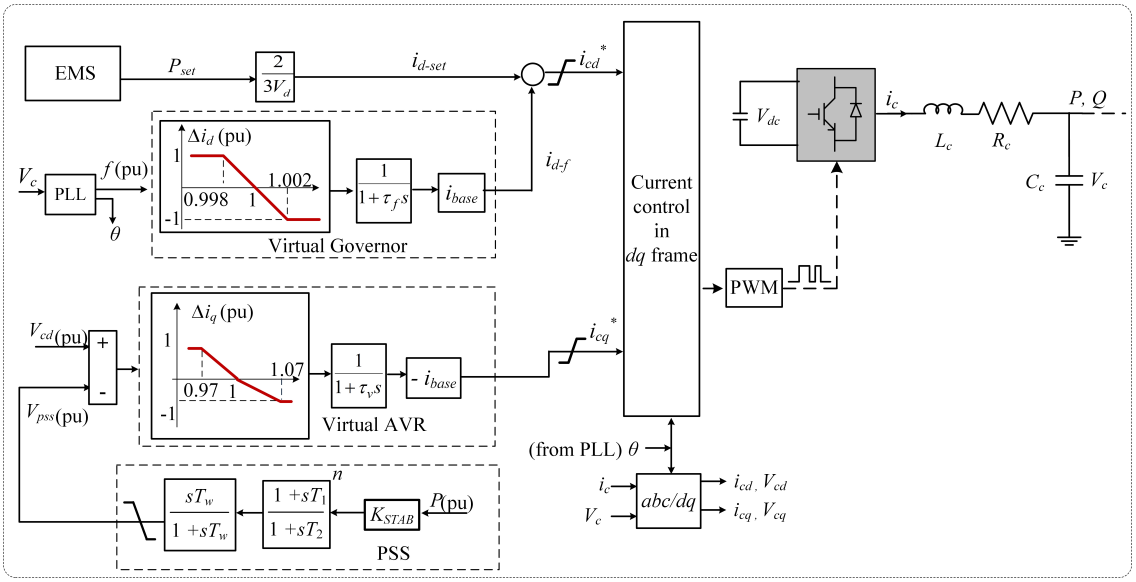

Fig. 4.1. Proposed VSM_{PSS} control structure.

Similarly, the virtual AVR regulates the system voltage as described in chapter 3. In this study, the virtual AVR is integrated with the PSS as illustrated in Fig. 4.1.

4.3.2 Power System Stabilizer

As discussed in chapter 2, the primary function of the PSS is to damp LFOs, thus improving the stability of the power system [3]. The PSS is integrated to the virtual AVR as illustrated in Fig. 4.1. To achieve adequate damping on the system, the input signal of the PSS should contain sufficient information of the system oscillation [132], [134]. Here, we implement the P signal, which is a function of the rotor angle difference $\Delta\delta$ between interconnected machines (for inductive grid) [3], [156]. This enables the use of a local variable (P) with adequate information on remote signals ($\Delta\delta$). The overall equation representing the integration of the virtual AVR with the PSS is given by (4.1):

$$i_q^* = -K_v(V_{cd}^* - (V_{cd} - V_{pss}))(\frac{1}{1+\tau_v s}) \tag{4.1}$$

4.4 Modelling of the Synchronous Generator

The 6th-order model of the SG has been implemented in this study. The equations representing the dynamics of the SG are given by (4.2) [158], [178]:

$$\begin{aligned}
\frac{d\delta}{dt} &= \omega \\
\frac{d\omega}{dt} &= K(3P_{set} - \frac{1}{D}(\omega - \omega^*) + (\frac{3\beta\omega^* - 6L_{ff}L_q\omega^*}{2\beta L_q})\lambda_d\lambda_q + \frac{3L_{af}\omega^*}{\beta}\lambda_q\lambda_f \\
\frac{d\lambda_d}{dt} &= -\frac{2R_aL_{ff}}{\beta}\lambda_d + \omega\lambda_q + \frac{2R_aL_{af}}{\beta}\lambda_f + V_d \\
\frac{d\lambda_q}{dt} &= -\omega\lambda_d - \frac{R_a}{L_q}\lambda_q + V_q \\
\frac{d\lambda_0}{dt} &= -\frac{R_a}{L_0}\lambda_0 + V_0 \\
\frac{d\lambda_f}{dt} &= \frac{3L_{af}\omega^*}{\beta}\lambda_d - \frac{2R_aL_af}{\beta}\lambda_f + V_f
\end{aligned} \tag{4.2}$$

Where,

$$K = \frac{p}{J\omega^*}, \quad \beta = \frac{2L_d}{L_{ff}} - 3L_{af}^2, \quad L_{ff} = \frac{2L_{af}^2}{L_d} \tag{4.3}$$

$$\begin{aligned}
i_{sd} &= \frac{2L_{af}}{\beta}\lambda_f - \frac{2L_{ff}}{\beta}\lambda_d \\
i_{sq} &= \frac{-1}{L_q}\lambda_q \\
i_{s0} &= \frac{-1}{L_0}\lambda_0
\end{aligned} \tag{4.4}$$

The notations D, ω^* and ω respectively represent the damping factor, reference rotor speed and rotor speed. L_d, L_q, L_0, i_{sd}, i_{sq}, i_{s0}, λ_d, λ_q, λ_0 represent the $dq0$ component of the synchronous inductance, stator current and stator flux linkage respectively. L_{af}, L_{ff}, R_f, R_a, λ_f, V_f, i_f, represent the stator to rotor mutual field winding, self-inductance, field winding resistance, armature resistance, field winding flux linkage, field winding voltage and current respectively. K and β are constants relating to the swing equation and inductors respectively. The notations p and J are the pole pairs and rotor inertia respectively. The measured voltage at the bus terminal is represented by V_d, V_q, V_0. For a balanced network, the zero sequence

components are eliminated (i.e. $V_0 = i_{s0} = 0$) [3]. It is assumed that the bus terminal is grounded via a virtual ground R_v as described by (4.5). R_v is modelled with a high resistance, such that it has minimal impact on the network dynamics [157], [179]. The notations i_{dx}, i_{qx}, represent the current measured at the x_{th} node, connecting the SG with the rest of the network.

$$\begin{aligned} V_d &= R_v(i_{sd} - i_{dx}) \\ V_q &= R_v(i_{sq} - i_{qx}) \end{aligned} \tag{4.5}$$

4.5 Modelling of the Network

For the stability analysis in this study, the complete network and load dynamics are modelled in state space as described in [157], [179]. This facilitates an accurate analysis, which takes into account the dynamic interaction of the machines with the network [158], [177]. The configuration of the network is illustrated in Fig. 4.2. The voltage at buses 1, 2, 3 and 4 are represented by V_{dq1}, V_{dq2}, V_{dq3} and V_{dq4} respectively. The state space representation of each component of the network is described below.

4.5.1 Transformer

The transformer is represented by its equivalent leakage impedance [6], [180]. The inductance of the transformer is represented by L_{tr}, and it is assumed that the winding resistance is negligible [6]. The dynamics of the transformers tr_1 and tr_2 (see Fig. 4.2) are represented by (4.6) and (4.7) respectively:

$$\begin{aligned} \frac{di_{d1}}{dt} &= \frac{1}{L_{tr}}V_{d1} + \omega i_{q1} - \frac{1}{L_{tr}}V_{d3} \\ \frac{di_{q1}}{dt} &= \frac{1}{L_{tr}}V_{q1} - \omega i_{d1} - \frac{1}{L_{tr}}V_{q3} \end{aligned} \tag{4.6}$$

$$\begin{aligned} \frac{di_{d2}}{dt} &= \frac{1}{L_{tr}}V_{d2} + \omega i_{q2} - \frac{1}{L_{tr}}V_{d4} \\ \frac{di_{q2}}{dt} &= \frac{1}{L_{tr}}V_{q2} - \omega i_{d2} - \frac{1}{L_{tr}}V_{q4} \end{aligned} \tag{4.7}$$

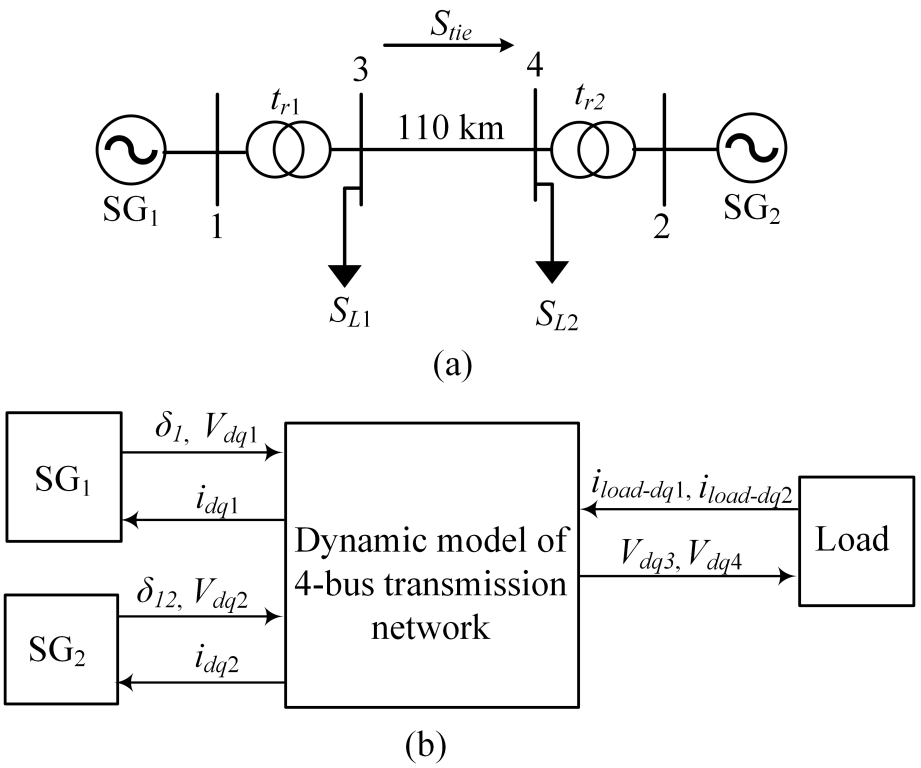

Fig. 4.2. Topology of the two-machine test-bed for small-signal analysis: (a) Single line diagram (b) Signal-flow diagram.

The current in dq flowing through tr_1 and tr_2 are denoted by i_{dq1} and i_{dq2} respectively.

4.5.2 Load

A dynamic RL load is employed in this study. The dynamics of the loads S_{L1} and S_{L2} (see Fig. 4.2) are represented by (4.8) and (4.9) respectively:

$$\begin{aligned}
\frac{di_{load-d1}}{dt} &= \frac{-R_{load}}{L_{load}} i_{load-d1} + \omega i_{load-q1} + \frac{1}{L_{load}} V_{3d} \\
\frac{di_{load-q1}}{dt} &= \frac{-R_{load}}{L_{load}} i_{load-q1} - \omega i_{load-d1} + \frac{1}{L_{load}} V_{3q}
\end{aligned} \tag{4.8}$$

$$\begin{aligned}
\frac{di_{load-d2}}{dt} &= \frac{-R_{load}}{L_{load}} i_{load-d2} + \omega i_{load-q2} + \frac{1}{L_{load}} V_{4d} \\
\frac{di_{load-q2}}{dt} &= \frac{-R_{load}}{L_{load}} i_{load-q2} - \omega i_{load-d2} + \frac{1}{L_{load}} V_{4q}
\end{aligned} \tag{4.9}$$

The current in dq flowing into S_{L1} and S_{L2} are respectively represented by $i_{load-dq1}$ and $i_{load-dq2}$. The notations R_{load} and L_{load} represent the equivalent resistance and inductance of the load respectively.

4.5.3 Transmission tie-line

The transmission tie-line plays an important role on the stability of interconnected power systems [33]. Large disturbances (e.g. 3-phase fault) on transmission tie-lines can lead to power split or blackout if adequate damping measures are not in place [3], [116]. The tie-line is represented by an equivalent nominal π circuit [3], [180]. The tie-line dynamics are described below (4.10)−(4.15):

$$\frac{dV_{d3}}{dt} = \omega V_{3q} + \frac{1}{C/2}\left(i_{d1} - i_{tie-d} - i_{load-d1}\right) \tag{4.10}$$

$$\frac{dV_{q3}}{dt} = -\omega V_{3d} + \frac{1}{C/2}\left(i_{q1} - i_{tie-q} - i_{load-q1}\right) \tag{4.11}$$

$$\frac{di_{tie-d}}{dt} = \frac{-R}{L} i_{tie-d} + \omega i_{tie-q} + \frac{1}{L} V_{3d} - \frac{1}{L} V_{4d} \tag{4.12}$$

$$\frac{di_{tie-q}}{dt} = \frac{-R}{L} i_{tie-q} - \omega i_{tie-d} + \frac{1}{L} V_{3q} - \frac{1}{L} V_{4q} \tag{4.13}$$

$$\frac{dV_{d4}}{dt} = \omega V_{4q} + \frac{1}{C/2}\left(i_{d2} + i_{tie-d} - i_{load-d2}\right) \tag{4.14}$$

$$\frac{dV_{q4}}{dt} = -\omega V_{4d} + \frac{1}{C/2}\left(i_{q2} + i_{tie-q} - i_{load-q2}\right) \tag{4.15}$$

The notations R, L and C respectively represent the resistance, inductance and shunt capacitance of the transmission line. From Fig. 4.2, it is observed that there is a net power flow on the tie-line S_{tie} from V_{dq3} to V_{dq4}. This is modelled by subtracting the current flowing in the tie-line i_{tie-dq} from V_{dq3} (see (4.10) & (4.11)) and adding it to V_{dq4} (see (4.14) & (4.15)) [3].

4.6 Small-Signal Stability Analysis

The small-signal stability study of power systems is primarily concerned with the nature of the angular oscillations, when the system is subjected to small disturbances [3]. The angular oscillations of interest are the LFOs [33], [133]. A single machine infinite bus model is commonly used to observe the stability and performance of SGs [3], [6]. However, this may not be adequate for systems containing diverse RESs, as it is unable to elucidate the interaction between the various power generating sources

in the network. Hence in this study, a detailed two-machine test-bed has been developed which offers an excellent platform for the observation and comprehensive analyses of the interaction of modes between the SG and VSM. It is noted that the proposed test-bed is an adaptation of the IEEE two-area four-machine benchmark model. The topology of the test-bed is illustrated in Fig. 4.2, and the dynamics of each components have been detailed in section 4.3−4.5. In order to investigate the small-signal stability analysis, all units in the system must be synchronized to a common reference frame [3], [6]. The rotating frame of an arbitrary machine is chosen as the common reference frame DQ_j [3]. The output variables of the ith machine rotating at dq_i is translated to DQ_j using the output transformation operator T_{out} (4.17), while the input variables on DQ_j are translated to dq_i using the input transformation operator T_{in} (4.19) [157], [158].

$$\begin{bmatrix} f_{DQ} \end{bmatrix} = \begin{bmatrix} T_{out} \end{bmatrix} \begin{bmatrix} f_{dq} \end{bmatrix} \tag{4.16}$$

$$\begin{bmatrix} T_{out} \end{bmatrix} = \begin{bmatrix} cos(\delta_{ij}) & -sin(\delta_{ij}) \\ sin(\delta_{ij}) & cos(\delta_{ij}) \end{bmatrix} \tag{4.17}$$

$$\begin{bmatrix} f_{dq} \end{bmatrix} = \begin{bmatrix} T_{in} \end{bmatrix} \begin{bmatrix} f_{DQ} \end{bmatrix} \tag{4.18}$$

$$\begin{bmatrix} T_{in} \end{bmatrix} = \begin{bmatrix} cos(\delta_{ij}) & sin(\delta_{ij}) \\ -sin(\delta_{ij}) & cos(\delta_{ij}) \end{bmatrix} \tag{4.19}$$

Where f_{DQ} and f_{dq} are the machine variables represented on DQ_j and dq_i respectively, δ_{ij} is the angular difference between DQ_j and dq_i. Fig. 4.3 illustrates the

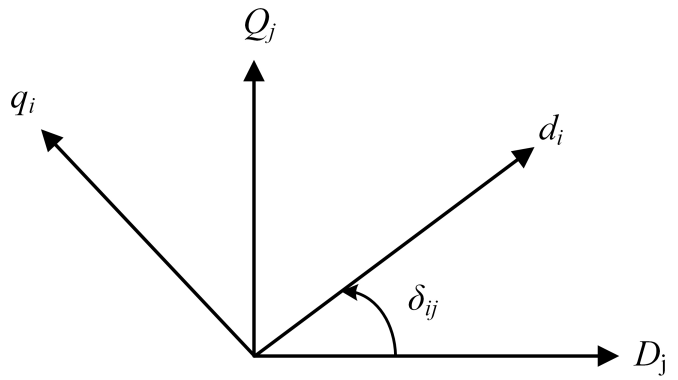

Fig. 4.3. Reference frame transformation [3].

dq reference frame transformation. The output and input of each machine are the machine voltage and current respectively. The states of the two-machine test-bed are given below:

$$\begin{aligned} x_{VSM} &= \begin{bmatrix} \theta & \omega_{PLL} & i^*_{cdq} & \gamma_{odq} & i_{cdq} & V_{cdq} \end{bmatrix} \\ x_{VSM_{PSS}} &= \begin{bmatrix} \theta & \omega_{PLL} & i^*_{cdq} & \gamma_{odq} & i_{cdq} & V_{cdq} & V_{pss} \end{bmatrix} \\ u_{VSM} &= u_{VSM_{PSS}} = \begin{bmatrix} V^*_{cd} & f^* & P_{set} \end{bmatrix} \end{aligned} \tag{4.20}$$

$$\begin{aligned} x_{SG} &= \begin{bmatrix} \delta & \omega & \lambda_{dq0} & \lambda_f \end{bmatrix} \\ u_{SG} &= \begin{bmatrix} \omega^* & P_{set} \end{bmatrix} \end{aligned} \tag{4.21}$$

$$\begin{aligned} x_{net} &= \begin{bmatrix} i_{dq1} & i_{dq2} & i_{tie-dq} & i_{load-dq1} & i_{load-dq2} & V_{dq3} & V_{dq4} \end{bmatrix} \\ u_{net} &= \begin{bmatrix} V_{dq1} & V_{dq2} \end{bmatrix} \end{aligned} \tag{4.22}$$

The states of the VSM & VSM_{PSS}, SG and network are respectively represented by (4.20), (4.21) and (4.22) respectively. The network state equations are all represented on the common reference frame [157], [178]. The complete state space model

Tab. 4.1. System's parameters

VSM		
Parameter	Value	
Current Loop PI control	K_p = 9e−4	K_i = 9e−3
t_f, t_v	1.3 s,	0.005 s
PLL PI control	K_p = 0.005	K_i = 0.05
Filter impedance	R_c = 0.008 pu	L_c = 0.3 pu
SG		
Parameter	Value (pu)	
H, p	6, 2	
R_a, R_f, R_v	0.02, 0.368, 8	
L_d, L_q, L_0, L_{af}	0.6, 0.6, 0.06, 7.07	
D	0.002	
Transmission network		
Line impedance	R = 9e−4 pu/km, X_L = 9e−3 pu/km, b_c= 1.58e−3 pu/km	
Transformer impedance	X_{tr} = 0.15 pu	
S_{L1}, S_{L2}, S_{tie}	0.4 pu, 0.8 pu, 0.36 pu (at 0.85 PF)	

of the test system is modelled in MATLAB/SIMULINK. The linearized model of the complete system is represented by $\boldsymbol{\Delta\dot{x}} = \boldsymbol{A\Delta x} + \boldsymbol{B\Delta u}$ and is obtained in MATLAB using the linear analysis toolbox.

The stability analysis in this study analyzes the: (A) impact of SG replacement by VSM (B) robustness of the VSM_{PSS} (C) stability of an all-VSM grid (D) the role of PSS in these scenarios. The system's parameters are detailed in Table 4.1. The machine and network parameters have a base rating of 900 MVA. The nominal voltage at the SG terminal and transmission network are 20 kV and 230 kV respectively. The initial operating point for the machines are P_{set} = 0.8 pu.

4.6.1 Impact of SG replacement by VSM

The objective here is to observe the LFO modes when SGs are replaced by VSMs. To achieve this, we consider three system configurations on the test-bed (see Fig. 4.2):

Tab. 4.2. Dominant eigenvalues for sub-section 4.6.1

SG-SG			
Pole	Mode	Damping Ratio (ζ)	Dominant states
$\lambda_{1,2}$	-0.017 ± 5.52	0.003	$\Delta\delta_{12}$, $\Delta\omega_1$, $\Delta\omega_2$
SG-VSM			
Pole	Mode	Damping Ratio (ζ)	Dominant states
$\lambda_{1,2}$	-0.242 ± 2.62	0.092	$\Delta\delta_{12}$, $\Delta\omega_1$, Δi^*_{cd2}
$\lambda_{3,4}$	-1.58 ± 4.44	0.335	$\Delta\delta_{12}$, $\Delta\omega_{PLL2}$, Δi^*_{cd2}
SG-VSM$_{\text{PSS}}$			
Pole	Mode	Damping Ratio (ζ)	Dominant states
$\lambda_{1,2}$	-0.584 ± 2.46	0.23	$\Delta\delta_{12}$, $\Delta\omega_1$, Δi^*_{cd2}, ΔV_{pss}
$\lambda_{3,4}$	-4.3 ± 4.62	0.681	$\Delta\omega_{PLL2}$, Δi^*_{cd2}, ΔV_{pss}
$\lambda_{5,6}$	-0.87 ± 3.82	0.209	$\Delta\delta_{12}$, $\Delta\omega_{PLL2}$, ΔV_{pss}

(1) The stability of the test system with two SGs (SG-SG)

(2) Replacing SG_2 with VSM (SG-VSM)

(3) Addition of PSS to VSM (SG-VSM$_{\text{PSS}}$)

For this test, PSS is not utilized for the SG as this has been well established in literature [3], [6]. Fig. 4.4 illustrates the location of the dominant system poles for the three test configurations. Table 4.2 illustrates the damping ratio (ζ) and dominant states affecting the LFO modes. The dominant states are obtained using participation factor matrix (p_k)[3].
The subscript 1 and 2 in the last column of Table 4.2 denote the dominant states relating to machine 1 and 2 respectively.

(1) SG-SG: For the first configuration, (see Fig. 4.4(a)). It is observed that, with 2 SGs (with no PSS) the system is marginally stable as a pair of poles oscillating at 5.52 rad/s are situated very close to the $j\omega$-axis. From Table 4.2, it is observed that

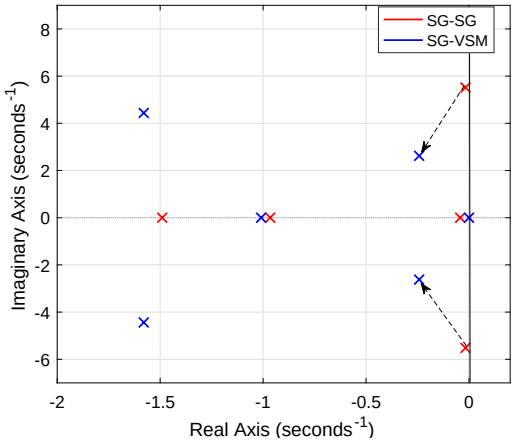

(a) Comparison of the LFO when VSM replaces SG

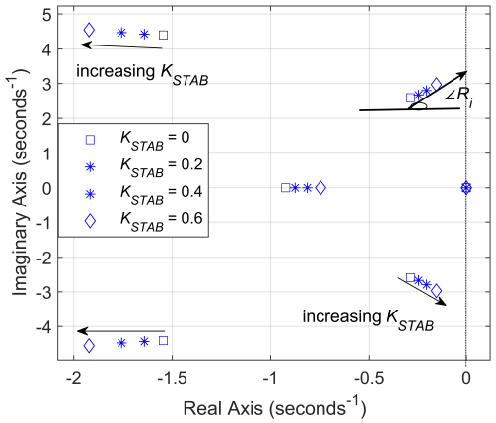

(b) Transition of LFO modes with direct feedback of P without lead-lag compensators

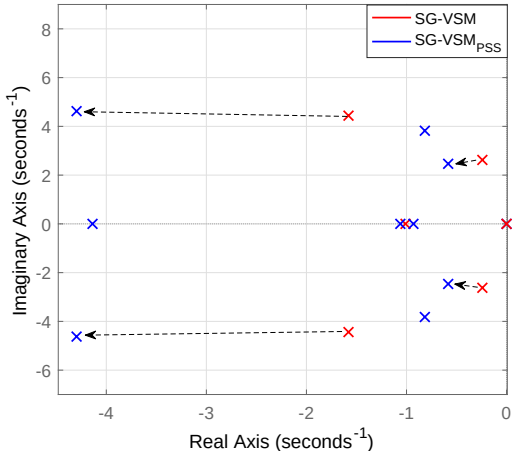

(c) Comparison of the LFO when PSS is employed on VSM

Fig. 4.4. Impact of SG replacement by VSM.

this poles are rotor angle modes (i.e. dominated by $\Delta\delta_{12}$, $\Delta\omega_1$ and $\Delta\omega_2$) and $\zeta = 0.003$. This implies that a disturbance in the system will lead to continuous angular oscillations which do not decay with time, due to insufficient damping torque.

(2) SG-VSM: With SG_2 replaced by the VSM (see Fig. 4.4(a)), two oscillatory poles $\lambda_{1,2}$ and $\lambda_{3,4}$ are observed. The poles $\lambda_{1,2}$ oscillates at 2.62 rad/s and is dominated by $\Delta\delta_{12}$, $\Delta\omega_1$ and Δi^*_{cd2} (from the VSM's virtual governor). Whereas, $\lambda_{3,4}$ oscillates at 4.44 rad/s, and is dominated by $\Delta\delta_{12}$, Δi^*_{cd2} and $\Delta\omega_{PLL2}$ (from the VSM's PLL). This system is stable as the poles are all located on the left hand side (LHS) of the $j\omega$-axis. It is also noted that the damping ratio of $\lambda_{1,2}$ has increased. However, it is still not well-damped ($\zeta = 0.092$). It is noted that, although [136] suggests retuning the VSM's parameters, retuning an already well-designed VSM, may exacerbate other modes and deteriorate the VSM performance. As an alternative, since the VSM is designed to emulate the SG, some of the supplementary controls (e.g. PSS) employed on the SG, should be applicable on the VSM to enhance the power system stability.

(3) $SG\text{-}VSM_{PSS}$: For this configuration, the PSS shown in Fig. 4.1 is employed on the VSM. From Fig. 4.4(b), it is observed that a direct feedback of P (without lead-lag compensators) exacerbates the dominant LFO mode (λ_{12}) in the SG-VSM configuration. Hence, to achieve the desired damping on the LFO modes, the PSS must be systematically designed. Two crucial parameters in the design of the PSS are the oscillatory frequency ω_{osc} and the phase lead ϕ_{lead} on the lead-lag compensator [6]. In this study, the required ϕ_{lead} is obtained using the residue approach [107], [129]. The residue angle $\angle R_i$ (see Fig. 4.4(b)), at which λ_{12} approaches the $j\omega$-axis is obtained from the transfer function $G_{res}(s) = P/V^*$. Here $\angle R_i \approx 60°$, hence the required $\phi_{lead} = 120°$ i.e. $\phi_{lead} = 180° - \angle R_i$. The primary consideration in selecting ω_{osc} for the PSS, is to achieve maximum damping on the critical

modes. This is usually the inter-area modes which are usually under-damped due to weak interconnecting tie-lines [130], [33]. In this study, ω_{osc} is chosen as 4.21 rad/s which ensures adequate damping for the LFO modes of interest. It is noted that for complex PSS designs i.e. multi-band PSS (MB-PSS), more than one ω_{osc} value is normally chosen within the LFO range [107]. For optimum performance, it is desirable to limit the maximum ϕ_{lead} of each compensator, such that $\phi_{lead} < 60^{o}$ [107]. Hence, three identical lead-lag compensators (n=3) with $\phi_{lead} = 40°$ are implemented; such that T_1 and T_2 are 0.509 and 0.11 respectively. K_{pss} is chosen on the premise of achieving sufficient damping, whilst also avoiding controller saturation (which might occur due to very high K_{pss}). Here, K_{pss} is chosen as 0.12.
To ensure fast response of the VSM, while passing the desired low frequencies, T_w = 1 s.

From Fig. 4.4(c), it is observed that by employing the PSS, an additional oscillatory mode $\lambda_{5,6}$ is introduced into the system. This mode is dominated by $\Delta\delta_{12}$, $\Delta\omega_{PLL2}$ and ΔV_{pss}. It is also observed that, the dominant modes in $\lambda_{1,2}$ and $\lambda_{3,4}$ are similar to configuration 2. However, ΔV_{pss} is also dominant on $\lambda_{1,2}$ and $\lambda_{3,4}$. From Fig. 4.4(c), it is observed that the inclusion of the PSS moves the oscillatory modes further to the LHS, indicating improved stability and damping. As detailed in Table 4.2, the ζ for $\lambda_{1,2}$ and $\lambda_{3,4}$ have increased to 0.23 and 0.681 respectively, which are now well-damped.

4.6.2 Robustness of the VSM_{PSS}

Consider the testbed in Fig. 4.2, where P_1 and P_2 represent the active power generated by SG_1 (or VSM_1) and SG_2 (or VSM_2) respectively, and P_L represents the aggregated active load (i.e. $P_{L1} + P_{L2} = P_L$). Since the network is mainly inductive (i.e. $X_L \gg R$), one can assume that the SGs (or VSMs) rotor angles are small (i.e. $\sin\delta_i \approx \delta_i$), and the system voltage deviation is negligible (i.e. $V_1 = V_2 \approx 1$ pu). The linear equation representing the active power flow in the network can be represented

by (4.23) [181]:

$$\begin{aligned}\Delta P_1 &= \frac{1}{X_{L1}}(\Delta\delta_1 - \Delta\delta_L)\\ \Delta P_2 &= \frac{1}{X_{L2}}(\Delta\delta_2 - \Delta\delta_L)\\ \Delta\delta_L &= \frac{\Delta\delta_1 X_{L2} + \Delta\delta_2 X_{L1} - \Delta P_L X_{L1} X_{L2}}{X_{L1} + X_{L2}}\end{aligned} \tag{4.23}$$

Where δ_L is the load angle, while X_{L1} and X_{L2} respectively represent the reactance of the transmission line connecting SG_1 (or VSM_1) and SG_2 (or VSM_2) to P_L. From (4.23), assuming that $\Delta\delta_1$ and $\Delta\delta_2$ are very small i.e. $\Delta\delta_1 = \Delta\delta_2 \approx 0$, $\Delta\delta_L$ can be represented as:

$$|\Delta\delta_L| \approx \frac{\Delta P_L X_{L1} X_{L2}}{X_{L1} + X_{L2}} \tag{4.24}$$

From (4.24), it is observed that variations in the loading condition ΔP_L and in the reactance of the transmission line ΔX_L are the main grid parameters that impact the small-signal (angular) stability of the system. It is noted that for a given transmission line, X_L is proportional to the length of the transmission line. Hence, the robustness of the VSM_{PSS} will be evaluated for (1) variations in the system loading, (2) variations in the length of the transmission tie-line l_{tie}. The SG-VSM_{PSS} setup in sub-section 4.6.1 is employed here.

(1) Impact of varying system loading: To observe the stability of the VSM_{PSS} for varying load conditions, S_{L2} is varied from 0.6–1.2 pu. For the purpose of comparison, a scenario without PSS is also shown in the result. The Bode plot of the system frequency response is observed using the virtual governor loop, with f^* and f taken as the input and output of the open loop transfer function $G_f(s)$ respectively i.e. $G_f(s) = f/f^*$. From Fig. 4.5, it is observed that without the PSS, although the phase margin (PM) is satisfactory i.e. PM = 35°, the system has a relatively sharp peak at 2.6 rad/s which indicates poor damping. With the VSM_{PSS}, the peak is eliminated for all scenarios indicating satisfactory damping. Furthermore, the PM is significantly improved for all configurations i.e. 93°≤ PM ≤ 106°. The gain

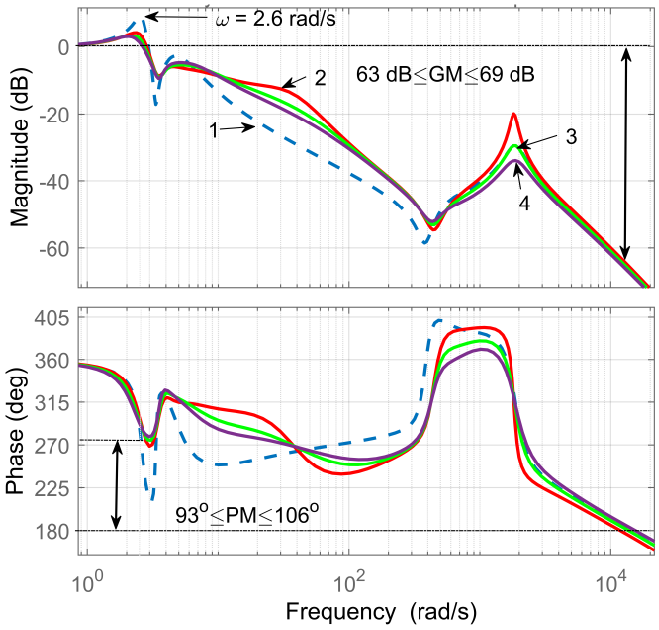

Fig. 4.5. Impact of varying load on VSM_{PSS} stability:1–S_{L2} = 0.9 pu no PSS, 2–S_{L2} = 0.6 pu with PSS, 3–S_{L2} = 0.9pu with PSS, 4–S_{L2} = 1.2 pu with PSS.

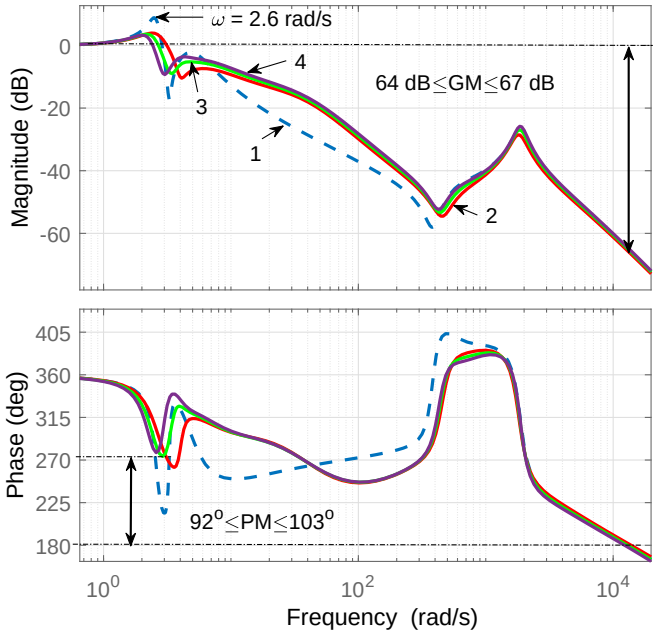

Fig. 4.6. Impact of varying length of tie-line on VSM_{PSS} stability: 1–l_{tie} = 120 km no PSS, 2–l_{tie} = 80 km with PSS, 3–l_{tie} = 120 km with PSS, 4–l_{tie} = 160 km with PSS.

margin (GM) for all scenarios is satisfactory, and is not impacted by the PSS i.e. 63 dB $\leq$ GM $\leq$ 69 dB.

(2) Impact of variations in the length of the tie-line: The test here analyses the VSM_{PSS} stability for different l_{tie}, varying from 80–160 km. The frequency response is also observed using $G_f(s) = f/f^*$. From Fig. 4.6, it is observed that without the PSS, although the PM is satisfactory (i.e. PM = 38°) the system is not well damped at ω = 2.6 rad/s. With the VSM_{PSS} employed, the system is well damped for all scenarios and the PM is improved i.e. 92°$\leq$ PM $\leq$ 103°. The GM for all scenarios is satisfactory, and is not impacted by the PSS i.e. 64 dB $\leq$ GM $\leq$ 67 dB.

4.6.3 Stability analysis of an all-VSM grid

The objectives here are to observe: (a) if the LFO modes observed in the SGs exists for an all-VSM grid (b) the states participating in the LFO (c) the impact of PSS on the overall system stability. To achieve this, two configurations are investigated:

Tab. 4.3. Dominant eigenvalues for sub-section 4.6.3

VSM-VSM			
Pole	Mode	Damping	Dominant states
$\lambda_{1,2}$	-1.22 ± 4.44	0.265	$\Delta\delta_{12}$, $\Delta\omega_{PLL1}$, $\Delta\omega_{PLL2}$, i^*_{cd1}, i^*_{cd2}
$\lambda_{3,4}$	-2.93 ± 6.19	0.428	$\Delta\omega_{PLL1}$, $\Delta\omega_{PLL2}$, i^*_{cd1}, i^*_{cd2}
VSM_{PSS}-VSM_{PSS}			
Pole	Mode	Damping	Dominant states
$\lambda_{1,2}$	-3.15 ± 4.49	0.575	$\Delta\delta_{12}$, $\Delta\omega_{PLL1}$, $\Delta\omega_{PLL2}$, i^*_{cd1}, i^*_{cd2}, ΔV_{pss}
$\lambda_{3,4}$	-5.75 ± 5.33	0.734	$\Delta\omega_{PLL1}$, $\Delta\omega_{PLL2}$, i^*_{cd1}, i^*_{cd2}, ΔV_{pss}
$\lambda_{5,6}$	-1.42 ± 3.58	0.368	$\Delta\delta_{12}$, $\Delta\omega_{PLL1}$, $\Delta\omega_{PLL2}$, i^*_{cd1}, i^*_{cd2}, ΔV_{pss}
$\lambda_{7,8}$	-1.28 ± 3.89	0.3	$\Delta\delta_{12}$, $\Delta\omega_{PLL1}$, $\Delta\omega_{PLL2}$, ΔV_{pss}

(1) Both SGs in Fig. 4.2 are replaced by VSMs (VSM-VSM).

(2) PSS added on both VSMs (VSM_{PSS}-VSM_{PSS}).

1) VSM-VSM: It is observed from Fig. 4.7 that the system is stable as all the modes are on the LHS of the $j\omega$-axis. Two modes $\lambda_{1,2}$ and $\lambda_{3,4}$ are observed oscillating at 4.44 rad/s and 6.19 rad/s respectively. These modes are dominated by states from the PLL and governor. However, $\Delta\delta_{12}$ has minimal influence on $\lambda_{3,4}$. From Table 4.3, it is observed that these modes are well damped. Moreover, comparing this configuration with the SG-SG and SG-VSM configurations (see subsection 4.6.1), it is observed that the two modes ($\lambda_{1,2}$ and $\lambda_{3,4}$) are much better damped in the VSM-VSM.

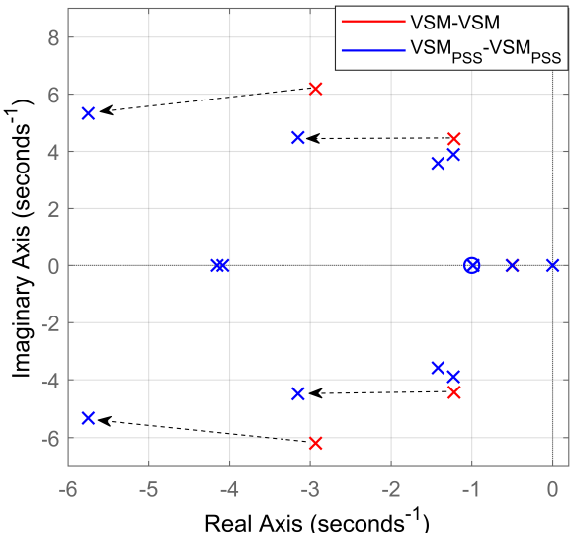

Fig. 4.7. Impact of PSS on LFO in an all-VSM grid.

2) VSM_{PSS}-VSM_{PSS}: With the inclusion of PSS, two additional modes $\lambda_{5,6}$ and $\lambda_{7,8}$ are introduced in the system. These modes are dominated by states from the PLL, virtual governor and PSS. It is observed from Fig. 4.7, that the PSS moves the modes further to the LHS indicating improved stability and damping (see Table 4.3).

The observation from the small-signal analysis shows that, the replacement of SGs

with VSMs improves the damping of inter-area LFOs. However, PSS is required for satisfactory operation. It is also observed that the VSM_{PSS} is robust to variations in the system operating condition. Furthermore, an all-VSM grid can operate satisfactorily without the need for a PSS, as the LFO modes are well damped. Although the PSS can improve the stability of an all-VSM grid, it is not a requirement as is the case for SG dominated grids. It is noted that, as with all control designs, the above conclusion will not be valid for a poorly tuned VSM.

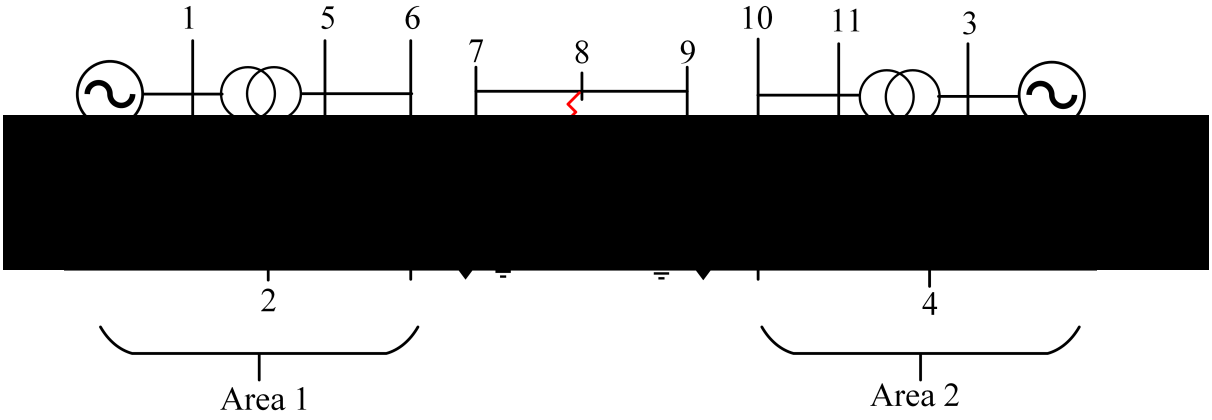

Fig. 4.8. IEEE benchmark two-area four-machine system [3]

4.7 Transient stability

The objective of this section is to observe the dynamics of the system when subjected to large disturbances. To achieve this, the IEEE benchmark two-area four-machine system (also known as Kundur model) has been implemented (see Fig. 4.8). This system (Fig. 4.8) is the dedicated IEEE benchmark for investigating LFOs and the role of PSS in power systems [182]. The full-order MATLAB/SIMULINK model of the SG with AVR and governor has been employed here. The SG and network parameters are detailed in [3], while the VSM parameters are detailed in Table. 4.1. In Figs. 4.9–4.22, $\Delta\delta_{12}$, $\Delta\delta_{13}$ and $\Delta\delta_{14}$ represent the relative angular oscillation of SG_2 (or VSM_2), SG_3 (or VSM_3) and SG_4 (or VSM_4) with respect to SG_1 (or VSM_1). P_1, P_2, P_3 and P_4 represent the active power generated from SG_1 (or VSM_1), SG_2

(or VSM_2), SG_3 (or VSM_3) and SG_4 (or VSM_4) respectively. Q_1, Q_2, Q_3 and Q_4 represent the reactive power generated from SG_1 (or VSM_1), SG_2 (or VSM_2), SG_3 (or VSM_3) and SG_4 (or VSM_4) respectively. The V and f are measured at bus 7 (see Fig. 4.8). Three test cases have been investigated:

(A) Impact of VSM replacing SG.

(B) Robustness of the VSM_{PSS}.

(C) Evaluation of an all-VSM with respect to an all-SG grid.

4.7.1 Impact of VSM replacing SG

To observe the transient stability of the system, a 3-phase fault is applied on the tie-line at bus 8 (see Fig. 4.8) at t = 20 s for a period of 200 ms. Four system configurations are observed:

- Configuration 1: four SGs with no PSS (4SG).
- Configuration 2: SG_2 and SG_4 replaced by VSMs (2SG-2VSM).
- Configuration 3: PSS added to the two SGs in configuration 2 ($2SG_{pss}$-2VSM).
- Configuration 4: PSS added to the two VSMs in configuration 2 (2SG-$2VSM_{pss}$).

The standard MB-PSS available on MATLAB/SIMULINK which offers the best performance is implemented on the SGs, while the PSS designed in section 4.6.1 is implemented on the VSMs. This offers a good base-line evaluation on the efficacy of the PSS employed on the VSM. The results of these tests are shown in Figs. 4.9–4.12, which are discussed as follows:

(a) Angle stability: From Fig. 4.9, it is observed that the oscillation is an inter-area mode i.e. $\omega_{osc} \approx 4.2 rads^{-1}$, with machines in Area 1 swinging against machines in Area 2; δ_{13} and δ_{14} are much larger than δ_{12}. For configuration 1, the system loses synchronization as the amplitude of the angular oscillations progressively increases after fault, indicating lack of sufficient damping torque. For configuration 2, it is

observed that the system is stable but poorly damped; as the angular oscillations do not increase post-fault, but will take a long period of time to be damped out. For configuration 3, due to the addition of the MB-PSS on SG_1 and SG_3, the oscillation is rapidly damped and the system maintains synchronism. For configuration 4, with the addition of PSS to the VSMs, the system oscillations are promptly damped out. It is observed that the performance of the PSS on the VSM (See Fig. 4.1), is very comparable to the MB-PSS on the SG. Hence, a complex PSS design is not required on the VSM to obtain satisfactory performance.

(b) Active power oscillation: For configuration 1 (see Fig. 4.10), it is observed that the power oscillations progressively increases post-fault as the system is unstable. For configuration 2, the power oscillations do not increase but will take long time to be damped out. It is also observed that the inertial response from the SG is more dominant, ensuring quicker power recovery from the SG post-fault. Due to the surge in power from the SGs (P_1 and P_3), the VSMs (P_2 and P_4) seems to recover slowly to maintain power balance in the system. For configuration 3, the power oscillation is promptly damped and the system maintains stability. For configuration 4, the power oscillation is also effectively damped and it is observed that the active power dip is less than all other scenarios. This is a result of the increased Q injection due to PSS action, which leads to a corresponding reduction in voltage sag (see Fig. 4.12(a)).

(c) Reactive power injection: It is observed (see Fig. 4.11) that, the Q injected in configuration 1 and configuration 2 are comparable, though Q is slightly less in configuration 1. In configuration 3, it is observed that the increased Q injection on SG_1 and SG_3 is accompanied by transient absorption of Q in the VSMs (Q_2 and Q_4) to maintain Q balance in the system. Similarly, in configuration 4 the SGs (Q_1 and Q_3) transiently absorb Q due to the increased Q injection on the VSMs employing PSS. In comparison with the other scenarios, configuration 4 injects the maximum Q during fault, thus ensuring the best voltage support.

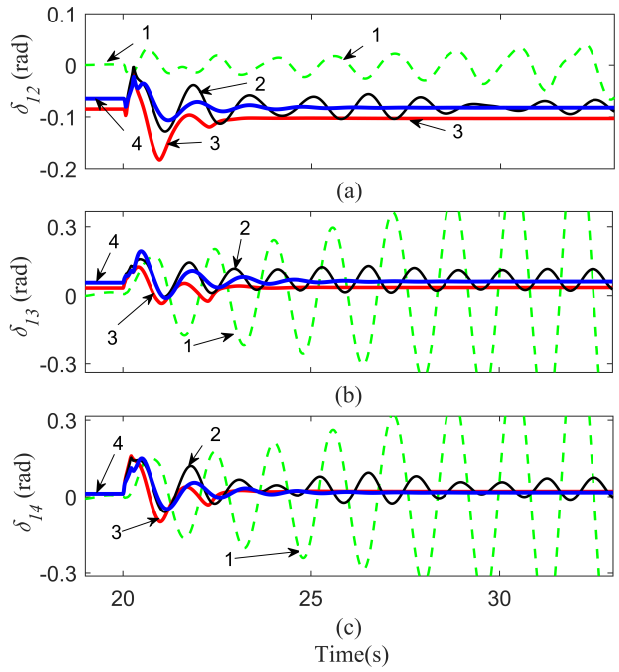

Fig. 4.9. Rotor angle: 1−4SG, 2−2SG-2VSM, 3−2SG$_{pss}$-2VSM, 4−2SG-2VSM$_{pss}$.

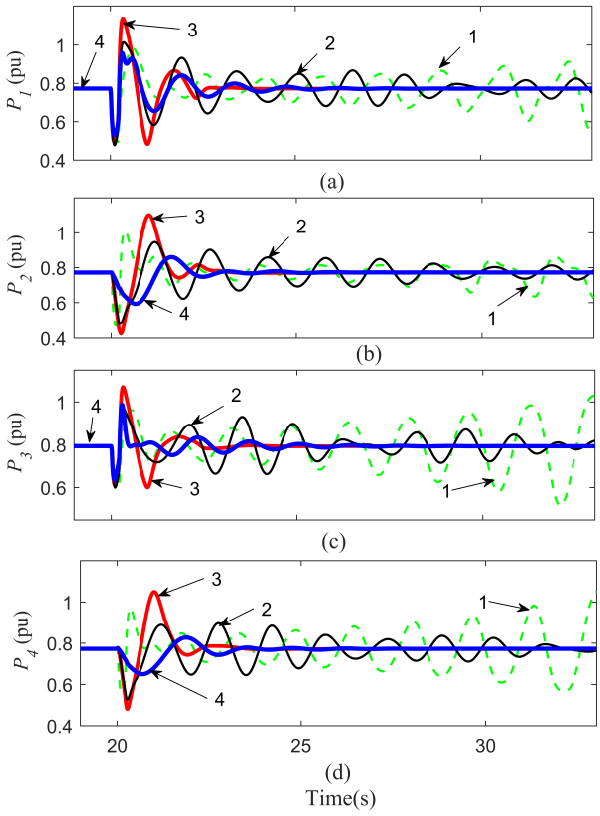

Fig. 4.10. Active Power (pu):1−4SG, 2−2SG-2VSM, 3−2SG$_{pss}$-2VSM, 4−2SG-2VSM$_{pss}$.

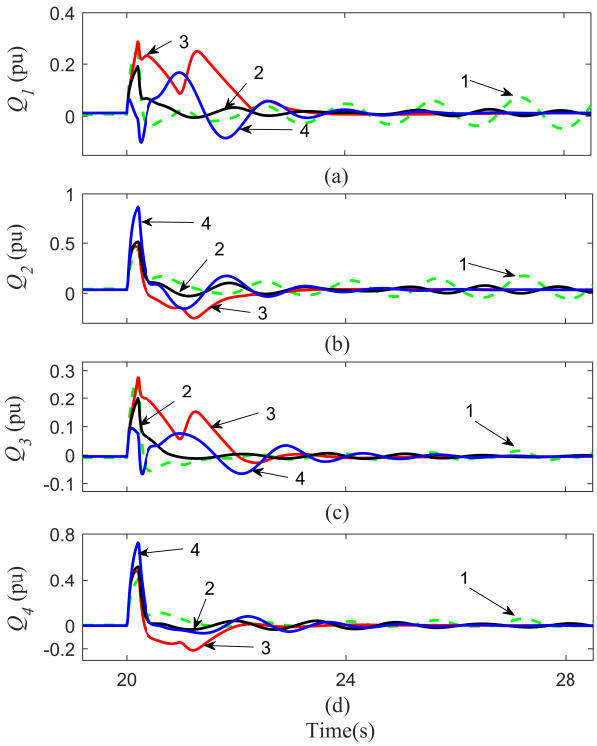

Fig. 4.11. Reactive Power (pu): 1−4SG, 2−2SG-2VSM, 3−2SG$_{\text{pss}}$-2VSM, 4−2SG-2VSM$_{\text{pss}}$.

(d) Voltage: It is observed (see Fig. 4.12(a)) that the voltage dip in configurations 2 and 3 are similar. The voltage dip in configuration 1 is the largest because it injects the least Q during fault. On the contrary, the smallest voltage dip is observed in configuration 4 due to the maximum Q injected. This ensures a better voltage support in configuration 4 than all other configurations. The post-fault voltage swell and dip observed on configuration 3 and configuration 4 respectively, are due to the stabilizing signals injected into the system by the PSS.

(e) Frequency: It is observed (see Fig. 4.12(b)), that configuration 1 exhibits the least deviation during fault. For configurations 2–4, the frequency is maintained within nominal value ±1% [37], and is not impacted by the PSS. From this test, it is observed that the replacement of SGs with VSM improves damping of inter-area LFOs. However, PSS is required for satisfactory performance.

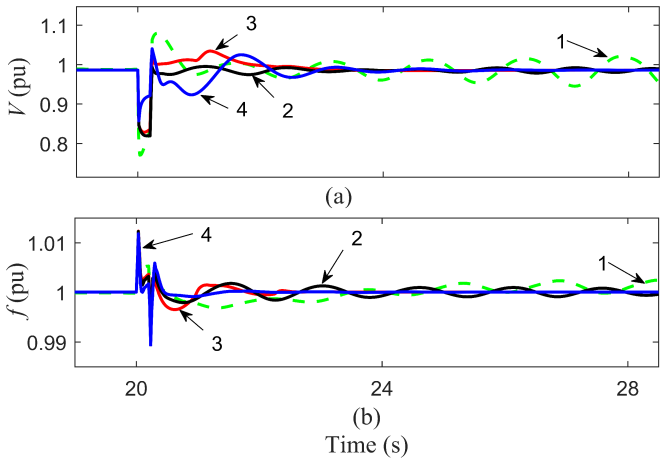

Fig. 4.12. (a) Voltage (pu): 1−4SG, 2−2SG-2VSM, 3−2SG$_{pss}$-2VSM, 4−2SG-2VSM$_{pss}$.
(b) Frequency (pu): same as (a).

4.7.2 VSM$_{PSS}$ Robustness test

To evaluate the robustness of the VSM$_{PSS}$ (see Fig. 4.1), the following scenarios are simulated on the same SG (or VSM) configuration as sub-section 4.7.1:

(1) Local fault

(2) Fault on a heavily loaded tie-line

(3) Reversal of power flow on heavily loaded tie-line.

(1) Local Fault: To observe the transient stability in the event of a local fault, a 3-phase fault is applied at bus 6 (see Fig. 4.8) at t = 20 s for a period of 200 ms. The results of this tests are shown in Figs. 4.13 & 4.14.

(a) Angle stability: From Fig. 4.13, it is observed that the local fault is more severe than the fault applied at the tie-line (see Fig. 4.9), due to the proximity of the fault to the SG (or VSM). For configuration 1, the system instantaneously falls out-of-step post-fault. For configuration 2, the system is marginally stable, as the angular oscillations are not incremental post-fault. For configurations 3 and 4, the oscillation is rapidly damped due to the PSS action on the SG and VSM respectively.

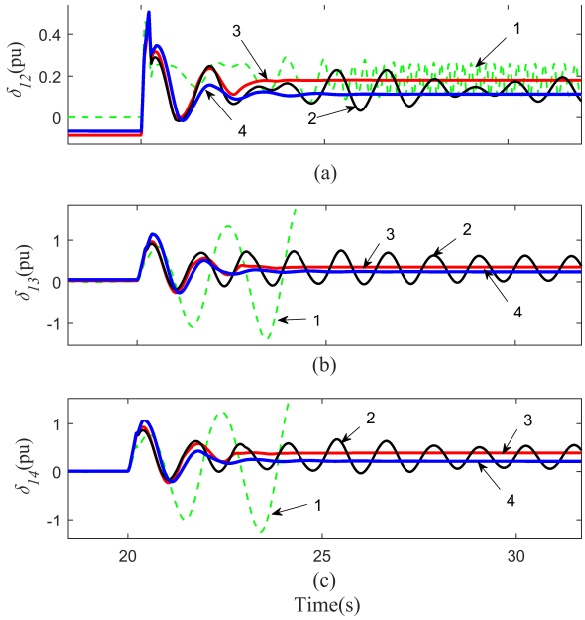

Fig. 4.13. Rotor angle: 1−4SG, 2−2SG-2VSM, 3−2SG$_{\text{pss}}$-2VSM, 4−2SG-2VSM$_{\text{pss}}$.

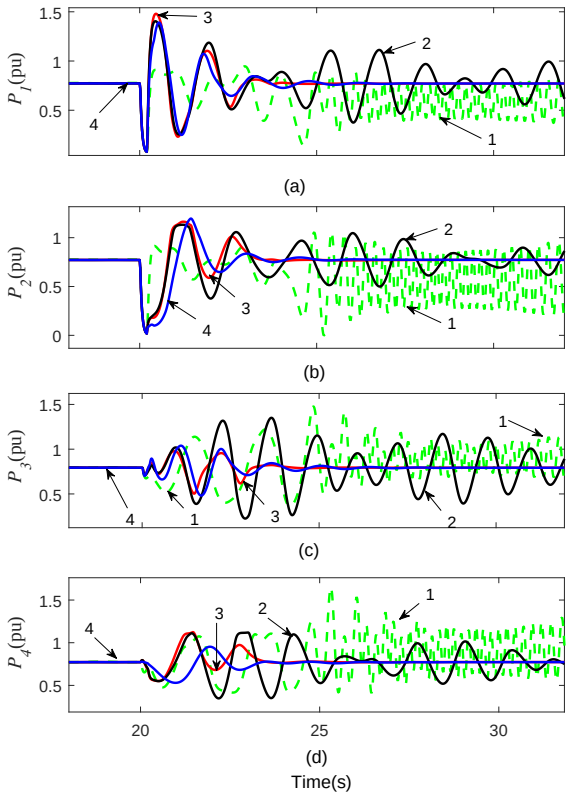

Fig. 4.14. Active Power (pu):1−4SG, 2−2SG-2VSM, 3−2SG$_{\text{pss}}$-2VSM, 4−2SG-2VSM$_{\text{pss}}$.

(b) Active Power oscillation: The power oscillation (see Fig. 4.14) for configurations 1 and 2, will trigger protective relays i.e out-of-step and pole slip protection relays [35]. For configurations 3 and 4, the oscillations are promptly damped, and the performance of the VSM_{PSS} (configuration 4) is comparable with MB-PSS (configuration 3) applied on the SG.

(2) Fault on a heavily loaded tie-line: The load at area 2 (see Fig. 4.8) is increased from 2 pu to 2.4 pu, leading to an increase in the tie-line power flow from 413 MW to 645 MW. The fault is applied at the tie-line at bus 8 (same as sub-section 4.7.1). The test results are shown in Figs. 4.15 & 4.16.

(a) Angle stability: From Fig. 4.15, it is observed that the angular oscillations are undamped and poorly damped for configurations 1 and 2 respectively. For configuration 3 and 4, the oscillations are promptly damped.

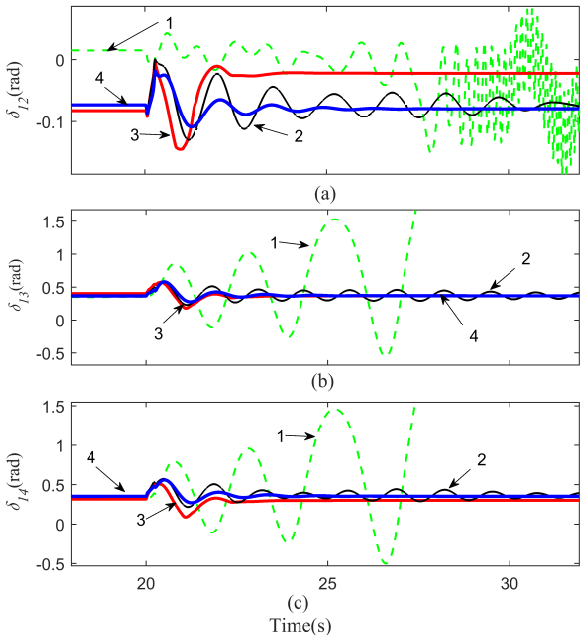

Fig. 4.15. Rotor angle: 1−4SG, 2−2SG-2VSM, 3−$2SG_{pss}$-2VSM, 4−2SG-$2VSM_{pss}$.

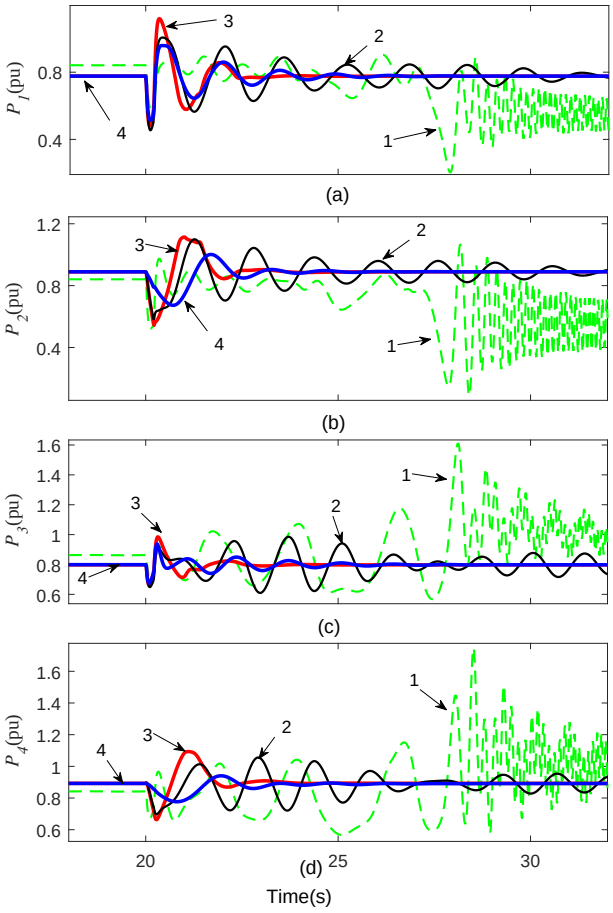

Fig. 4.16. Active Power (pu):1−4SG, 2−2SG-2VSM, 3−2SG$_{\text{pss}}$-2VSM, 4−2SG-2VSM$_{\text{pss}}$.

(b) Active Power oscillation: From Fig. 4.16, it is observed that the power oscillations are unsatisfactory for configurations 1 and 2. The result for configurations 3 and 4 illustrate that the oscillations are promptly damped post-fault, and demonstrates the efficacy of the PSS on the VSM.

3) Reversal of power flow on heavily loaded tie-line: Here, the loads at Area 1 and Area 2 are swapped (see Fig. 4.8). Thereafter, the load at Area 1 is increased from 2 pu to 2.4 pu, resulting in a net export of 645 MW power from Area 2 to Area 1. The fault is applied at the tie-line at bus 8 (same as sub-section 4.7.1). The test results are shown in Figs. 4.17 & 4.18.

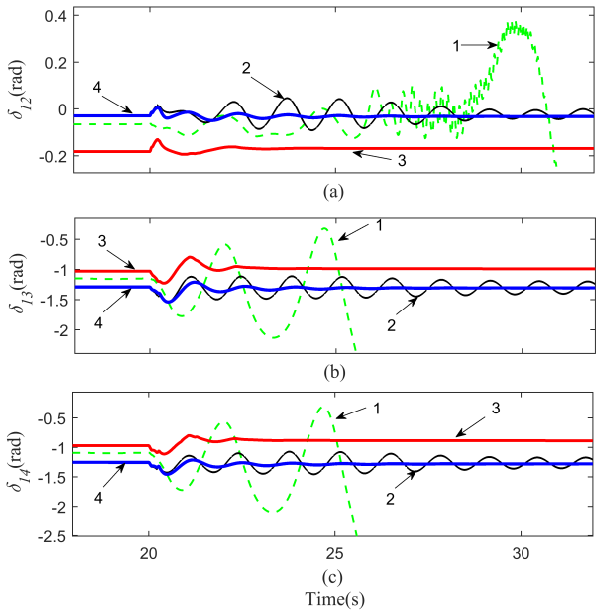

Fig. 4.17. Rotor angle: 1−4SG, 2−2SG-2VSM, 3−2SG$_{\text{pss}}$-2VSM, 4−2SG-2VSM$_{\text{pss}}$.

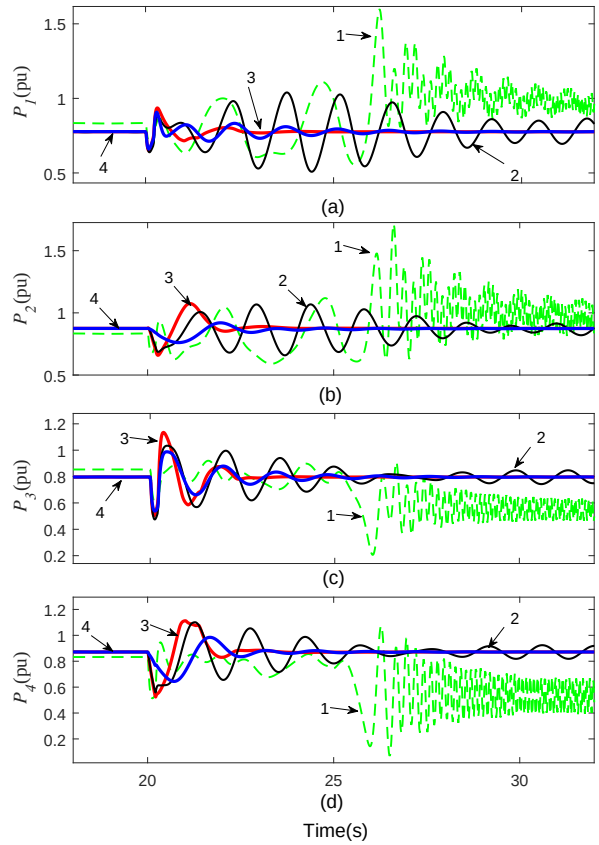

Fig. 4.18. Active Power (pu):1−4SG, 2−2SG-2VSM, 3−2SG$_{\text{pss}}$-2VSM, 4−2SG-2VSM$_{\text{pss}}$.

(a) Angle stability: The results in Figs. 4.17 & 4.18, illustrate that the system performance is unsatisfactory for both configurations 1 and 2. For configuration 3 and 4 (see Fig. 4.17), the oscillations are promptly damped. Unlike [130], the VSM_{PSS} performance is not impacted by the reversal of the tie-line power flow.

(b) Active Power oscillation: From Fig. 4.18, it is observed that the system performance is satisfactory for configurations 3 and 4.

The above tests show that the VSM_{PSS} is robust, as it provides adequate damping and satisfactory performance for various severe fault scenarios. The results also demonstrate that complex PSS designs (e.g. MB-PSS) are not required on the VSM for satisfactory operation.

4.7.3 Evaluation of an all-VSM with respect to an all-SG grid

The objective is to observe the overall performance of an all-SG system in comparison to an all-VSM system. The same fault scenario employed in sub-section 4.7.1 is applied here. Three system configurations are considered here:

- Configuration 1: four SGs no PSS (4SG).
- Configuration 2: four SGs with four MB-PSSs ($4SG_{pss}$).
- Configuration 3: four VSMs no PSS (4VSM).

Configuration 1 is same as the configuration 1 in sub-section 4.7.1), and is illustrated for the purpose of comparison and is not further discussed. The results of these tests are illustrated in Figs. 4.19–4.22, and are discussed as follows:

(a) Angle Stability: For configuration 2 (see Fig. 4.19), the rotor angle oscillation is rapidly damped post-fault due to the MB-PSSs action. For configuration 3, no oscillation is observed in the system post-fault, however there is a net angular

displacement post-fault. This is because δ is determined by PLL in the VSM, and is not required to return to pre-fault values to maintain stability, while δ is a function of the swing equation in the SG, which ensures δ returns to pre-fault values to maintain stability.

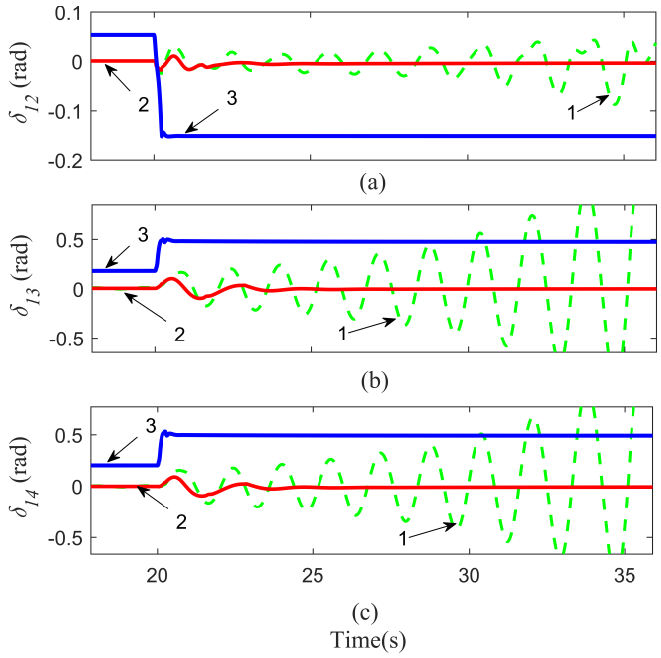

Fig. 4.19. Rotor angle: 1−4SG, 2−4SG$_{\text{pss}}$, 3−4VSM.

(b) Active Power oscillation: As shown in configuration 3 of Fig. 4.20, since no (inter-area) oscillations are generated in an all-VSM system, PSS is not required. Recovery time of P in configuration 2 and configuration 3 (see Fig. 4.20) are similar, however there is less overshoot on configuration 3, and the system recovers to pre-fault operating condition much faster.

(c) Reactive Power injection: Similar response is observed (see Fig. 4.21) on both configuration 2 and 3 with respect to the reactive power injected during fault. This shows that the VSM can adequately support the grid voltage when SGs are relinquished.

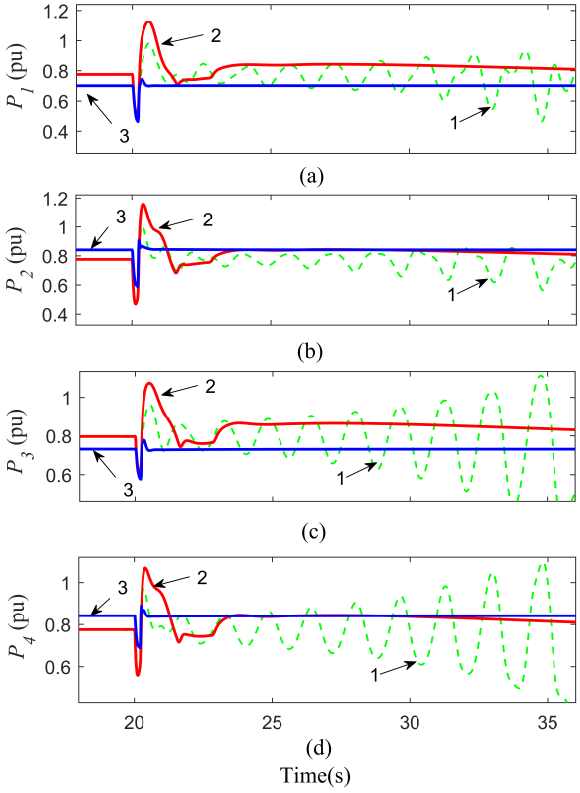

Fig. 4.20. Power (pu): 1−4SG, 2−4SG$_{\text{pss}}$, 3−4VSM.

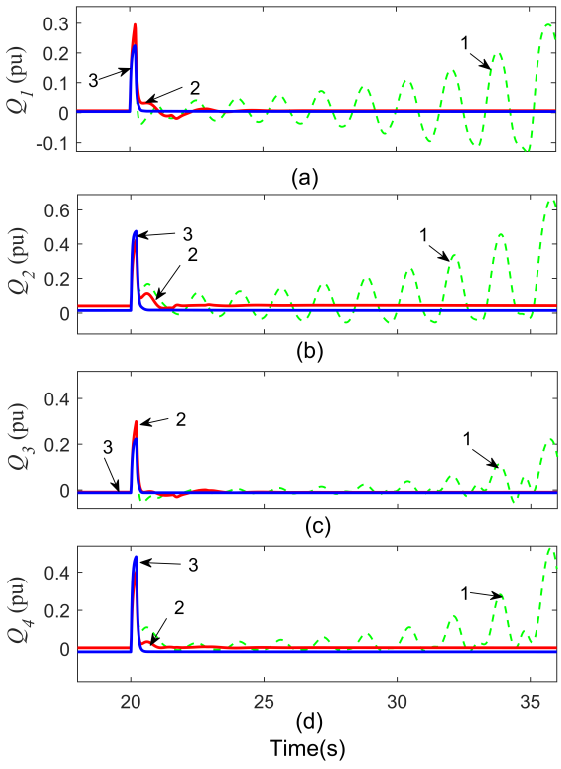

Fig. 4.21. Reactive Power (pu): 1−4SG, 2−4SG$_{\text{pss}}$, 3−4VSM.

(d) Voltage: As shown in Fig. 4.22(a), post-fault voltage regulation on configuration 3 is much better than that of configuration 2. The voltage dip during fault is similar and the differences observed may be attributed to the differences in equivalent impedance the SG and VSM present to the system, since injected Q is similar on both VSM and SG.

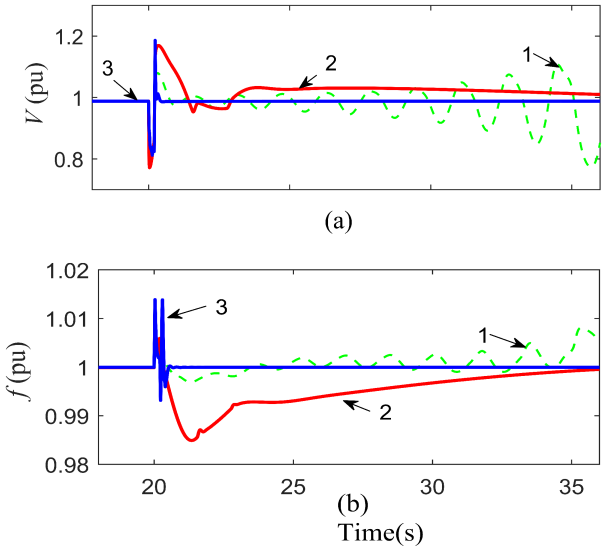

Fig. 4.22. (a) Voltage (pu): 1−4SG, 2−4SG$_{\text{pss}}$, 3−4VSM. (b) Frequency (pu): same as (a).

(e) Frequency: Frequency regulation (see Fig. 4.22(b)) seems better in configuration 3 than configuration 2, as the frequency returns to pre-fault condition much quicker. It is also observed that the employment of PSS on the SG has negative impact on the frequency nadir of the system.

From this test case, it is observed that for an all-VSM grid, inter-area oscillations do not exist, hence PSS is not required. This corroborates the observation from the small-signal analysis, which illustrates that the LFO modes for an all-VSM grid is well-damped, and the PSS is redundant.

Based on these results, one may suggest decoupling all SGs from the network using VSM-controlled AC-DC-AC converter (similar to the PMSG based VSM structure

proposed in chapter 3). This will eliminate LFOs, smoothen transition to a sustainable all-VSM system and enhance system stability.

The key contributions in this chapter are:

(I) Developed a detailed two-machine test-bed which enables accurate evaluation of the LFO modes from the participating generators.

(II) Comprehensive analysis on the impact of replacing SG with VSM and VSM-PSS (VSM_{PSS}).

(III) Comprehensive analysis of the LFO modes which exists in an all-VSM power system.

(IV) Evaluation of the role of PSS in an all-VSM power system.

4.8 Conclusion of Chapter 4

This chapter investigated the impact of VSM based RESs on the LFOs in the power system. This was achieved using a detailed two-machine state space model to comprehensively analyze the small-signal stability, while the transient stability was investigated in an IEEE bench mark dedicated for inter-area oscillations. From the small-signal stability analysis, it was observed that when VSM replaces SG, an additional LFO is added to the system. This LFO is sufficiently damped and does not adversely impact the system stability. The PLL and virtual governor from the VSM play a major role on the LFO interaction with the SG. The net impact of the SG replacement with VSM is an improved damping of the LFO modes. However, the VSM must be integrated with PSS for satisfactory performance when interconnected with SGs. The robustness of the VSM_{PSS} was validated for different test scenarios. For an all-VSM system, the LFO modes are well damped and inter-area oscillations do not exist, which makes using a PSS redundant. Thus, to eliminate LFOs without

the need for a PSS, it is pertinent to decouple the SGs from the grid using VSMs. The results of the transient analysis closely match the small-signal analysis, which shows that the two-machine test-bed accurately describes the dynamics of the participating generators and can be employed for investigating the LFOs in VSMs with diverse dynamics.

5. CONCLUSION AND FUTURE WORK

5.1 Conclusion

Energy sustainability, independence and socioeconomic factors are key drivers for the paradigm shift from the conventional fossil-fuel based power system to a decentralized system driven by RESs. The research work in this Ph.D. thesis, was focused on the design and stability analysis of grid-friendly control schemes which facilitate the large-scale integration of RESs, thus enabling the smooth transition to a zero-carbon power system.

A background study of the issues hindering the large-scale integration of RESs was discussed in chapter 1. It was highlighted that the conventional control topologies for RESs do not provide support for the grid during contingencies and are prone to transient stability. Moreover, the National Grid has reported operational and control challenges associated with the increasing penetration of RESs. Hence, the concept of VSMs, which mimic the desirable characteristics of the SG, have been proposed as a grid-friendly approach to integrate RESs into the grid. Owing to the superior performance of VSMs over the conventional RESs, there has been substantial research effort by academics and industry experts to design VSM topologies which seamlessly integrate with the grid.

Chapter 2 of this thesis presented a comprehensive and critical review of the VSM topologies proposed in literature. A comprehensive description of the operation and salient characteristics of each VSM topology was discussed. It was observed that most of the topologies proposed in literature do not guarantee seamless transition from grid-connected to islanded mode of operation (and vice-versa). Some topolo-

gies require a change of operating point prior to grid connection, while some require switching control paradigms between the two modes. Further, some topologies do not employ any frequency estimation/detection circuit, thereby necessitating further complications (e.g. communications and/or integral reseting) at the time of grid reconnection. It was concluded that most of the VSMs proposed in literature require further modifications in order to meet the grid requirements. Hence, a novel VSM topology which bridges the gaps identified in the previous topologies was proposed in this thesis.

In chapter 3, a novel PMSG based VSM topology which enables seamless performance in all operating modes was presented. A salient feature of the VSM topology is that it employs a single control paradigm in all operating modes. The VSM enables MPPT in grid-connected operation (assuming strong grid), LFPG in weak grid and FRT during fault. A small-signal stability analysis of the VSM was conducted to determine the impact of the controllers on the dominant modes of the system. Thereafter, the transient stability of the VSM was analyzed using a nonlinear model. Based on this analysis, design guidelines and operational limits of the VSM were established. It was highlighted that a low PLL bandwidth is required for a desirable performance and stable operation of the VSM. It was also observed that a fast virtual AVR and a relatively slow and well-damped virtual governor are essential to maintain stability and ensure optimal dynamic performance.

The studies in chapter 4 was focused on the impact of VSMs on the power systems LFOs. It was highlighted that some of the previous studies neglected the transmission network dynamics, while some neglected the voltage and current controllers. This impacted the accuracy of the previous studies, and led to conflicting reports on the net impact of VSMs on the power systems LFOs. In light of the gaps in the previous works, an accurate and comprehensive approach to analyse the impact of VSMs on the power systems LFOs was presented. A detailed two-machine test-bed was developed to analyze the LFOs which exists when VSMs replace SGs. Further,

this study analyzed the LFO modes which exists in an all-VSM grid, and the role of PSSs in the system. It was demonstrated that the net impact of the SG replacement with VSM is an improved damping of the LFO modes. However, the VSM must be integrated with PSS for satisfactory performance when interconnected with SGs. For an all-VSM system, PSS is not required since the LFO modes are well damped. The result of the small-signal analysis were validated using the IEEE benchmark two-area four-machine system. It was concluded that in order to eliminate the power systems LFOs without the need for a PSS, it is pertinent to decouple the SGs from the grid using VSMs.

5.2 Potential Future Work

This thesis proposed a novel VSM algorithm and provided a comprehensive analysis of the system in several scenarios. The following imminent recommendations are proposed at this stage:

(1) Laboratory test: The VSM proposed in this thesis has been extensively evaluated via small-signal stability analysis and time-domain simulations. To facilitate rapid prototyping of the proposed algorithm, a laboratory test must be done. Hardware in the loop simulators (e.g. OPAL-RT, dSpace and Speedgoat) can be employed to accurately validate the performance of the VSM algorithm in real-time. This facilitates early detection of anomalies in the algorithm, prior to deployment in real systems. It is noted that the British National Grid is actively seeking "new stability support products" which will facilitate the transition to a zero-carbon power system. Hence, rapid prototyping of the proposed algorithm will accelerate the readiness of the algorithm for grid-scale application.

(2) PLL-less VSM: An integral component of the proposed VSM is the PLL, which is required for frequency estimation and grid synchronization. Although

it was demonstrated that a well designed PLL has minimal impact on the VSM stability, an open area for further research, is the possibility of eliminating the PLL and replacing it with a virtual PLL. The envisaged structure, should be such that it simplifies the VSM algorithm, and improves the stability. It is noted that although some topologies in literature already employ PLL-less/self-synchronizing topologies, these algorithms do not guarantee seamless transition from grid-connected to islanded modes (and vice-versa).

(3) Multi-VSM analysis: The research work in this thesis was focused on the study and stability analysis of the proposed VSM. However, since several VSM topologies have been proposed in literature, microgrids may consist of several variant topologies. Hence, it is pertinent to evaluate the operation and stability of microgrids consisting of several VSM topologies. Furthermore, it will be essential to verify that the interaction of variant VSMs does not create new oscillatory modes, which impact the power system stability.

(4) Vehicle to grid (V2G): In line with the directives of the British government, electric vehicles (EVs) will rapidly replace fossil-fuelled vehicles in the next decades. Thus, a potential opportunity arises for EVs to support the grid via V2G services. For future research, the proposed VSM can be modified for application in smart EV charging systems. By so doing, a fleet of EVs can be exploited to provide substantial support for the grid during contingencies.

REFERENCES

[1] A. Ipakchi and F. Albuyeh, "Grid of the future," *IEEE Power and Energy Magazine*, vol. 7, no. 2, pp. 52–62, 2009. DOI: 10.1109/MPE.2008.931384.

[2] A. Shoaib and S. Ariaratnam, "A study of socioeconomic impacts of renewable energy projects in afghanistan," *Procedia Engineering*, vol. 145, pp. 995–1003, 2016, ICSDEC 2016 – Integrating Data Science, Construction and Sustainability, ISSN: 1877-7058. DOI: https://doi.org/10.1016/j.proeng.2016.04.129.

[3] P. Kundur, N. Balu, and M. Lauby, *Power System Stability and Control*. McGraw-Hill Education, 1994.

[4] G. Rogers, *Power system oscillations*. Springer Science & Business Media, 2012.

[5] C. Taylor, N. Balu, and D. Maratukulam, *Power System Voltage Stability*. McGraw-Hill Education, 1994.

[6] P. M. Anderson and A. A. Fouad, *Power System Control and Stability*. IEEE, 2003.

[7] R. Smith, *System Operability Framework*. National Grid, 2016, [Accessed on 01-Oct-2020]. [Online]. Available: https://www.nationalgrid.com/sites/default/files/documents/8589937803-SOF%202016%20-%20Full%20Interactive%20Document.pdf.

[8] ENTSO-E, *High Penetration of Power Electronic Interfaced Power Sources and the Potential Contribution of Grid Forming Converters*. Avenue de Corten-

bergh 100, 1000 Brussels, Belgium, Jan. 2020, [Accessed on 24-Jan-2021]. [Online]. Available: https://euagenda.eu/upload/publications/untitled-292051-ea.pdf.

[9] D. Lew, D. Bartlett, A. Groom, P. Jorgensen, J. O'Sullivan, R. Quint, B. Rew, B. Rockwell, S. Sharma, and D. Stenclik, "Secrets of successful integration: Operating experience with high levels of variable, inverter-based generation," *IEEE Power and Energy Magazine*, vol. 17, no. 6, 2019. DOI: 10.1109/MPE.2019.2930855.

[10] C. Chunyan, M. Xiaolei, Y. Wenjia, Z. Zhaozhi, and Y. Qiang, "Status and prospect of new energy: A review," in *2012 Third International Conference on Digital Manufacturing Automation*, 2012, pp. 796–800.

[11] F. Milano, F. Dörfler, G. Hug, D. J. Hill, and G. Verbič, "Foundations and challenges of low-inertia systems (invited paper)," in *2018 Power Systems Computation Conference (PSCC)*, 2018, pp. 1–25. DOI: 10.23919/PSCC.2018.8450880.

[12] National Grid, *Operability Strategy Report*. National Grid Warwick Technology Park, Gallows Hill, Warwick, UK., Dec. 2019, [Accessed on 11-Nov-2020]. [Online]. Available: https://www.nationalgrideso.com/document/159726/download.

[13] M. Fazeli, P. M. Holland, and M. Baruwa, ""Grid"-less power systems: A vision for future structure of power networks," *IEEE Access*, vol. 8, 2020. DOI: 10.1109/ACCESS.2020.3020455.

[14] O. Jogunola, W. Wang, and B. Adebisi, "Prosumers matching and least-cost energy path optimisation for peer-to-peer energy trading," *IEEE Access*, vol. 8, pp. 95 266–95 277, 2020. DOI: 10.1109/ACCESS.2020.2996309.

[15] Q. Zhong, "Virtual synchronous machines: A unified interface for grid integration," *IEEE Power Electronics Magazine*, vol. 3, no. 4, pp. 18–27, 2016. DOI: 10.1109/MPEL.2016.2614906.

[16] IRENA (2018), *Global Energy Transformation: A roadmap to 2050*. International Renewable Energy Agency, Abu Dhabi, Jun. 2018, [Accessed on 24-Jan-2021]. [Online]. Available: https://www.irena.org/-/media/Files/IRENA/Agency/Publication/2018/Apr/IRENA_Report_GET_2018.pdf.

[17] National Grid, *Towards 2030: An Electricity System Operator for Great Britain's Energy Future*. National Grid Warwick Technology Park, Gallows Hill, Warwick, UK., Apr. 2019, [Accessed on 11-Nov-2020]. [Online]. Available: https://www.nationalgrideso.com/document/161996/download.

[18] National Grid, *Future Energy Scenarios*. National Grid Warwick Technology Park, Gallows Hill, Warwick, UK., Jul. 2020, [Accessed on 16-Sep-2020]. [Online]. Available: https://www.nationalgrideso.com/document/174541/download.

[19] R. H. Lasseter and P. Paigi, "Microgrid: A conceptual solution," in *2004 IEEE 35th Annual Power Electronics Specialists Conference (IEEE Cat. No.04CH37551)*, vol. 6, 2004, 4285–4290 Vol.6. DOI: 10.1109/PESC.2004.1354758.

[20] "IEEE Guide for Design, Operation, and Integration of Distributed Resource Island Systems with Electric Power Systems," *IEEE Std 1547.4-2011*, pp. 1–54, 2011. DOI: 10.1109/IEEESTD.2011.5960751.

[21] M. Farrokhabadi et al., "Microgrid stability definitions, analysis, and examples," *IEEE Transactions on Power Systems*, vol. 35, no. 1, pp. 13–29, 2020. DOI: 10.1109/TPWRS.2019.2925703.

[22] Q. Jiang, M. Xue, and G. Geng, "Energy management of microgrid in grid-connected and stand-alone modes," *IEEE Transactions on Power Systems*, vol. 28, no. 3, pp. 3380–3389, 2013. DOI: 10.1109/TPWRS.2013.2244104.

[23] National Grid, *Black Start from Non-Traditional Generation Technologies*. National Grid Warwick Technology Park, Gallows Hill, Warwick, UK., Jun. 2019, [Accessed on 11-Nov-2020]. [Online]. Available: https://www.nationalgrideso.com/document/148201/download.

[24] B. Kroposki, B. Johnson, Y. Zhang, V. Gevorgian, P. Denholm, B. Hodge, and B. Hannegan, "Achieving a 100% renewable grid: Operating electric power systems with extremely high levels of variable renewable energy," *IEEE Power and Energy Magazine*, vol. 15, no. 2, pp. 61–73, 2017. DOI: 10.1109/MPE.2016.2637122.

[25] M. Fazeli, G. M. Asher, C. Klumpner, L. Yao, and M. Bazargan, "Novel Integration of Wind Generator-Energy Storage Systems Within Microgrids," *IEEE Transactions on Smart Grid*, vol. 3, no. 2, pp. 728–737, 2012. DOI: 10.1109/TSG.2012.2185073.

[26] M. Fazeli, G. M. Asher, C. Klumpner, and L. Yao, "Novel Integration of DFIG-Based Wind Generators Within Microgrids," *IEEE Transactions on Energy Conversion*, vol. 26, no. 3, pp. 840–850, 2011. DOI: 10.1109/TEC.2011.2146253.

[27] A. M. Egwebe, M. Fazeli, P. Igic, and P. M. Holland, "Implementation and stability study of dynamic droop in islanded microgrids," *IEEE Transactions on Energy Conversion*, vol. 31, no. 3, pp. 821–832, 2016. DOI: 10.1109/TEC.2016.2540922.

[28] L. Huang, H. Xin, Z. Wang, L. Zhang, K. Wu, and J. Hu, "Transient stability analysis and control design of droop-controlled voltage source converters considering current limitation," *IEEE Transactions on Smart Grid*, vol. 10, no. 1, pp. 578–591, 2019. DOI: 10.1109/TSG.2017.2749259.

[29] R. Belkacemi, S. Zarrabian, A. Babalola, and R. Craven, "Experimental transient stability analysis of microgrid systems: Lessons learned," in *2015 IEEE*

Power Energy Society General Meeting, 2015, pp. 1–5. DOI: 10.1109/PESGM.2015.7286637.

[30] J. Matevosyan, S. Sharma, S. Huang, D. Woodfin, K. Ragsdale, S. Moorty, P. Wattles, and W. Li, "Proposed future ancillary services in electric reliability council of texas," in *2015 IEEE Eindhoven PowerTech*, 2015, pp. 1–6. DOI: 10.1109/PTC.2015.7232743.

[31] Australian Energy Market Operator, *BLACK SYSTEM SOUTH AUSTRALIA 28 SEPTEMBER 2016–FINAL REPORT*. Australian Energy Market Operator, Mar. 2017, [Accessed on 12-Nov-2020]. [Online]. Available: https://www.aemo.com.au/-/media/Files/Electricity/NEM/Market_Notices_and_Events/Power_System_Incident_Reports/2017/Integrated-Final-Report-SA-Black-System-28-September-2016.pdf.

[32] P. Kundur, J. Paserba, V. Ajjarapu, G. Andersson, A. Bose, C. Canizares, N. Hatziargyriou, D. Hill, A. Stankovic, C. Taylor, T. Van Cutsem, and V. Vittal, "Definition and classification of power system stability IEEE/CIGRE joint task force on stability terms and definitions," *IEEE Transactions on Power Systems*, vol. 19, no. 3, pp. 1387–1401, 2004.

[33] M. Garmroodi, D. J. Hill, G. Verbič, and J. Ma, "Impact of tie-line power on inter-area modes with increased penetration of wind power," *IEEE Transactions on Power Systems*, vol. 31, no. 4, pp. 3051–3059, Jul. 2016.

[34] Q. Zhong and G. Weiss, "Synchronverters: Inverters that mimic synchronous generators," *IEEE Transactions on Industrial Electronics*, vol. 58, no. 4, 1259–1267, Apr. 2011. DOI: 10.1109/TIE.2010.2048839.

[35] J. Machowski, Z. Lubosny, J. Bialek, and J. Bumby, *Power System Dynamics: Stability and Control*. Wiley, 2020.

[36] W. Du, J. Bi, and H. F. Wang, "Small-signal angular stability of power system as affected by grid-connected variable speed wind generators- a survey of recent representative works," *CSEE Journal of Power and Energy Systems*, vol. 3, no. 3, pp. 223–231, Sep. 2017.

[37] National Grid, *THE GRID CODE*, 39. National Grid, Feb. 2020, [Accessed on 19-Feb-2020]. [Online]. Available: https://www.nationalgrideso.com/document/162271/download.

[38] M. Cheng, J. Wu, S. J. Galsworthy, C. E. Ugalde-Loo, N. Gargov, W. W. Hung, and N. Jenkins, "Power system frequency response from the control of bitumen tanks," *IEEE Transactions on Power Systems*, vol. 31, no. 3, pp. 1769–1778, 2016. DOI: 10.1109/TPWRS.2015.2440336.

[39] R. Smith, *System Operability Framework*. National Grid, 2015, [Accessed on 01-Oct-2020]. [Online]. Available: https://www.nationalgrideso.com/document/63461/download.

[40] National Grid, *Voltage and Frequency Dependency*. National Grid Warwick Technology Park, Gallows Hill, Warwick, UK., 2018, [Accessed on 27-Nov-2020]. [Online]. Available: https://www.nationalgrideso.com/sites/eso/files/documents/SOF%20Report%20-%20Frequency%20and%20Voltage%20assessment.pdf.

[41] National Grid, *Operating a Low Inertia System*. National Grid Warwick Technology Park, Gallows Hill, Warwick, UK., Feb. 2020, [Accessed on 12-Nov-2020]. [Online]. Available: https://www.nationalgrideso.com/document/164586/download.

[42] National Grid, *Impact of declining short circuit levels*. National Grid Warwick Technology Park, Gallows Hill, Warwick, UK., Dec. 2018, [Accessed on 12-Nov-2020]. [Online]. Available: https://www.nationalgrideso.com/document/135561/download.

[43] M. Yu, A. Dysko, C. Booth, A. Roscoe, J. Zhu, and H. Urdal, "Investigations of the constraints relating to penetration of non-synchronous generation (NSG) in future power systems," in *Sixth Protection, Automation and Control World Conference (PAC World 2015)*, 2015.

[44] European Commission, *Road Map 2050: A PRACTICAL GUIDE TO A PROSPEROUS, LOW-CARBON EUROPE*. Publications Office of the European Union, Apr. 2010, [Accessed on 24-Jan-2021]. [Online]. Available: https://www.roadmap2050.eu/attachments/files/Volume1_fullreport_PressPack.pdf.

[45] National Grid, *The potential operability benefits of Virtual Synchronous Machines and related technologies*. National Grid Warwick Technology Park, Gallows Hill, Warwick, UK., Apr. 2020, [Accessed on 11-Nov-2020]. [Online]. Available: https://www.nationalgrideso.com/document/168376/download.

[46] Y. Chen, R. Hesse, D. Turschner, and H. Beck, "Improving the grid power quality using virtual synchronous machines," in *2011 International Conference on Power Engineering, Energy and Electrical Drives*, May 2011, pp. 1–6. DOI: 10.1109/PowerEng.2011.6036498.

[47] National Grid, *Voltage and Frequency Dependency*. National Grid Warwick Technology Park, Gallows Hill, Warwick, UK., 2018, [Accessed on 27-Nov-2020]. [Online]. Available: https://www.nationalgrideso.com/sites/eso/files/documents/SOF%20Report%20-%20Frequency%20and%20Voltage%20assessment.pdf.

[48] H. Beck and R. Hesse, "Virtual synchronous machine," in *2007 9th International Conference on Electrical Power Quality and Utilisation*, 2007, pp. 1–6. DOI: 10.1109/EPQU.2007.4424220.

[49] H. Beck and R. Hesse, "Comparison of methods for implementing virtual synchronous machine on inverters," in *2012 International Conference on Renewable Energies and Power Quality (ICREPQ'12)*, 2012, pp. 1–6.

[50] R. Hesse, D. Turschner, and H.-P. Beck, "Micro grid stabilization using the virtual synchronous machine (VISMA)," *Renewable energy and power quality journal*, vol. 1, pp. 676–681, 2009.

[51] Y. Chen, R. Hesse, D. Turschner, and H.-P. Beck, "Dynamic properties of the virtual synchronous machine (visma)," *Renewable energy and power quality journal*, pp. 755–759, 2011.

[52] Q.-C. Zhong, P.-L. Nguyen, Z. Ma, and W. Sheng, "Self-synchronized synchronverters: Inverters without a dedicated synchronization unit," *IEEE Transactions on Power Electronics*, vol. 29, pp. 617–630, 2014. DOI: 10.1109/TPEL.2013.2258684.

[53] S. Dong, J. Jiang, and Y. C. Chen, "Analysis of synchronverter self-synchronization dynamics to facilitate parameter tuning," *IEEE Transactions on Energy Conversion*, vol. 35, no. 1, pp. 11–23, 2020. DOI: 10.1109/TEC.2019.2945958.

[54] S. Dong and Y. C. Chen, "Adjusting synchronverter dynamic response speed via damping correction loop," *IEEE Transactions on Energy Conversion*, vol. 32, no. 2, pp. 608–619, 2017. DOI: 10.1109/TEC.2016.2645450.

[55] Z. Shuai, W. Huang, C. Shen, J. Ge, and Z. J. Shen, "Characteristics and restraining method of fast transient inrush fault currents in synchronverters," *IEEE Transactions on Industrial Electronics*, vol. 64, no. 9, pp. 7487–7497, 2017. DOI: 10.1109/TIE.2017.2652362.

[56] Z. Shuai, Y. Hu, Y. Peng, C. Tu, and Z. J. Shen, "Dynamic stability analysis of synchronverter-dominated microgrid based on bifurcation theory," *IEEE Transactions on Industrial Electronics*, vol. 64, no. 9, pp. 7467–7477, 2017. DOI: 10.1109/TIE.2017.2652387.

[57] Q. Zhong, G. C. Konstantopoulos, B. Ren, and M. Krstic, "Improved synchronverters with bounded frequency and voltage for smart grid integration," *IEEE Transactions on Smart Grid*, vol. 9, no. 2, pp. 786–796, 2018. DOI: 10.1109/TSG.2016.2565663.

[58] P. Piya and M. Karimi-Ghartemani, "A stability analysis and efficiency improvement of synchronverter," in *2016 IEEE Applied Power Electronics Conference and Exposition (APEC)*, 2016, pp. 3165–3171. DOI: 10.1109/APEC.2016.7468317.

[59] R. Rosso, S. Engelken, and M. Liserre, "Robust stability analysis of synchronverters operating in parallel," *IEEE Transactions on Power Electronics*, vol. 34, no. 11, pp. 11 309–11 319, 2019. DOI: 10.1109/TPEL.2019.2896707.

[60] V. Natarajan and G. Weiss, "Synchronverters with better stability due to virtual inductors, virtual capacitors, and anti-windup," *IEEE Transactions on Industrial Electronics*, vol. 64, no. 7, pp. 5994–6004, 2017. DOI: 10.1109/TIE.2017.2674611.

[61] R. Aouini, B. Marinescu, K. Ben Kilani, and M. Elleuch, "Synchronverter-Based Emulation and Control of HVDC Transmission," *IEEE Transactions on Power Systems*, vol. 31, no. 1, pp. 278–286, 2016. DOI: 10.1109/TPWRS.2015.2389822.

[62] U. Tamrakar, D. Shrestha, M. Maharjan, B. P. Bhattarai, T. M. Hansen, and R. Tonkoski, "Virtual inertia: Current trends and future directions," *Applied Sciences*, vol. 7, no. 7, 2017, ISSN: 2076-3417. DOI: 10.3390/app7070654.

[63] K. Sakimoto, Y. Miura, and T. Ise, "Stabilization of a power system with a distributed generator by a virtual synchronous generator function," in *8th International Conference on Power Electronics - ECCE Asia*, 2011, pp. 1498–1505. DOI: 10.1109/ICPE.2011.5944492.

[64] H. Bevrani, T. Ise, and Y. Miura, "Virtual synchronous generators: A survey and new perspectives," *International Journal of Electrical Power and Energy Systems*, vol. 54, pp. 244–254, 2014, ISSN: 0142-0615. DOI: https://doi.org/10.1016/j.ijepes.2013.07.009.

[65] K. M. Cheema, "A comprehensive review of virtual synchronous generator," *International Journal of Electrical Power and Energy Systems*, vol. 120, p. 106 006, 2020, ISSN: 0142-0615. DOI: https://doi.org/10.1016/j.ijepes.2020.106006.

[66] A. Yazdani and R. Iravani, *Voltage-Sourced Converters in Power Systems:Modeling, Control, and Applications*. IEEE, 2010.

[67] J. Liu, Y. Miura, H. Bevrani, and T. Ise, "Enhanced virtual synchronous generator control for parallel inverters in microgrids," *IEEE Transactions on Smart Grid*, vol. 8, no. 5, pp. 2268–2277, Sep. 2017, ISSN: 1949-3053. DOI: 10.1109/TSG.2016.2521405.

[68] T. Shintai, Y. Miura, and T. Ise, "Reactive power control for load sharing with virtual synchronous generator control," in *Proceedings of The 7th International Power Electronics and Motion Control Conference*, vol. 2, 2012, pp. 846–853. DOI: 10.1109/IPEMC.2012.6258956.

[69] J. Alipoor, Y. Miura, and T. Ise, "Stability assessment and optimization methods for microgrid with multiple vsg units," *IEEE Transactions on Smart Grid*, vol. 9, no. 2, pp. 1462–1471, 2018. DOI: 10.1109/TSG.2016.2592508.

[70] J. Alipoor, Y. Miura, and T. Ise, "Power system stabilization using virtual synchronous generator with alternating moment of inertia," *IEEE Journal of Emerging and Selected Topics in Power Electronics*, vol. 3, no. 2, pp. 451–458, Jun. 2015. DOI: 10.1109/JESTPE.2014.2362530.

[71] J. Alipoor and Y. Miura and T. Ise, "Voltage sag ride-through performance of virtual synchronous generator," in *2014 International Power Electronics Conference (IPEC-Hiroshima 2014 - ECCE ASIA)*, 2014, pp. 3298–3305. DOI: 10.1109/IPEC.2014.6870160.

[72] M. Yu, A. J. Roscoe, C. D. Booth, A. Dysko, R. Ierna, J. Zhu, N. Grid, and H. Urdal, "Use of an inertia-less virtual synchronous machine within future power networks with high penetrations of converters," in *2016 Power Systems Computation Conference*, Jun. 2016, pp. 1–7. DOI: 10.1109/PSCC.2016.7540926.

[73] L. R. Castillo and A. Roscoe, "Experimental validation of a novel inertia-less vsm algorithm," in *2018 IEEE Power Energy Society Innovative Smart Grid Technologies Conference (ISGT)*, 2018, pp. 1–5. DOI: 10.1109/ISGT.2018.8403384.

[74] A. J Roscoe, M. Yu, A. Dyśko, C. Booth, R. Ierna, J. Zhu, and H. Urdal, "A vsm (virtual synchronous machine) convertor control model suitable for rms studies for resolving system operator / owner challenges," *15th Wind Integration Workshop*, Nov. 2016. [Online]. Available: http://strathprints.strath.ac.uk/58053/.

[75] K. S. Yuko Hirase Kazuhiro Abe and Y. Shindo, "A grid-connected inverter with virtual synchronous generator model of algebraic type," *IEEJ Transactions on Power and Energy*, vol. 132, pp. 371–380, 4 2012. DOI: https://doi.org/10.1541/ieejpes.132.371.

[76] L. Zhang, L. Harnefors, and H. Nee, "Power-Synchronization Control of Grid-Connected Voltage-Source Converters," *IEEE Transactions on Power Systems*, vol. 25, no. 2, pp. 809–820, 2010. DOI: 10.1109/TPWRS.2009.2032231.

[77] M. Ashabani, Y. A. R. I. Mohamed, M. Mirsalim, and M. Aghashabani, "Multivariable droop control of synchronous current converters in weak grids/microgrids

with decoupled dq-axes currents," *IEEE Transactions on Smart Grid*, vol. 6, no. 4, pp. 1610–1620, 2015. DOI: 10.1109/TSG.2015.2392373.

[78] L. Zhang, L. Harnefors, and H. Nee, "Interconnection of Two Very Weak AC Systems by VSC-HVDC Links Using Power-Synchronization Control," *IEEE Transactions on Power Systems*, vol. 26, no. 1, pp. 344–355, 2011. DOI: 10.1109/TPWRS.2010.2047875.

[79] L. Zhang, L. Harnefor, and H. Nee, "Modeling and Control of VSC-HVDC Links Connected to Island Systems," *IEEE Transactions on Power Systems*, vol. 26, no. 2, pp. 783–793, 2011. DOI: 10.1109/TPWRS.2010.2070085.

[80] W. Zhang, A. M. Cantarellas, J. Rocabert, A. Luna, and P. Rodriguez, "Synchronous power controller with flexible droop characteristics for renewable power generation systems," *IEEE Transactions on Sustainable Energy*, vol. 7, no. 4, pp. 1572–1582, 2016. DOI: 10.1109/TSTE.2016.2565059.

[81] W. Zhang, D. Remon, and P. Rodriguez, "Frequency support characteristics of grid-interactive power converters based on the synchronous power controller," *IET Renewable Power Generation*, vol. 11, no. 4, pp. 470–479, 2017. DOI: 10.1049/iet-rpg.2016.0557.

[82] S. S. Thale and V. Agarwal, "Controller area network assisted grid synchronization of a microgrid with renewable energy sources and storage," *IEEE Transactions on Smart Grid*, vol. 7, no. 3, pp. 1442–1452, 2016. DOI: 10.1109/TSG.2015.2453157.

[83] D. Shi, Y. Luo, and R. K. Sharma, "Active synchronization control for microgrid reconnection after islanding," in *IEEE PES Innovative Smart Grid Technologies, Europe*, 2014, pp. 1–6. DOI: 10.1109/ISGTEurope.2014.7028802.

[84] C. Verdugo, J. I. Candela, and P. Rodriguez, "Re-synchronization strategy for the synchronous power controller in hvdc systems," in *2017 IEEE Energy Conversion Congress and Exposition (ECCE)*, 2017, pp. 5186–5191. DOI: 10.1109/ECCE.2017.8096872.

[85] M. Ashabani and J. Jung, "Synchronous voltage controllers: Voltage-based emulation of synchronous machines for the integration of renewable energy sources," *IEEE Access*, vol. 8, pp. 49 497–49 508, 2020. DOI: 10.1109/ACCESS.2020.2976892.

[86] M. Fazeli and P. Holland, "Universal and seamless control of distributed resources-energy storage for all operational scenarios of microgrids," *IEEE Transactions on Energy Conversion*, vol. 32, no. 3, pp. 963–973, Sep. 2017. DOI: 10.1109/TEC.2017.2689505.

[87] M. Ashabani, F. D. Freijedo, S. Golestan, and J. M. Guerrero, "Inducverters: Pll-less converters with auto-synchronization and emulated inertia capability," *IEEE Transactions on Smart Grid*, vol. 7, no. 3, pp. 1660–1674, 2016. DOI: 10.1109/TSG.2015.2468600.

[88] E. Hossain, R. Perez, A. Nasiri, and S. Padmanaban, "A comprehensive review on constant power loads compensation techniques," *IEEE Access*, vol. 6, pp. 33 285–33 305, 2018. DOI: 10.1109/ACCESS.2018.2849065.

[89] M. P. N. van Wesenbeeck, S. W. H. de Haan, P. Varela, and K. Visscher, "Grid-tied converter with virtual kinetic storage," in *2009 IEEE Bucharest PowerTech*, 2009, pp. 1–7. DOI: 10.1109/PTC.2009.5282048.

[90] J. Driesen and K. Visscher, "Virtual synchronous generators," in *2008 IEEE Power and Energy Society General Meeting - Conversion and Delivery of Electrical Energy in the 21st Century*, 2008, pp. 1–3. DOI: 10.1109/PES.2008.4596800.

[91] K. Visscher and S. W. H. De Haan, "Virtual synchronous machines (VSG's) for frequency stabilisation in future grids with a significant share of decentralized generation," in *CIRED Seminar 2008: SmartGrids for Distribution*, 2008, pp. 1–4.

[92] V. Karapanos, S. de Haan, and K. Zwetsloot, "Real time simulation of a power system with vsg hardware in the loop," in *IECON 2011 - 37th Annual Conference of the IEEE Industrial Electronics Society*, 2011, pp. 3748–3754. DOI: 10.1109/IECON.2011.6119919.

[93] V. Van Thong, A. Woyte, M. Albu, M. Van Hest, J. Bozelie, J. Diaz, T. Loix, D. Stanculescu, and K. Visscher, "Virtual synchronous generator: Laboratory scale results and field demonstration," in *2009 IEEE Bucharest PowerTech*, 2009, pp. 1–6. DOI: 10.1109/PTC.2009.5281790.

[94] V. Karapanos, Z. Yuan, S. de Haan, and K. Visscher, "A control algorithm for the coordination of multiple virtual sychnronous generator units," English, in *Proceedings of the IEEE Powertech Conference, 2011*, A. Apostolov, Ed., IEEE Society, 2011, pp. 1–7.

[95] National Grid, *Stability pathfinder RFI – Technical performanceand assessment criteria (Attachment 1)*. National Grid Warwick Technology Park, Gallows Hill, Warwick, UK., 2020, [Accessed on 11-Nov-2020]. [Online]. Available: https://www.nationalgrideso.com/news/carbon-free-system-stability-pathfinder-stakeholder-feedback-request.

[96] T. Prevost and G. Denis, *WP3 - Control and Operation of a Grid with 100 % Converter-BasedDevices*. MIGRATE, Dec. 2019, [Accessed on 02-Oct-2020]. [Online]. Available: https://www.h2020-migrate.eu/_Resources/Persistent/1bb0f89024e41a85bf94f1ec7ee6f8d7c34bc29a/D3.6%20-%20Requirement%20guidelines%20for%20operating%20a%20grid%20with%20100%20power%20electronic%20devices.pdf.

[97] R. A. Allah, "Correlation-based synchro-check relay for power systems," *IET Generation, Transmission Distribution*, vol. 12, no. 5, pp. 1109–1120, 2018.

[98] M. J. Thompson, A. Li, R. Luo, M. C. Tu, and I. Urdaneta, "Advanced synchronizing systems for offshore power systems: Improving system reliability and flexibility," *IEEE Industry Applications Magazine*, vol. 23, no. 5, pp. 60–69, 2017. DOI: 10.1109/MIAS.2016.2600742.

[99] L. Fan, "Modeling Type-4 Wind in Weak Grids," *IEEE Transactions on Sustainable Energy*, vol. 10, no. 2, pp. 853–864, 2019. DOI: 10.1109/TSTE.2018.2849849.

[100] National Grid, *System Operability Framework: Whole system Short Circuit Level*. National Grid Warwick Technology Park, Gallows Hill, Warwick, UK., 2020, [Accessed on 11-Nov-2020]. [Online]. Available: https://www.nationalgrideso.com/research-publications/system-operability-framework-sof.

[101] H. Wen and M. Fazeli, "A low-voltage ride-through strategy using mixed potential function for three-phase grid-connected PV systems," *Electric Power Systems Research*, vol. 173, pp. 271–280, 2019, ISSN: 0378-7796. DOI: https://doi.org/10.1016/j.epsr.2019.04.039.

[102] National Grid, *Black Start from Distributed Energy Resources*. National Grid Warwick Technology Park, Gallows Hill, Warwick, UK., Nov. 2018, [Accessed on 14-Nov-2020]. [Online]. Available: https://www.ofgem.gov.uk/ofgem-publications/143706.

[103] National Grid, *Black Start from Non-Traditional Generation Technologies*. National Grid Warwick Technology Park, Gallows Hill, Warwick, UK., Jun. 2019, [Accessed on 14-Nov-2020]. [Online]. Available: https://www.nationalgrideso.com/document/148201/download.

[104] A. Pena Asensio, S. Arnaltes, J. L. Rodriguez-Amenedo, and M. A. Cardiel-Alvarez, "Decentralized frequency control for black start of full-converter wind turbines," *IEEE Transactions on Energy Conversion*, pp. 1–1, 2020. DOI: 10.1109/TEC.2020.3011611.

[105] F. R. Schleif and J. H. White, "Damping for the northwest - southwest tieline oscillations - an analog study," *IEEE Transactions on Power Apparatus and Systems*, vol. PAS-85, no. 12, pp. 1239–1247, 1966.

[106] H. Wang and W. Du, *Analysis and Damping Control of Power System Low-frequency Oscillations*, ser. Power Electronics and Power Systems. Springer US, 2016, ISBN: 9781489976963.

[107] M. Gibbard, P. Pourbeik, and D. Vowles, *Small-signal Stability, Control and Dynamic Performance of Power Systems*. University of Adelaide Press, 2015.

[108] G. J. W. Dudgeon, W. E. Leithead, A. Dysko, J. O'Reilly, and J. R. McDonald, "The Effective Role of AVR and PSS in Power Systems: Frequency Response Analysis," *IEEE Transactions on Power Systems*, vol. 22, no. 4, pp. 1986–1994, 2007.

[109] H. F. Wang, F. J. Swift, and M. Li, "Indices for selecting the best location of psss or facts-based stabilisers in multimachine power systems: A comparative study," *IEE Proceedings - Generation, Transmission and Distribution*, vol. 144, no. 2, pp. 155–159, 1997.

[110] P. Pourbeik and M. J. Gibbard, "Damping and synchronizing torques induced on generators by facts stabilizers in multimachine power systems," *IEEE Transactions on Power Systems*, vol. 11, no. 4, pp. 1920–1925, 1996.

[111] H. Cai, T. Littler, J. H. Huang, and Z. J. Xie, "Application of a damping torque analysis index for coordinated tuning of stabilisers in a large power grid," in *2014 IEEE PES General Meeting — Conference Exposition*, 2014, pp. 1–5.

[112] N. Jiang and H. Chiang, "Damping torques of multi-machine power systems during transient behaviors," *IEEE Transactions on Power Systems*, vol. 29, no. 3, pp. 1186–1193, 2014.

[113] K. Padiyar, *Facts Controllers in Power Transmission and Distribution*. Anshan, 2009, ISBN: 9781848290105.

[114] National Grid, *National Electricity Transmission System Security and Quality of Supply Standard*, 2.4. National Grid, Apr. 2019, [Accessed on 23-Sep-2020]. [Online]. Available: https://www.nationalgrideso.com/document/141056/download.

[115] D. Trudnowski, D. Kosterev, and J. Undrill, "PDCI damping control analysis for the western North American power system," in *2013 IEEE Power Energy Society General Meeting*, 2013, pp. 1–5.

[116] F. Wilches-Bernal, R. H. Byrne, and J. Lian, "Damping of Inter-Area Oscillations via Modulation of Aggregated Loads," *IEEE Transactions on Power Systems*, vol. 35, no. 3, pp. 2024–2036, 2020. DOI: 10.1109/TPWRS.2019.2948116.

[117] O. Samuelsson and B. Eliasson, "Damping of electro-mechanical oscillations in a multimachine system by direct load control," *IEEE Transactions on Power Systems*, vol. 12, no. 4, pp. 1604–1609, 1997.

[118] I. Kamwa, R. Grondin, D. Asber, J. P. Gingras, and G. Trudel, "Large-scale active-load modulation for angle stability improvement," *IEEE Transactions on Power Systems*, vol. 14, no. 2, pp. 582–590, 1999.

[119] R. Faranda, A. Pievatolo, and E. Tironi, "Load shedding: A new proposal," *IEEE Transactions on Power Systems*, vol. 22, no. 4, pp. 2086–2093, 2007.

[120] J. Lian, S. Wang, and M. E. J. Hansen, *Universal wide-area damping control for mitigating interarea oscillations in power systems*. Pacific Northwest National Laboratory, Richland, WA, USA, Tech. Rep. PNNL-27351, 2017.

[121] C. Zhang, D. Ke, Y. Sun, C. Y. Chung, and J. Xu, "Investigations of Large-Scale Voltage-Dependent Loads for Damping Inter-Area Oscillations: Mechanism and Robust Decentralized Control," *IEEE Transactions on Power Systems*, vol. 33, no. 6, pp. 6037–6048, 2018. DOI: 10.1109/TPWRS.2018.2854648.

[122] J. Lian, Q. Zhang, L. D. Marinovici, R. Fan, and J. Hansen, "Wide-Area Demand-Side Control for Inter-Area Oscillation Mitigation in Power Systems," in *2018 IEEE/PES Transmission and Distribution Conference and Exposition (T D)*, 2018, pp. 1–5.

[123] R. K. Varma, "Concepts of FACTS controllers," in *2011 IEEE/PES Power Systems Conference and Exposition*, 2011, pp. 1–6.

[124] T. U. Okeke and R. G. Zaher, "Flexible AC Transmission Systems (FACTS)," in *2013 International Conference on New Concepts in Smart Cities: Fostering Public and Private Alliances (SmartMILE)*, 2013, pp. 1–4.

[125] E. V. Larsen, J. J. Sanchez-Gasca, and J. H. Chow, "Concepts for design of facts controllers to damp power swings," *IEEE Transactions on Power Systems*, vol. 10, no. 2, pp. 948–956, 1995.

[126] R. K. Pandey and D. K. Gupta, "Integrated multi-stage LQR power oscillation damping FACTS controller," *CSEE Journal of Power and Energy Systems*, vol. 4, no. 1, pp. 83–91, 2018.

[127] D. Mondal, A. Chakrabarti, and A. Sengupta, *Power System Small Signal Stability Analysis and Control*. Elsevier Science, 2014, ISBN: 9780128005729.

[128] A. Siddique, Y. Xu, W. Aslam, and M. Rasheed, "A Comprehensive Study on FACTS Devices to Improve the Stability and Power Flow Capability in Power System," in *2019 IEEE Asia Power and Energy Engineering Conference (APEEC)*, 2019, pp. 199–205.

[129] N. Yang, Q. Liu, and J. D. McCalley, "TCSC controller design for damping interarea oscillations," *IEEE Transactions on Power Systems*, vol. 13, no. 4, pp. 1304–1310, Nov. 1998.

[130] J. Zuo, Y. Li, D. Shi, and X. Duan, "Simultaneous Robust Coordinated Damping Control of Power System Stabilizers (PSSs), Static Var Compensator (SVC) and Doubly-Fed Induction Generator Power Oscillation Dampers (DFIG PODs) in Multimachine Power Systems," *Energies*, vol. 10, no. 4, 2017.

[131] "IEEE Recommended Practice for Excitation System Models for Power System Stability Studies," *IEEE Std 421.5-2016 (Revision of IEEE Std 421.5-2005)*, pp. 1–207, 2016.

[132] T. Surinkaew and I. Ngamroo, "Hierarchical Coordinated Wide Area and Local Controls of DFIG Wind Turbine and PSS for Robust Power Oscillation Damping," *IEEE Transactions on Sustainable Energy*, vol. 7, no. 3, pp. 943–955, 2016.

[133] M. Edrah, K. L. Lo, and O. Anaya-Lara, "Impacts of high penetration of DFIG wind turbines on rotor angle stability of power systems," *IEEE Transactions on Sustainable Energy*, vol. 6, no. 3, pp. 759–766, Jul. 2015.

[134] T. Surinkaew and I. Ngamroo, "Coordinated Robust Control of DFIG Wind Turbine and PSS for Stabilization of Power Oscillations Considering System Uncertainties," *IEEE Transactions on Sustainable Energy*, vol. 5, no. 3, pp. 823–833, 2014.

[135] Y. Chi, B. Tang, J. Hu, X. Tian, H. Tang, Y. Li, S. Sun, L. Shi, and L. Shuai, "Overview of mechanism and mitigation measures on multi-frequency oscillation caused by large-scale integration of wind power," *CSEE Journal of Power and Energy Systems*, vol. 5, no. 4, pp. 433–443, 2019.

[136] W. Du, Q. Fu, and H. F. Wang, "Power system small-signal angular stability affected by virtual synchronous generators," *IEEE Transactions on Power Systems*, vol. 34, no. 4, pp. 3209–3219, 2019.

[137] D. Gautam, V. Vittal, and T. Harbour, "Impact of Increased Penetration of DFIG-Based Wind Turbine Generators on Transient and Small Signal Stability of Power Systems," *IEEE Transactions on Power Systems*, vol. 24, no. 3, pp. 1426–1434, 2009.

[138] Y. Li, L. Fan, and Z. Miao, "Wind in Weak Grids: Low-Frequency Oscillations, Subsynchronous Oscillations, and Torsional Interactions," *IEEE Transactions on Power Systems*, vol. 35, no. 1, pp. 109–118, 2020.

[139] L. Fan and Z. Miao, "An explanation of oscillations due to wind power plants weak grid interconnection," *IEEE Transactions on Sustainable Energy*, vol. 9, no. 1, pp. 488–490, Jan. 2018.

[140] J. Quintero, V. Vittal, G. T. Heydt, and H. Zhang, "The impact of increased penetration of converter control-based generators on power system modes of oscillation," *IEEE Transactions on Power Systems*, vol. 29, no. 5, pp. 2248–2256, 2014.

[141] S. Li, "Low-frequency oscillations of wind power systems caused by doubly-fed induction generators," *Renewable Energy*, vol. 104, pp. 129–138, 2017, ISSN: 0960-1481.

[142] T. Sadamoto, A. Chakrabortty, T. Ishizaki, and J. Imura, "Retrofit control of wind-integrated power systems," *IEEE Transactions on Power Systems*, vol. 33, no. 3, pp. 2804–2815, May 2018.

[143] J. Ma, Y. Qiu, Y. Li, W. Zhang, Z. Song, and J. S. Thorp, "Research on the Impact of DFIG Virtual Inertia Control on Power System Small-Signal Stability Considering the Phase-Locked Loop," *IEEE Transactions on Power Systems*, vol. 32, no. 3, pp. 2094–2105, May 2017.

[144] Y. Wang and Y. Yuan, "Inertia provision and small signal stability analysis of a wind-power generation system using phase-locked synchronized equation," *Sustainability*, vol. 11, no. 5, 2019.

[145] Z. Liu, C. Liu, G. Li, Y. Liu, and Y. Liu, "Impact Study of PMSG-Based Wind Power Penetration on Power System Transient Stability Using EEAC Theory," *Energies*, vol. 8, no. 12, pp. 13 419–13 441, 2015.

[146] M. J. Morshed and A. Fekih, "A Probabilistic Robust Coordinated Approach to Stabilize Power Oscillations in DFIG-Based Power Systems," *IEEE Transactions on Industrial Informatics*, vol. 15, no. 10, pp. 5599–5612, 2019.

[147] M. Singh, A. J. Allen, E. Muljadi, V. Gevorgian, Y. Zhang, and S. Santoso, "Interarea oscillation damping controls for wind power plants," *IEEE Transactions on Sustainable Energy*, vol. 6, no. 3, pp. 967–975, 2015.

[148] E. Vittal, M. O'Malley, and A. Keane, "Rotor angle stability with high penetrations of wind generation," *IEEE Transactions on Power Systems*, vol. 27, no. 1, pp. 353–362, 2012.

[149] L. Huang, H. Xin, and Z. Wang, "Damping low-frequency oscillations through VSC-HVDC stations operated as virtual synchronous machines," *IEEE Transactions on Power Electronics*, vol. 34, no. 6, pp. 5803–5818, Jun. 2019.

[150] C. Sun, G. Joos, and F. Bouffard, "Identification of low-frequency oscillation mode and improved damping design for virtual synchronous machines in microgrid," *IET Generation, Transmission Distribution*, vol. 13, no. 14, pp. 2993–3001, 2019.

[151] K. Shi, C. Chen, Y. Sun, P. Xu, Y. Yang, and F. Blaabjerg, "Rotor inertia adaptive control and inertia matching strategy based on parallel virtual synchronous generators system," *IET Generation, Transmission Distribution*, vol. 14, no. 10, pp. 1854–1861, 2020.

[152] T. Shintai, Y. Miura, and T. Ise, "Oscillation damping of a distributed generator using a virtual synchronous generator," *IEEE Transactions on Power Delivery*, vol. 29, no. 2, pp. 668–676, Apr. 2014. DOI: 10.1109/TPWRD.2013.2281359.

[153] J. R. Pérez, J. A. Suul, S. D'Arco, A. Rodríguez-Cabero, and M. Prodanovic, "Virtual synchronous machine control of VSC-HVDC for power system oscillation damping," in *IECON 2018 - 44th Annual Conference of the IEEE Industrial Electronics Society*, Oct. 2018, pp. 6026–6031. DOI: 10.1109/IECON.2018.8591097.

[154] W. Sheng, Y. Wang, B. Liu, S. Duan, and M. Wu, "Virtual synchronous generator strategy for suppressing output power fluctuation without additional energy storage," *IET Power Electronics*, vol. 13, no. 3, pp. 602–610, 2020.

[155] G. W. Moshe Blau, "Synchronverters used for damping inter-area oscillations in two-area power systems," in *International Conference on Renewable Energies and Power Quality (ICREPQ)*, Mar. 2018.

[156] Q. Zhong and Y. Zeng, "Universal droop control of inverters with different types of output impedance," *IEEE Access*, vol. 4, pp. 702–712, Mar. 2016. DOI: 10.1109/ACCESS.2016.2526616.

[157] N. Pogaku, M. Prodanovic, and T. C. Green, "Modeling, analysis and testing of autonomous operation of an inverter-based microgrid," *IEEE Transactions on Power Electronics*, vol. 22, no. 2, pp. 613–625, Mar. 2007. DOI: 10.1109/TPEL.2006.890003.

[158] Y. Levron, J. Belikov, and D. Baimel, "A tutorial on dynamics and control of power systems with distributed and renewable energy sources based on the DQ0 transformation," *Applied Sciences*, vol. 8, no. 9, Sep. 2018.

[159] A. Ellis, E. Muljadi, J. Sanchez-Gasca, and Y. Kazachkov, "Generic models for simulation of wind power plants in bulk system planning studies," in *2011 IEEE Power and Energy Society General Meeting*, 2011, pp. 1–8.

[160] B. Muftau, M. Fazeli, and A. Egwebe, "Stability analysis of a PMSG based Virtual Synchronous Machine," *Electric Power Systems Research*, vol. 180, p. 106 170, Mar. 2020.

[161] M. Mueller, *Electrical Drives for Direct Drive Renewable Energy Systems*, ser. Woodhead Publishing Series in Energy. Woodhead Publishing, 2013, ISBN: 978-1-84569-783-9. DOI: https://doi.org/10.1016/B978-1-84569-783-9.50014-6.

[162] O. P. Mahela, N. Gupta, M. Khosravy, and N. Patel, "Comprehensive overview of low voltage ride through methods of grid integrated wind generator," *IEEE Access*, vol. 7, pp. 99 299–99 326, 2019. DOI: 10.1109/ACCESS.2019.2930413.

[163] M. Nasiri, J. Milimonfared, and S. Fathi, "A review of low-voltage ride-through enhancement methods for permanent magnet synchronous generator based wind turbines," *Renewable and Sustainable Energy Reviews*, vol. 47, pp. 399–415, 2015, ISSN: 1364-0321. DOI: https://doi.org/10.1016/j.rser.2015.03.079.

[164] J. I. Yoo, J. Kim, and J. Park, "Converter control of pmsg wind turbine system for inertia-free stand-alone microgrid," in *2016 IEEE Industry Applications Society Annual Meeting*, Oct. 2016, pp. 1–8.

[165] X. Guo, S. Liu, and X. Wang, "Impact of phase-locked loop on stability of active damped lcl-filter-based grid-connected inverters with capacitor voltage

feedback," *Journal of Modern Power Systems and Clean Energy*, vol. 5, no. 4, pp. 574–583, Jul. 2017.

[166] J. Beerten, S. D'Arco, and J. A. Suul, "Identification and small-signal analysis of interaction modes in vsc mtdc systems," *IEEE Transactions on Power Delivery*, vol. 31, no. 2, pp. 888–897, 2016. DOI: 10.1109/TPWRD.2015.2467965.

[167] G. Li, Z. Du, T. An, Y. Xia, and J. Lei, "Impact of pll and vsc control parameters on the ac/mtdc systems stability," *Electric Power Systems Research*, vol. 141, pp. 476–486, 2016.

[168] C. Zhang, X. Wang, and F. Blaabjerg, "Analysis of phase-locked loop influence on the stability of single-phase grid-connected inverter," in *2015 IEEE 6th International Symposium on Power Electronics for Distributed Generation Systems (PEDG)*, Jun. 2015, pp. 1–8.

[169] Y. A. I. Mohamed and E. F. El-Saadany, "Adaptive decentralized droop controller to preserve power sharing stability of paralleled inverters in distributed generation microgrids," *IEEE Transactions on Power Electronics*, vol. 23, no. 6, pp. 2806–2816, Nov. 2008.

[170] A. E. M. Bouzid, P. Sicard, A. Yamane, and J. Paquin, "Simulation of droop control strategy for parallel inverters in autonomous ac microgrids," in *2016 8th International Conference on Modelling, Identification and Control (ICMIC)*, Nov. 2016, pp. 701–706.

[171] O. Kotb, M. Ghandhari, R. Eriksson, and V. K. Sood, "On small signal stability of an ac/dc power system with a hybrid mtdc network," *Electric Power Systems Research*, vol. 136, pp. 79–88, 2016.

[172] S.-K. Chung, "A phase tracking system for three phase utility interface inverters," *IEEE Transactions on Power Electronics*, vol. 15, no. 3, pp. 431–438, May 2000, ISSN: 0885-8993. DOI: 10.1109/63.844502.

[173] Y. Tan, L. Meegahapola, and K. M. Muttaqi, "A suboptimal power-point-tracking-based primary frequency response strategy for dfigs in hybrid remote area power supply systems," *IEEE Transactions on Energy Conversion*, vol. 31, no. 1, pp. 93–105, Mar. 2016, ISSN: 0885-8969. DOI: 10.1109/TEC.2015.2476827.

[174] "IEEE Standard for Interconnecting Distributed Resources with Electric Power Systems," *IEEE Std 1547-2003*, pp. 1–28, 2003. DOI: 10.1109/IEEESTD.2003.94285.

[175] M. O. Baruwa and M. Fazeli, "Impact of virtual synchronous machines on low-frequency oscillations in power systems," *IEEE Transactions on Power Systems*, 2020. DOI: 10.1109/TPWRS.2020.3029111.

[176] E. Vittal, M. O'Malley, and A. Keane, "Rotor angle stability with high penetrations of wind generation," *IEEE Transactions on Power Systems*, vol. 27, no. 1, pp. 353–362, Feb. 2012.

[177] J. Belikov and Y. Levron, "Uses and misuses of quasi-static time-varying phasor models in power systems," *IEEE Transactions on Power Delivery*, vol. 33, no. 6, pp. 3263–3266, Dec. 2018. DOI: 10.1109/TPWRD.2018.2852950.

[178] D. Baimel, J. Belikov, J. M. Guerrero, and Y. Levron, "Dynamic modeling of networks, microgrids, and renewable sources in the dq0 reference frame: A survey," *IEEE Access*, vol. 5, pp. 21 323–21 335, Oct. 2017.

[179] M. Rasheduzzaman, J. A. Mueller, and J. W. Kimball, "An accurate small-signal model of inverter- dominated islanded microgrids using *dq* reference frame," *IEEE Journal of Emerging and Selected Topics in Power Electronics*, vol. 2, no. 4, pp. 1070–1080, 2014. DOI: 10.1109/JESTPE.2014.2338131.

[180] J. Machowski, Z. Lubosny, J. Bialek, and J. Bumby, *Power System Dynamics: Stability and Control*. Wiley, 2020.

[181] H. Ergun, J. Dave, D. Van Hertem, and F. Geth, "Optimal power flow for ac–dc grids: Formulation, convex relaxation, linear approximation, and implementation," *IEEE Transactions on Power Systems*, vol. 34, no. 4, pp. 2980–2990, 2019.

[182] C. Canizares *et al.*, "Benchmark models for the analysis and control of small-signal oscillatory dynamics in power systems," *IEEE Transactions on Power Systems*, vol. 32, no. 1, pp. 715–722, Jan. 2017.

APPENDIX

A. SYSTEM FORMULATION

A.1 *abc* - *dq0* Transformation

$$\begin{bmatrix} i_a \\ i_b \\ i_c \end{bmatrix} = \begin{bmatrix} cos\theta & -sin\theta & 1 \\ cos(\theta - \frac{2\pi}{3}) & -sin(\theta - \frac{2\pi}{3}) & 1 \\ cos(\theta + \frac{2\pi}{3}) & -sin(\theta + \frac{2\pi}{3}) & 1 \end{bmatrix} \begin{bmatrix} i_d \\ i_q \\ i_0 \end{bmatrix} \tag{A.1}$$

A.2 *dq0* - *abc* Transformation

$$\begin{bmatrix} i_d \\ i_q \\ i_0 \end{bmatrix} = \frac{2}{3} \begin{bmatrix} cos\theta & cos(\theta - \frac{2\pi}{3}) & cos(\theta + \frac{2\pi}{3}) \\ -sin\theta & -sin(\theta - \frac{2\pi}{3}) & -sin(\theta + \frac{2\pi}{3}) \\ \frac{1}{2} & \frac{1}{2} & \frac{1}{2} \end{bmatrix} \begin{bmatrix} i_a \\ i_b \\ i_c \end{bmatrix} \tag{A.2}$$

A.3 Formulation of Power in *dq* frame

$$P = \frac{3}{2}(V_d i_d + V_q i_q) \tag{A.3}$$

$$Q = \frac{3}{2}(-V_d i_q + V_q i_d) \tag{A.4}$$

Tab. A.1. System Base Values

Quantity	Symbol and Expression	Description
Rated Power	$S_b = \sqrt{P^2 + Q^2}$	VA rating of machine
Base Voltage	$V_{L-L} = V_b$	Amplitude of line to line nominal voltage
Base Current	$i_b = \dfrac{S_b}{\sqrt{3}V_b}$	Amplitude of nominal line current
Base Impedance	$Z_b = \dfrac{V_b^2}{S_b}$	
Base Inductance	$L_b = \dfrac{Z_b}{\omega_b}$	
Base Capacitance	$C_b = \dfrac{1}{Z_b\omega_b}$	
Frequency	$\omega = \omega_b$	Nominal frequency

A.4 Wind Turbine Modelling

The MATLAB/SIMULINK wind turbine model was employed in the thesis. The mechanical power P_m captured by the wind turbine can be expressed by the following equation (A.5):

$$P_m = 0.5\rho A\upsilon^3 C_p(\lambda, \beta) \tag{A.5}$$

The air density in Kg/m^3 is represented by ρ, A is the area swept by the turbine blades in m^2, υ is the wind speed in m/s, T_m is mechanical torque in Nm, ω_r is the rotor speed in rad/s and C_p (λ, β) is the power coefficient. The C_p (λ, β) is a non-linear function of the tip speed ratio λ and the pitch angle β, which is given by (A.6), (A.7):

$$C_p(\lambda, \beta) = 0.5176\left(\frac{116}{\lambda_i} - 0.4\beta - 5\right)e^{-21/\lambda_i} + 0.0068\lambda_i\Big) \tag{A.6}$$

$$\frac{1}{\lambda_i} = \frac{1}{\lambda_{opt} + 0.08\beta} - \frac{0.035}{\beta^3 + 1} \tag{A.7}$$

The notation λ_i represents the instantaneous value of the tip speed ratio which varies with β, while λ_{opt} represents the optimal tip speed ratio.